



Raytheon

USER'S GUIDE FOR VIIRS CLOUD IMAGERY PRODUCTS

Version 5: March 2002

Keith Hutchison
Kenneth A. Jensen
Shawn Miller

SRBS Document #: Y2466 (Appendix)

EDR: IMAGERY USER'S GUIDE

Doc No: Y2466 (Appendix)

Version: 5

Revision: 0

	Function	Name	Signature	Date
PREPARED BY	EDR DEVELOPER	K. HUTCHISON		
APPROVED BY	IMAGERY IPT LEAD	K. JENSEN		
REVIEWED BY	REVIEWER	K. JENSEN		
APPROVED BY	CHIEF SCIENTIST	S. MILLER		
RELEASED BY	ALGORITHM IPT LEAD	P. KEALY		

Table of Contents

Table of Contents	i
List of Tables	iii
List of Figures	iv
Preface	viii
Chapter 1	1
INTRODUCTION	1
1.1 PURPOSE	1
1.2 SCOPE.....	2
Chapter 2	3
NPOESS SYSTEM OVERVIEW	3
2.1 SATELLITES AND SENSORS	3
2.2 PRIMARY VIIRS EDR REQUIREMENTS	5
2.3 VIIRS IMAGERY EDR REQUIREMENTS	7
2.4 VIIRS APPLICATION-RELATED IMAGERY REQUIREMENTS	9
2.4.1 <i>Cloud Cover</i>	10
2.4.2 <i>Cloud Type</i>	11
2.5 VALUE OF MANUALLY-GENERATED CLOUD ANALYSES.....	12
2.5.1 <i>Performance Verification of Automated Cloud Models</i>	12
2.5.2 <i>Quality Control of Automated Cloud Analyses</i>	13
Chapter 3	17
THEORETICAL BASIS FOR MANUAL CLOUD ANALYSES	17
3.1 PHYSICS OF THE PROBLEM.....	17
3.2 DEFINITION OF CLOUD TRUTH DATA SETS	20
3.2.1 <i>Cloud Truth from Manual Interpretation of Multispectral Imagery</i>	21
3.2.2 <i>Cloud Truth in Synthetic Scenes for Sensor Simulations</i>	24
3.3 SENSOR BANDPASS SELECTION PROCESS.....	27
3.3.1 <i>Basic Concepts of Satellite Radiometry and Instrument Design</i>	27
3.3.2 <i>Phenomenology of Spectral Signatures</i>	29
3.3.3 <i>VIIRS Imagery Bandpass Selection for Manual Cloud Detection</i>	32
Chapter 4	39
VIIRS INSTRUMENT CHARACTERISTICS	39
Chapter 5	43

PRINCIPALS IN IMAGE INTERPRETATION	43
5.1. INTRODUCTION.....	43
5.2. VIIRS IMAGERY DATA	46
5.2.1. VIIRS Imagery Band I1 ($0.640 \pm 0.040 \mu\text{m}$).....	47
5.2.2. VIIRS I2 Band ($0.865 \pm 0.020 \mu\text{m}$).....	50
5.2.3. VIIRS I3 and M10 Bands ($1.61 \pm 0.03 \mu\text{m}$).....	54
5.2.4. VIIRS I4 Band $3.74 (\pm 0.19 \mu\text{m})$ and M12 Band ($3.7 \pm 0.09 \mu\text{m}$)	56
5.2.5. VIIRS I5 Band ($11.45 \pm 0.95 \mu\text{m}$).....	73
5.2.6. VIIRS Day Night Band (DNB).....	79
5.3. VIIRS IMAGERY ASSIST DATA	82
5.3.1. VIIRS M1–M4 Bands ($0.412 \pm 0.010 \mu\text{m}$, $0.445 \pm 0.009 \mu\text{m}$, $0.488 \pm 0.010 \mu\text{m}$, $0.555 \pm 0.010 \mu\text{m}$)..	83
5.3.2. VIIRS M9 Band ($1.378 \pm 0.0075 \mu\text{m}$).....	87
Chapter 6.....	91
MULTICOLOR COMPOSITES OF MULTISPECTRAL IMAGERY.....	91
6.1. INTRODUCTION.....	91
6.2. COLOR COMPOSITES OF (0.64 μm , 0.865 μm , AND 12.0 μm) SURFACE VEGETATION AND CLOUD CLASSIFICATION FROM VIIRS IMAGERY BANDS	93
6.3. COLOR COMPOSITES OF (3.7 μm ALBEDO, 0.865 μm , 12.0 μm) POSITIVE SNOW DETECTION WITH VIIRS IMAGERY BANDS.....	95
6.4. COLOR COMPOSITES OF (0.64 μm , 0.64 μm , 3.7 μm ALBEDO) SNOW MAPPING THROUGH THIN CIRRUS CLOUDS WITH VIIRS IMAGERY BANDS.....	97
6.5. COLOR COMPOSITES OF (0.412 μm , 0.865 μm , AND 0.64 μm) CLOUDS OVER ARID REGIONS USING VIIRS IMAGERY AND IMAGERY ASSIST BANDS	99
6.6. COLOR COMPOSITES SERIES FROM MODIS AIRBORNE SIMULATOR DATA.....	101
Chapter 7.....	119
REFERENCES	119

List of Tables

TABLE 1. RECENT SATELLITES AND SENSOR SUPPORTING THE WMO’S WWW PROGRAM.....	4
TABLE 2. PLANNED LAUNCHES OF NPOESS SATELLITES AND SENSOR CONFIGURATIONS.....	5
TABLE 3. ATTRIBUTE REQUIREMENTS FOR EACH VIIRS BAND CLASSIFIED AS IMAGERY	8
TABLE 4. NPOESS REQUIREMENTS FOR MANUALLY-GENERATED CLOUD COVER EDR.....	11
TABLE 5. NPOESS REQUIREMENTS FOR MANUALLY-GENERATED CLOUD TYPE EDR.....	11
TABLE 6. COMPARISONS OF MANUALLY-GENERATED CLOUD MASK AND SIMULATION BINARY CLOUD MASK FOR SYNTHETIC VIIRS IMAGERY SHOWN IN FIGURE 8.	26
TABLE 7. VIIRS IMAGERY BANDS NEEDED TO SATISFY EACH NPOESS VIIRS REQUIREMENT FOR MANUALLY- GENERATED CLOUD COVER AND CLOUD TYPE EDRs (NPOESS VIIRS SRD, 2000).....	33
TABLE 8. VIIRS IMAGERY AND IMAGERY ASSIST BAND SELECTED TO SATISFY NPOESS REQUIREMENTS.....	34
TABLE 9. BANDPASSES OF SENSORS THAT CLOSELY APPROXIMATE VIIRS IMAGERY RESOLUTION BANDS.....	46
TABLE 10. BANDPASSES OF SENSORS THAT CLOSELY APPROXIMATE VIIRS MODERATE RESOLUTION BANDS.....	82

List of Figures

FIGURE 1. METEOROLOGICAL SATELLITES SUPPORTING THE WMO WORLD WEATHER WATCH PROGRAM.	14
FIGURE 2. HRCF CLOUD FORECAST RELIABILITY ESTABLISHED DURING 1990 CMEP STUDY (HUTCHISON AND JANOTA, 1989).	23
FIGURE 3. CLOUDS AND SNOW ARE BRIGHT IN AVHRR IMAGERY CHANNEL 2 (0.9 μm) AT PANEL (A) AND CHANNEL 5 (12.0 μm) AT PANEL (B) OF A NOAA-12 SCENE COLLECTED ON MARCH 19, 1996 (HUTCHISON ET AL, 1997)...	31
FIGURE 4. CLOUDS SEEN IN THE 0.6 μm BAND (CHANNEL 1) OF THE AVHRR IMAGERY IN PANEL (A) ARE CONTAINED THE MANUALLY-GENERATED CLOUD ANALYSIS, ARE SHOWN AS RED, IN PANEL (B).....	32
FIGURE 5. SNOW NOW APPEARS BLACK IN PANEL (A) CONTAINING THE ALBEDO COMPONENT OF THE 3.7 μm BAND (CHANNEL 3) OF THE AVHRR IMAGERY WHILE PANEL (B) CONTAINS THE MANUALLY-GENERATED CLOUD ANALYSIS MADE USING THIS IMAGE.	33
FIGURE 6. EXAMPLE OF A TOTAL CNC ANALYSIS CREATED BY MERGING CNC ANALYSES FROM INDIVIDUAL SPECTRAL BANDS SHOWN IN FIGURES 4 AND 5 INTO A SINGLE CNC ANALYSIS.	33
FIGURE 7. SYNTHETIC BACKGROUND SHOWN IN PANEL (A) ARE USED WITH CLOUD MASK, SHOWN IN PANEL (B) TO GENERATE SYNTHETIC VIIRS IMAGERY.	34
FIGURE 8. SYNTHETIC 12.0 μm VIIRS IMAGE, MANUAL AND SYNTHETIC CLOUD MASKS, AND DIFFERENCE FIELDS SHOW LOCATIONS OF INACCURACIES IN MANUALLY-GENERATED CLOUD DATA PRODUCT.....	35
FIGURE 9. SOLAR SPECTRAL IRRADIANCE DISTRIBUTION FOR TOP OF THE ATMOSPHERE (TOA) AND SEA LEVEL ALONG WITH PRIMARY ATMOSPHERIC ABSORPTION BANDS AND SPECIES. (FIGURE 2.6 FROM LIOU, 1980).	39
FIGURE 10. SPECTRAL SIGNATURES OF CLOUD PARTICLES AND SURFACE BACKGROUNDS IN 0.3 - 1.0 MICRON RANGE. (KEY: REFLECTIVITIES: VEGETATED LAND = GREEN, OCEAN = DARK BLUE, SNOW = WHITE, SAND = YELLOW., SOLAR ILLUMINATION = GOLD AND ATMOSPHERIC TRANSMISSION = BLACK. VIIRS BANDS BLUE.)	45
FIGURE 11. SPECTRAL SIGNATURES OF CLOUD PARTICLES AND SURFACE BACKGROUNDS IN 1.0 - 3.0 MICRON RANGE. (KEY: REFLECTIVITIES OF, VEGETATED LAND = GREEN, OCEAN = DARK BLUE, SNOW = WHITE, SAND = YELLOW. SOLAR ILLUMINATION = GOLD AND ATMOSPHERIC TRANSMISSION = BLACK. VIIRS BANDS ARE SHOWN IN LIGHTER BLUE.).....	46
FIGURE 12. SPECTRAL SIGNATURES OF CLOUD PARTICLES AND SURFACE BACKGROUNDS IN 3.0 - 5.0 MICRON RANGE. (KEY: REFLECTIVITIES OF, VEGETATED LAND = GREEN, OCEAN = DARK BLUE, SNOW = WHITE, SAND = YELLOW. SOLAR ILLUMINATION = GOLD AND ATMOSPHERIC TRANSMISSION = BLACK. VIIRS BANDS ARE SHOWN IN LIGHTER BLUE.).....	47
FIGURE 13. SPECTRAL SIGNATURES OF CLOUD PARTICLES AND SURFACE BACKGROUNDS IN 5.0.- 15.0 MICRON RANGE. (KEY: REFLECTIVITIES OF, VEGETATED LAND = GREEN, OCEAN = DARK BLUE, SNOW = WHITE, SAND = YELLOW. SOLAR ILLUMINATION = GOLD AND ATMOSPHERIC TRANSMISSION = BLACK. VIIRS BANDS ARE SHOWN IN LIGHTER BLUE.).....	48
FIGURE 14. SUMMARY OF VIIRS DESIGN CONCEPTS AND HERITAGE.....	40
FIGURE 15. VIIRS DETECTOR FOOTPRINT AGGREGATION SCHEME FOR BUILDING IMAGERY PIXELS	41
FIGURE 16. HORIZONTAL SAMPLING INTERVAL (hSI) FOR IMAGERY BANDS (AGGREGATION IN SCAN DIRECTION).....	41
FIGURE 17. VIIRS AGGREGATION AND BOW TIE PIXEL REDUCTION	62
FIGURE 18. NORMALIZED DISTRIBUTION OF EMISSION SPECTRA FOR THREE BLACKBODIES WITH ABSOLUTE TEMPERATURES OF 6000 K (SUN), 770 K (FOREST FIRES), AND 300 K (EARTH'S SURFACE) SHOWS PRIMARY ENERGY SOURCES FOR EACH OF THE VIIRS SPECTRAL BANDS (FIGURE 2.7.1, SCORER, 1990).	54

FIGURE 19. SPECTRAL SIGNATURES IN VIIRS I1 BAND SHOWS SNOW WITH A VERY HIGH REFLECTIVITY WHILE VEGETATED LAND AND OCEAN ARE VERY LOW. SIGNATURES OF WATER CLOUDS AND BARE SOIL ARE SIMILAR.	58
FIGURE 20. SIGNATURES OF CLOUDS AND LAND SURFACES TYPICAL OF THOSE PRESENT IN THE VIIRS I1 BAND ARE SEEN IN THE NOAA-12 AVHRR CHANNEL 1 IMAGERY COLLECTED NEAR SAN FRANCISCO, CA ON FEBRUARY 19, 1996 (HUTCHISON ET AL., 1997).	59
FIGURE 21. SPECTRAL SIGNATURES IN VIIRS I2 BAND SHOWS SNOW, WATER CLOUDS AND VEGETATED LAND WITH HIGH VALUES OF REFLECTIVITY WHILE WATER SURFACES REMAIN VERY LOW. THE REFLECTIVITY OF VEGETATED SOIL IS NOW HIGHER THAN THAT OF BARE SOIL	51
FIGURE 22. SIGNATURES OF CLOUDS AND LAND SURFACES TYPICAL OF THOSE PRESENT IN THE VIIRS I2 BAND ARE SEEN IN THE NOAA-12 AVHRR CHANNEL 1 IMAGERY COLLECTED NEAR SAN FRANCISCO, CA ON FEBRUARY 19, 1996 (HUTCHISON ET AL., 1997).	62
FIGURE 23. SIGNATURES OF CLOUDS AND LAND SURFACES TYPICAL OF THOSE PRESENT IN THE VIIRS I2 BAND ARE SEEN IN THE SEAWIFS DATA COLLECTED OVER SOUTHWESTERN US ON JULY 13, 2001 AS ALSO SHOWN IN FIGURE 40.	63
FIGURE 24. THEORETICAL CALCULATIONS OF ATMOSPHERIC AND SURFACE PROPERTIES IN THE 1.61 μm BAND THAT CONSTITUTES THE VIIRS I3 AND M10 CHANNELS.	54
FIGURE 25. THEMATIC MAPPER DATA COLLECTED OVER THE SIERRA NEVADA MOUNTAINS SHOW THE VALUE OF 1.61 μm IMAGERY FOR DIFFERENTIATING BETWEEN WATER CLOUDS (BRIGHT IN BOTH BANDS) AND SNOW (BLACK IN ONLY THE 1.61 μm IMAGE).	65
FIGURE 26. THEORETICAL CALCULATIONS OF ATMOSPHERIC AND SURFACE PROPERTIES IN THE 3.7 μm BAND THAT CONSTITUTES THE VIIRS I4 AND M12 CHANNELS.	67
FIGURE 27. ATMOSPHERIC ATTENUATION IN AVHRR 3.7, 10.8, AND 11.8 μm IR CHANNELS AS A FUNCTION OF TOTAL ATMOSPHERIC WATER VAPOR (HUTCHISON ET AL., 1995).	68
FIGURE 28. SUNGLINT IN AVHRR CHANNEL 2 AND CHANNEL 3 BANDS OF NOAA-15 MISSION OVER SOUTHEASTERN UNITED STATES.	71
FIGURE 29. STRATUS OVER SAN FRANCISCO BAY AND COASTAL CALIFORNIA IN NIGHTTIME 3.7 μm AND 11 μm IMAGERY COLLECTED BY NOAA-14.	73
FIGURE 30. CHANNELS 1,3, AND 5 OF NOAA-12 IMAGERY COLLECTED AT ABOUT 7:05 AM PST ON MARCH 19, 1996 OVER WESTERN UNITED STATES AND PACIFIC COASTAL REGIONS.	74
FIGURE 31. NOAA-12 SCENE COLLECTED AT ABOUT 7:05 AM LOCAL PST (1505 GMT) ON MARCH 19, 1996 OVER WESTERN UNITED STATES AND PACIFIC COASTAL REGIONS (HUTCHISON AND LOCKE, 1997).	76
FIGURE 32. NOAA-12 SCENE COLLECTED AT ABOUT 7:58 AM LOCAL (1558 GMT) ON MARCH 12, 1996 OVER WESTERN UNITED STATES AND PACIFIC COASTAL REGIONS (HUTCHISON ET AL., 1997)	77
FIGURE 33. AMBIGUITIES IN SPECTRAL SIGNATURES CAN IMPACT A-PRIORI CLOUD TOP PHASE ANALYSES OF THIS NOAA-12 AVHRR SCENE COLLECTED AT 1558 GMT ON MARCH 12, 1996. ZOOMING IN ON THE LOWER-RIGHT QUADRANT OF CHANNEL 5, C(1), AND CHANNEL 3A, C(2), SHOWS THE DIFFICULTY IN MANUALLY CLASSIFYING CIRRUS SINCE ICE APPEARANCE CHANGES AS OPTICAL THICKNESS DECREASES FROM (A) TO (B) (HUTCHISON ET AL., 1997).	78
FIGURE 34A. SIMULATED AVHRR (CH3-CH5) BRIGHTNESS TEMPERATURE DIFFERENCE VERSUS OPTICAL THICKNESS OF CIRRUS IN MID-LATITUDE WINTER ATMOSPHERE WITH CLOUD TEMPERATURE OF 236K AND RADII OF 20 AND 40 MICRONS (HUTCHISON ET AL., 1997).	79
FIGURE 34B. SIMULATED AVHRR (CHANNEL 3 MINUS CHANNEL 5) BRIGHTNESS TEMPERATURE DIFFERENCE VERSUS CHANNEL 4 TEMPERATURE FOR CIRRUS OF VARIABLE EMISSIVITY AT 10 KM IN SUB-ARCTIC WINTER ATMOSPHERE (HUTCHISON ET AL., 1997).	80
FIGURE 35. PLUMES FROM SEVERAL FOREST FIRES (INCLUDING THE ONE NEAR LOS ALAMOS, NEW MEXICO) ARE EVIDENT IN CHANNEL 2 OF THE NOAA-12 AVHRR SCENE COLLECTED AT 2319 GMT ON MAY 11, 2000.	81

FIGURE 36. HOT SPOTS IN THE FOREST FIRES ARE EVIDENT IN CHANNEL 3 OF THE NOAA-12 AVHRR SCENE COLLECTED AT 2319 GMT ON MAY 11, 2000. SEVERAL IN THE MOUNTAINS OF MEXICO SHOW NO PLUMES.	82
FIGURE 37. SPECTRAL SIGNATURES IN VIIRS I5 IMAGERY, M15 AND M16 MODERATE RESOLUTION BANDS.	83
FIGURE 38. GOES-EAST VISIBLE AND IR IMAGERY OF TEXAS ON APRIL 4, 2001 AT 1600 GMT SHOW EXTENSIVE WATER CLOUDS OVER THE EASTERN AND THIN CIRRUS CLOUDS OVER WESTERN TEXAS.	86
FIGURE 39. BRIGHTNESS TEMPERATURES IN AVHRR CHANNEL 4 IMAGERY OF VARIOUS CLOUDS LOCATED OVER TEXAS AT 1127 GMT ON APRIL 4, 2001.	87
FIGURE 40. RADIOSONDE FOR CORPUS CHRISTI, TEXAS AT 1200 UTC ON APRIL 4, 2001 ALONG WITH THERMODYNAMIC (SKEWT-LOGP) CHART OF THESE DATA SHOW CLOUD TOP TEMPERATURE OF 19.6C.	88
FIGURE 41. SPECTRAL RESPONSE OF THE DAYTIME/NIGHTTIME VISIBLE IMAGERY BAND, COMPARED WITH THE LUNAR SIGNAL.	79
FIGURE 42. SNR PERFORMANCE OF THE DAYTIME/NIGHTTIME VISIBLE IMAGERY UNDER QUARTER-MOON ILLUMINATION CONDITIONS, AS A FUNCTION OF SCAN ANGLE.	80
FIGURE 43. SPECTRAL F13 OLS VISIBLE (HRD) IMAGE FOR THE FIRST TERMINATOR CROSSING OF THE JULY 20, 2001 1131 UT ORBIT.	81
FIGURE 44. THEORETICAL CALCULATIONS OF ATMOSPHERIC AND SURFACE PROPERTIES IN THE VIIRS M1-M4 BANDS.	94
FIGURE 45. SEAWIFS DATA FROM THE 412 NM AND 488 BANDPASSES ARE SHOWN FOR THE WESTERN US AND NORTHERN MEXICO ON JULY 13, 2001 AT 1954 GMT.	95
FIGURE 45A. SEAWIFS DATA IN THE 555 NM AND 765 NM BANDS ARE SHOWN FOR THE SCENE OVER THE WESTERN US AND NORTHERN MEXICO ON JULY 13, 2001 AT 1954 GMT.	96
FIGURE 46. THEORETICAL CALCULATIONS OF ATMOSPHERIC AND SURFACE PROPERTIES IN THE 1.378 μm BAND THAT CONSTITUTES THE VIIRS M9 BAND.	98
FIGURE 47. THE TWO-WAY CLEAR-SKY TRANSMITTANCES FOR ENERGY ARRIVING AT SATELLITE ALTITUDE IN THE 1.38 μm REGION FOR A PERFECT REFLECTOR LOCATED AT DIFFERENT ALTITUDES. CALCULATIONS BASED UPON SUB-ARCTIC SUMMER ATMOSPHERE AND LOWTRAN. (GAO ET AL., 1993).	99
FIGURE 48. AVIRIS IMAGERY FOR VIIRS I2 AND M9 CHANNELS OVER COFFEVILLE, KS SHOWS VALUE OF MASKING SURFACE FEATURES FOR MANUAL INTERPRETATION OF THIN CIRRUS.	100
FIGURE 49. AVIRIS IMAGERY FOR VIIRS I2 AND M9 CHANNELS OVER TEXAS GULF COAST REVEALS THAT LOW-LEVEL WATER CLOUDS ARE MASKED IN 1.38 μm IMAGERY.	100
FIGURE 50. COLOR COMPOSITE TO EMPHASIZE VEGETATED LAND SURFACES CREATED BY ASSIGNING 0.64 μm BAND ASSIGNED TO RED AND GREEN GUNS OF CRT AND 0.865 μm ALBEDO CHANNEL ASSIGNED TO BLUE GUN.	102
FIGURE 51. PLACING THE 12.0 μm CHANNEL IN THE BLUE GUN OF FIGURE 50 PROVIDES VALUABLE DATA ON CLOUD TOP TEMPERATURES NEEDED FOR CLOUD TYPING. WARM, LOW LEVEL WATER CLOUDS APPEAR YELLOW WHILE COLDER ICE CLOUDS ARE BLUE.	103

FIGURE 52. REPLACING THE BAND IN THE RED GUN OF FIGURE 51 WITH THE 3.7 ALBEDO CHANNEL ALLOWS SNOW TO BE DIFFERENTIATED FROM LOWER-LEVEL WATER CLOUDS, THIN CIRRUS, AND THICKER CIRRUS WHILE MAINTAINING INFORMATION ON CLOUD TOP TEMPERATURES AND VEGETATED LAND SURFACES (RED = 3.7 μM ALBEDO, GREEN = 0.865 μM , BLUE = 12.0 μM).	105
FIGURE 53. COLOR COMPOSITE RED = 0.64 μM BAND, GREEN = 0.64 μM BAND, BLUE = 3.7 μM ALBEDO BAND) FOR THE MANUAL DETECTION AND MAPPING OF SNOW THROUGH CIRRUS CLOUDY CONDITIONS (HUTCHISON AND LOCKE, 1997).	107
FIGURE 54. COMPOSITE IMAGE (RED = 0.412 μM , GREEN = 0.865 μM , BLUE = 0.64 μM) FOR THE DETECTION CLOUDS OVER HIGHLY REFLECTIVE, ARID OR SEMI-ARID REGIONS.	109
FIGURE 55. RGB (0.64, 1.61, BT10.8/BT12.0)	111
FIGURE 56. RGB (1.38[1.88], 1.61, 12.0).....	112
FIGURE 57. RGB (1.61, INVERT BT8.6, 0.64)	113
FIGURE 58. RGB (BT11, BT8.6, BT3.75)	114
FIGURE 59. RGB (0.64, 1.38[1.88], 1.61).....	115
FIGURE 60. RGB (0.64, 1.61, 3.75A)	116
FIGURE 61. RGB (BT3.75, BT10.8, BT12)	117
FIGURE 62. RGB (2.1/1.6, .845, .640)	118
FIGURE 63. RGB (2.1, 1.6, .640)	119
FIGURE 64. RGB (BT3.75, 2.1, 1.6)	120
FIGURE 65. RGB (BT8.6, .640, .845)	121
FIGURE 66. RGB (.86, 1.61, .640)	122
FIGURE 67. RGB (1.61, BT8.6, .640)	123
FIGURE 68. RGB (BT12, BT11, BT8.6).....	124
FIGURE 69. RGB (2.13, 1.38[1.88], 1.66).....	125
FIGURE 70. RGB (1.38[1.88], BT4, 1.61).....	126
FIGURE 71. RGB (.640, 1.61, BT3.75-BT4.0).....	127

Preface

This text introduces the reader to the fundamental principles necessary to manually interpret surface and atmospheric features in multispectral meteorological satellite imagery. The text is aimed at those familiar with integral calculus and offers such individuals detailed insights into the signatures of clouds and land surfaces in both daytime and nighttime imagery along with background material that could be useful in the design of future satellite sensors. Those with a less extensive mathematical background can also become very knowledgeable in the interpretation of multispectral imagery through the careful review of the many examples contained in the text.

Meteorological satellites have been flown by the United States (US) in near-Earth orbit since the launch of Television InfraRed (IR) Observing System (TIROS)-1 in 1960. In the mid-1960s, the US Department of Defense launched its first meteorological satellite under the Defense Meteorological Satellite Program (DMSP). These early satellite sensors collected data in only one broadband visible and one broadband IR channel, e.g. 0.5-1.0 and 10-12 microns (μm) regions of the electromagnetic spectrum (EMS). Early applications of these data included their use in automated cloud models at the US Air Force Weather Central and the manual interpretation of meteorological conditions for weather forecasting. A DMSP User's Guide was the first significant attempt to document the manual interpretation of clouds and weather patterns in meteorological satellite imagery. Several cloud detection problems were associated with these early satellite sensors. Difficulties were experienced in the detection of stratus in nighttime imagery, cirrus clouds in daytime and nighttime imagery, and the differentiation between snow and clouds in daytime imagery.

The Advanced Very High Resolution Radiation (AVHRR) was the first truly operational, multispectral meteorological satellite sensor launched by the US. AVHRR was first carried on the experimental TIROS-N spacecraft in 1978 and became an operational system when flown on the National Oceanographic and Atmospheric Administration (NOAA)-6 spacecraft in 1979. The AVHRR sensor was originally designed to provide improved sea surface temperature (SST) analyses, not improved cloud detection. NOAA scientists postulated in the mid-1970s that SSTs could be analyzed with a 1.0 K accuracy using improved atmospheric corrections made possible by viewing the ocean at two discrete wavelengths within the mid-wave 3.7 and long-wave 10-12 μm regions of the EMS. Thus, the first AVHRR sensor collected data in four spectral bands; one visible channel, and three in the infrared including one mid-IR channel, and the two long-wave IR channels.

Many years after the launch of NOAA-6, new applications continued to be discovered for AVHRR imagery. While the feasibility of retrieving improved SST fields was demonstrated soon after the launch of the AVHRR sensor, there remained the challenge of detecting cloud contamination pixels and removing them from the SST analyses, especially stratus in nighttime imagery and thin cirrus in both daytime and nighttime imagery. In 1984, Wong demonstrated that the contrast between nighttime stratus and ocean surfaces was greatly enhanced in the brightness temperature difference field (BTD) obtained by subtracting the AVHRR 3.7 μm brightness temperatures from the AVHRR 11.0 μm brightness temperatures, i.e. $(\text{BT}_{11.0} - \text{BT}_{3.7})$. The increased contrast resulted from the large difference in emissivity of water droplets in the

stratus clouds at these two wavelengths, even when differences between the temperatures of the surrounding background and the cloud top temperature is negligible. Similarly, Inoue demonstrated in 1985 that the contrast between cirrus and its cloud-free surrounding area is greatly enhanced in the $BT_{11.0} - BT_{12.0}$ feature. Saunders and Kriebel (1988) included these concepts in their new formalism for automated cloud detection that more fully exploited these and other bi-spectral methods to improve cloud detection in SST analyses. Thereafter, NOAA began implementing its own automated cloud analyses model, known as CLouds from AVHRR (CLAVR), based largely upon the work of Saunders and Kriebel, as described by Stowe in 1991.

Recognizing the importance of multispectral imagery for cloud detection was critical to the DMSP Special Program Office (SPO) decision to make its first complete design modification in 30 years. In 1991, the DMSP SPO initiated the DMSP Block 6 program and levied requirements upon competing contractors to design a new system to collect data across the EMS from visible through microwave regions that would allow the accurate retrieval of 22 environmental data records (EDRs) or products. However this program was terminated when the Clinton Administration converged both the NOAA and DMSP into a single US polar-orbiting operational, meteorological satellite system that became known as the National Polar-orbiting Operational Environmental Satellite System (NPOESS). The initial NPOESS system listed requirements for over 60 EDRs to be generated from multiple sensors including imagers and sounders. The electro-optical imager, known as the Visible/Infrared Imager/Radiometer Suite (VIIRS), was required to collect data needed to retrieve 27 NPOESS EDRs. Raytheon Santa Barbara Remote Sensing (SBRS) won the competitive contract in 2000 to build the NPOESS VIIRS sensor. The VIIRS instrument is scheduled to fly on the NPOESS Preparatory Project (NPP) in 2005 and on all NPOESS satellites, commencing with the first NPOESS flight in 2009. VIIRS will collect data in 22 spectral bands in the visible, near-IR (NIR), mid-IR(MIR), and long-wave IR (LIR) regions of the EMS and has its heritage in AVHRR, SeaWIFS, and the MODerate Resolution Imaging Spectroradiometer (MODIS) sensors.

Clearly, recent decades have seen an ever-increasing wealth of information collected by polar-orbiting meteorological satellites that carry multispectral sensors to view the Earth-atmosphere system in a large number of discrete wavelengths. However, no single reference has been written to introduce users of these data to the next generation instrument or help those new to the field to more fully exploit the data once they become available. It is hoped that this text will serve as a useful guide for the VIIRS sensor and the interpretation of VIIRS heritage imagery, especially for those interested in cloud detection and cloud typing under global conditions.

Chapter 1

INTRODUCTION

1.1 PURPOSE

This manual provides information on the fundamental principles used to help design the VIIRS sensor and contains many examples of “expected” VIIRS images collected by numerous, existing sensors having similar bandpass characteristics. The purpose of the text is to assist future users to more fully exploit VIIRS imagery once these data become available. The text provides, in Chapter 2, information on the NPOESS system including the position of NPOESS in the total Earth Observation System of the World Meteorological Organization (WMO). This section also provides background information on NPOESS requirements that must be satisfied with VIIRS data, specific requirements that must require VIIRS imagery, including application-related requirements for manually generated cloud data products. In addition, an overview is provided on the expected value of VIIRS data in the generation of automated, global cloud analyses and forecasts.

Since the NPOESS program defined the characteristics of imagery and identified only a subset of the total VIIRS EDR requirements that must be satisfied by imagery bands, Raytheon designed the VIIRS sensor to collect spectral data at two different resolutions, i.e. nominally 375 m imagery channels and 750 m resolution non-imagery channels (called moderate resolution channels). In this text, moderate resolution bands may be referred to as “Imagery Assist” bands since these data may occasionally be used to better understand the content of the imagery bands while reducing transmission bandwidth required of the entire NPOESS system. Chapter 3 provides insight into the process used to determine which VIIRS bands would be imagery bands and which would be non-imagery bands. This chapter includes the theoretical basis for manual cloud analyses and detailed information on the characteristics of land surface classes, water and ice particle indices of refraction, and atmospheric transmission that produce spectral signatures in VIIRS imagery. Together, all are considered the phenomenology of the channel selection process and provide detailed justification for the imagery and imagery assist bandpasses selected for the VIIRS sensor.

Chapter 4 contains information on the VIIRS sensor hardware design that flows down from the requirements established in Chapter 3.

Chapter 5 provides deeper insight into the spectral signatures contained within each VIIRS (imagery and imagery-assist) spectral band along with examples of expected VIIRS data collected from existing research and operational sensors. The primary focus of this chapter is to demonstrate features that can be identified in each individual spectral band along with ambiguities that require additional spectral data to resolve.

The discussion in Chapter 5 sets the stage for Chapter 6, which demonstrates the use of color composites to view the spectral signatures in multiple bands simultaneously thus

facilitating the rapid manual interpretation of VIIRS imagery. This discussion should greatly assist those interested in the quality control (QC) of global, automated cloud products and possibly others interested in extracting the most detailed information possible on regional scales. Topics in Chapter 6 are cross-referenced in Chapter 7.

1.2 SCOPE

There is no misconception in the authors' minds that this manual is an exhaustive work. The community learned much over the two plus decade lifetime of AVHRR and new applications were being developed toward the end of its lifetime. Even with MODIS flying on the EOS AM and PM missions, it is anticipated that a great deal more will be learned about the Earth-atmosphere system from VIIRS imagery, once the sensor becomes operational, simply from larger numbers of analysts having routine, easy access to these data. Therefore, the authors solicit information from all future VIIRS users of detailed information on applications, including sample images, which can be published in future updates to this text for the benefit of the entire community.

More detailed information is available in the following Raytheon documents for those wishing to acquire it through the NPOESS IPO:

[Y2469] - VIIRS Context Level Software Architecture

[Y2477] – VIIRS Snow/Ice Module Level Software Architecture Document

[Y2478] - VIIRS Build-RDR Module Level Software Architecture Document

[Y2479] - VIIRS Build-SDR Module Level Software Architecture Document

[Y2401] - VIIRS Snow Cover ATBD

[Y2404] - VIIRS Fresh Water Ice ATBD

[Y2405] - VIIRS Ice Surface Temperature ATBD

[Y2409] - VIIRS Sea Ice Age/Edge Motion ATBD

[Y2411] - VIIRS Surface Reflectance ATBD

[Y2412] - VIIRS Cloud Mask ATBD

[Y2466] - VIIRS Imagery ATBD *

[Y3252] – VIIRS Active Fires ATBD

[Y3258] – VIIRS Geolocation ATBD

[Y3261] - VIIRS Radiometric Calibration ATBD

[Y4963] - VIIRS Imagery TIM, March 8, 2000

* - This User's Guide is the appendix to the VIIRS Imagery ATBD

Chapter 2

NPOESS SYSTEM OVERVIEW

2.1 SATELLITES AND SENSORS

The World Meteorological Convention, by which the World Meteorological Organization was created, was adopted at the Twelfth Conference of Directors of the International Meteorological Organization (IMO), which met in Washington, D.C. in 1947. Although the Convention became active in 1950, WMO commenced operations as the successor to IMO in 1951 and, later that year, was established as a specialized agency of the United Nations by agreement between the UN and WMO. The purposes of the 185-member organization are to facilitate international cooperation in the establishment of networks of stations for making meteorological, hydrological and other observations; and to promote the rapid exchange of meteorological information, the standardization of meteorological observations and the uniform publication of observations and statistics. It also furthers the application of meteorology to aviation, shipping, water problems, agriculture and other human activities, promotes operational hydrology and encourages research and training in meteorology. (Ref: WMO web-page)

Among the WMO's major scientific and technical programs is the World Weather Watch (WWW), which is the backbone of WMO's activities. The WWW offers up-to-the-minute world-wide weather information through member-operated observation systems and telecommunication links currently with polar-orbiting [e.g. TIROS (USA), METEOR (Russia), FY (China), etc.] and geostationary satellites [e.g. GOES-E/W (USA), GMS (Japan), Meteosat (EUMETSAT), etc.] as shown in Figure 1. Table 1 provides an overview of the key satellites and sensors that have supported the WMO's modern WWW program since 1980. (Ref: WMO web-page)

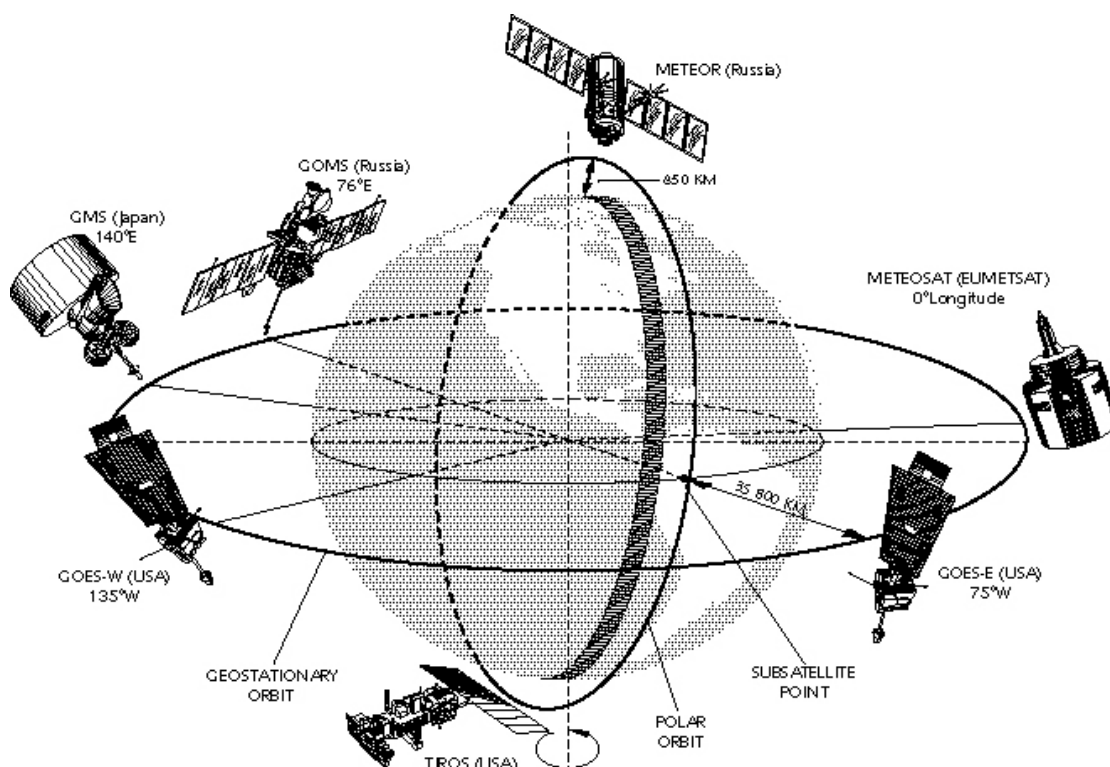


Figure 1. Meteorological satellites supporting the WMO World Weather Watch Program.
(Figure taken from WMO website)

The WWW also provides information from about 10,000 land observations and 7,000 ship stations and 300 moored and drifting buoys carrying automatic weather stations. Each day, high-speed links transmit over 15 million data characters and 2,000 weather charts through 3-World, 35-Regional and 183-National Meteorological Centers cooperating with each other in preparing weather analyses and forecasts. It is through WMO that the complex agreements on standards, codes, measurements and communications are established internationally. (Ref: WMO web-page)

Table 1. Recent Satellites and Sensors Supporting the WMO's WWW Program.
(To be completed in a later version.)

Name	Country	Launch	Key Meteorological Instruments
FY - 1	China		
FY - ...	China		
GOES - I	USA		
GOES -	USA		
GOMS	Russia		
INSAT	India		
GMS -	Japan		
METEOR -	Russia		
METEOSAT -	Europe		
TIROS -	USA		

US support to the WWW program will transition from TIROS to NPOESS with the scheduled launch of NPOESS-1 in 2009. Current plans call for NPOESS to fly three spacecraft in sun-synchronous orbits at nominal altitudes of 833 KM with nodal times of 0530 (1730), 0930 (2130), and 1330 (0130). VIIRS is a key sensor and will be carried on every NPOESS satellite. With a nominal data swath width of 3000 km, VIIRS will provide contiguous coverage at the equator every four hours. In addition, VIIRS will also fly on the NPOESS Preparatory Program (NPP) spacecraft scheduled for launch in 2005. The NPP spacecraft is a transitional system that will fill the gap between NASA's Earth Observing Systems (AM and PM) spacecraft and the first NPOESS satellite. It is not yet known whether the NPP data will support the WMO WWW program but the NPP spacecraft will carry a direct broadcast capability. A list of planned NPOESS launches and payloads is shown in Table 2. In addition to the VIIRS, other key NPOESS sensors include the Cross-track Infrared Sounder (CrIS), Conical Scanning Microwave Imager Sounder (CMIS), Ozone Mapping and Profiler Suite (OMPS), GPS Occultation Sensor (GPSOS), and the Space Environmental Sensor Suite (SESS). In addition, a cross-track microwave sensor, known as the Advanced Technology Microwave Sounder (ATMS), will be carried on the NPP satellite(s).

Table 2. Planned Launches of NPOESS Satellites and Sensor Configurations.
(To be completed in a later version.)

Name	Scheduled Launch	Key Meteorological Instruments
NPP – 1	2005	VIIRS, CrIS, ATMS,
NPP - 2 (optional)		
NPOESS – 1	2009	VIIRS, CrIS, CMIS,
NPOESS – 2		
NPOESS – 3		
NPOESS – 4		
NPOESS -		

2.2 PRIMARY VIIRS EDR REQUIREMENTS

The US Departments of Commerce and Defense as well as NASA created the NPOESS Integrated Program Office (IPO) to develop, acquire, manage, and operate the next generation of US polar-orbiting, operational, environmental satellites. The VIIRS sensor was designed to collect data sufficient to create EDRs that comply with specifications defined by the NPOESS IPO. The following EDRs and Application-Related Requirements (ARRs) are VIIRS requirements:

- Imagery (except microwave imagery) (Appendix D, Sec. 40.2.3)
- Sea Surface Temperature (Appendix D, Sec. 40.2.4)
- Soil Moisture (Appendix D, Sec. 40.2.6)
- Aerosol Optical Thickness (Appendix D, Sec. 40.3.1.1)

- Aerosol Particle Size Parameter (Appendix D, Sec. 40.3.1.2)
- Suspended Matter (Appendix D, Sec. 40.3.1.3)
- Cloud Base Height (Derived) (Appendix D, Sec. 40.4.1)
- Cloud Cover/Layers (Appendix D, Sec. 40.4.2)
- Cloud Effective Particle Size (Appendix D, Sec. 40.4.3)
- Cloud Optical Thickness (Appendix D, Sec. 40.4.6)
- Cloud Top Height (Derived) (Appendix D, Sec. 40.4.7)
- Cloud Top Pressure (Derived) (Appendix D, Sec. 40.4.8)
- Cloud Top Temperature (Appendix D, Sec. 40.4.9)
- Albedo (Surface) (Appendix D, Sec. 40.5.2)
- Land Surface Temperature (Appendix D, Sec. 40.6.1)
- Vegetation Index (VI) (Appendix D, Sec. 40.6.2)
- Snow Cover/Depth (Appendix D, Sec. 40.6.3)
- Surface Type (Appendix D, Sec. 40.6.4)
- Ice Surface Temperature (Appendix D, Sec. 40.7.3)
- Net Heat Flux (Derived) (Appendix D, Sec. 40.7.5)
- Ocean Color/Chlorophyll (Appendix D, Sec. 40.7.6)
- Sea Ice Age/Edge Motion (Appendix D, Sec. 40.7.8)
- Fresh Water Ice ARR (Appendix D, Sec. 40.7.8.1)
- Active Fires (ARR)
- Precipitable Water (Appendix D, Sec. 40.3.3.) (primary for CMIS, an augmented product for VIIRS)

Listed in parentheses following each data product is a reference to a section of Appendix D to the NPOESS Technical Requirements Document (NPOESS TRD, 2001). The TRD specifies NPOESS system-level requirements that must be satisfied, possibly using data acquired by more than one NPOESS sensor. Thus, in some cases, VIIRS data may be used with additional data derived from other (non-VIIRS) sources, including other NPOESS sensors, conventional weather observations, or output from weather forecast models, to produce data products that meet the NPOESS EDR requirements. Thus, the NPOESS system represents the first US operational environmental satellite that has been specifically designed by the user community represented by the IPO to meet a complete set of EDR or data product requirements.

2.3 VIIRS IMAGERY EDR REQUIREMENTS

The first user-requirement identified in the VIIRS SRD defines the specifications for the Imagery EDR. (Section 40.2.3 in Appendix D of the TRD exempts microwave imagery from this requirement.) Imagery collected by polar-orbiting environmental satellites have long been used in operational meteorology, e.g. to evaluate automated cloud analyses and forecast products, as discussed later in this chapter. Thus, the NPOESS user community listed Imagery as a top EDR requirement to ensure VIIRS data were of sufficient quality to support their missions.

The VIIRS SRD states that Imagery EDR requirements fall into three classes: (a) explicit requirements on the EDR content, quality, reporting frequency, and timeliness; (b) application-related requirements based on utilizing the imagery EDR, such as manual generation of cloud and sea ice data; and (c) derived requirements to be derived by the VIIRS contractor based on requirements for other EDRs supported by the imagery. A brief overview of these requirements includes:

- (1) Explicit EDR Requirements for each Imagery band includes the following two data products, both generated by ground processing of VIIRS data:
 - (a) a two-dimensional array of locally averaged absolute in-band radiances at the top of the atmosphere measured in the direction of the viewing instrument, and
 - (b) the corresponding array of equivalent blackbody temperatures (EBBT) if the band is primarily emissive, or the corresponding array top-of-the-atmosphere (TOA) reflectances if the band is primarily reflective during daytime. The form of the spatial weighting function that determines the local averaging of the absolute TOA radiance is constrained by the Horizontal Spatial Resolution (HSR) requirement. The number of spectral bands, band limit values, measurement ranges, and measurement uncertainty (or accuracy and precision) requirements are to be derived based on the manually-generated, application-related requirements and on the requirements of other EDRs supported by the imagery.
 - (c) In addition to these products, the Imagery EDR includes a daytime/nighttime visible imagery product that maintains apparent contrast under daytime, nighttime, and terminator region illumination conditions.
 - (d) At a minimum, at least one daytime visible, one daytime/nighttime visible, and one IR channel shall meet the explicit imagery requirements.
- (2) Application-related Imagery requirements are based on specific applications utilizing the imagery EDR, such as manual-generation of cloud and sea ice data as outlined in the next section.
- (3) Derived Imagery requirements are requirements necessary to satisfy threshold requirements of other “primary” EDRs supported by the imagery.

All VIIRS spectral bands that are classified as imagery channels in order to meet the explicit, applications-related, or derived Imagery EDR requirements listed above must

also meet the additional requirements shown in Table 3. Thresholds are considered minimum acceptable NPOESS system-level performance requirements and objectives are preferred NPOESS system-level performance requirements. Typically, much more stringent design requirements and significantly increased costs are needed to attain Objective performances levels. For example, worst-case Horizontal Spatial Resolution decreases from 0.8 km for the Threshold requirement to 0.1 km for the Objective requirement at the VIIRS edge of scan. Obviously, the much higher resolution of this Objective requirement would greatly increase both hardware design costs, to measure sufficient energy 1500 km from nadir and to store much larger data sets on-board the satellite, as well as increased communication costs, associated with the transmission of a much larger data volume to the satellite operations ground station.

Table 3. Attribute Requirements for Each VIIRS Band Classified as Imagery.

Para. No.	Attribute	Thresholds	Objectives
	a. Horizontal Spatial Resolution (HSR), both in-track and cross-track		
V40.2.3.1-2	1. At nadir	0.4 km	(TBD)
V40.2.3.1-3	2. Worst case	0.8 km	0.1 km
V40.2.3.1-6	5. Daytime/Nighttime Visible, worst case	2.6 km	0.65 km
V40.2.3.1-7	b. Horizontal Reporting Interval	Derived (gapless or near gapless coverage required)	Derived (gapless or near gapless coverage required)
	c. Horizontal Coverage	Global	Global
	d. Measurement Range		
V40.2.3.1-11	1. Daytime/Nighttime visible	4E-9 - 3E-2 W/cm ² -sr (TBR) in 0.4-1.0 mm band, or equivalent in another band	Includes threshold range
V40.2.3.1-12	2. Other bands	Derived	Derived
V40.2.3.1-13	e. Measurement Uncertainty	Derived	Derived
	f. Mapping Uncertainty		
V40.2.3.1-14	1. At nadir	3 km	(TBD)
V40.2.3.1-15	2. Worst case	4 km	0.5 km
	g. Maximum Local Average Revisit Time	4 hrs	(TBD)
	h. Maximum Local Refresh	6 hrs	(TBD)
	i. Fraction of Revisit Times Less Than a Specified Value	At any location at least 75% of the revisit times will be 4 hours or less.	(TBD)
V40.2.3.1-16	j. Minimum Swath Width (All other EDR thresholds met)	3000 km (TBR)	(TBD)

Thus, VIIRS Imagery requirement specifies that: (a) at least one daytime visible, nighttime visible, and IR band will be Imagery channels, (2) all bands needed to meet Threshold requirements for manually-generated cloud and sea ice analyses will be

Imagery channels, and (3) any band that requires Imagery attributes listed in Table 3 to meet the Threshold requirements of another VIIRS EDR will be an Imagery channel.

2.4 VIIRS APPLICATION-RELATED IMAGERY REQUIREMENTS

As noted above, the VIIRS SRD states that the content and quality of VIIRS Imagery shall be adequate to allow application-related requirements to be satisfied. These requirements include manually-generated cloud and manually-generated sea ice data. The requirement for manually-generated cloud analyses includes the capability to detect or identify clouds and manually classify them as discussed below. *Therefore, a primary goal of this Guide is to demonstrate the capability and procedures to manually detect and classify clouds in spectral data similar to those identified as VIIRS Imagery bands.*

- Manually Generated Cloud Data, i.e. manually generated cloud data are estimates of cloud cover and cloud type generated by a trained human analyst viewing the unprocessed and/or processed imagery derived from the unprocessed imagery, e.g., by data fusion, spatial re-scaling, image enhancement, etc.

- Cloud Type defined as follows:

- (1) Altocumulus (AC)
- (2) Altocumulus Castellanus (ACCAS)
- (3) Altocumulus (Standing lenticular) (ACSL)
- (4) Altostratus (AS)
- (5) Cirrocumulus (CC)
- (6) Cirrocumulus (Standing lenticular) (CCSL)
- (7) Cirrostratus (CS)
- (8) Cirrus (CI)
- (9) Cumulonimbus (CB)
- (10) Cumulus (CU)
- (11) Cumulus Fractus (CUFRA)
- (12) Towering Cumulus (TCU)
- (13) Stratus Fractus (STFRA)
- (14) Nimbostratus (NS)
- (15) Stratocumulus (SC)
- (16) Stratocumulus (Standing lenticular) (SCSL)
- (17) Stratus (ST)

Cloud typing not only entails a capability to distinguish between clouds of different type, but also a capability to distinguish clouds from other features, such as snow, cold water, cold land, haze, smoke, dust, etc. Therefore, the following additional types are defined:

- (18) Obscured/not cloudy
- (19) Clear

- Sea Ice Data. Sea ice data may be generated interactively by a trained human analyst viewing unprocessed or processed imagery at a computer workstation, or automatically via an algorithm. In addition to determination of ice edge location and ice concentration as described below, analysts will attempt to determine the thickness and size of leads and polynyas based on the imagery.
- Ice Edge Location and Ice Concentration. An ice edge is defined as the boundary between ice-covered sea water (ice concentration > 0.1 (TBR)) and sea water not covered by ice (ice concentration ≤ 0.1 (TBR)). Ice concentration is defined as the fraction of a given area of sea water covered by ice. An ice edge is typically provided as a contour on a map or in digital form as a set of latitude/longitude coordinates. The ice edge location error is defined as the distance.

2.4.1 Cloud Cover

The NPOESS requirements for manually-generated cloud cover are shown in Table 4. Cloud cover is defined as the fraction of a given area, i.e., of a horizontal cell, on the Earth's surface for which a locally normal line segment, extending between two given altitudes, intersects a detectable cloud. For manual analyses, cloud cover is estimated for a single atmospheric layer. Specifically, the minimum and maximum altitudes of this layer are defined to be the surface of the Earth and the altitude where the pressure is 0.1 mb. Haze, smoke, dust, and rain are not to be considered clouds. For the purpose of validating this requirement, cloud cover estimates are to be generated by a trained human analyst viewing unprocessed and/or processed imagery for contiguous square areas having side length equal to the horizontal cell size specified below.

Thus, the requirement for the manually-generated cloud cover EDR translates into identifying the minimum set of VIIRS Imagery channels needed to accurately differentiate between cloud and cloud-free pixels under a global set of conditions. "Accurately" is defined by the attributes listed in Table 4. From a sensor design perspective, this requirement includes quantifying the spatial, spectral, and sensor (e.g. noise) model needed to meet the Threshold requirements. Chapter 3, "Theoretical Basis for Manual Cloud Analyses," demonstrates the procedures used to define the VIIRS design parameters needed to satisfy requirements for the manually-generated cloud cover EDR.

Table 4. NPOESS requirements for Manually-Generated Cloud Cover EDR.

Para. No.	Attribute	Thresholds	Objectives
V40.2.3.2.1.1-6	a. Horizontal Cell Size	3 (TBR) times the Imagery HSR	2 times the Imagery HSR
V40.2.3.2.1.1-3	b. Horizontal Reporting Interval	Horizontal cell size	Horizontal cell size
V40.2.3.2.1.1-4	c. Measurement Range	0 - 1, 0.1 increments	0 - 1, 0.1 increments
V40.2.3.2.1.1-5	d. Measurement Uncertainty	0.1	0.1

2.4.2 Cloud Type

The NPOESS Requirements for the manually-generated cloud type EDR are shown in Table 5. For the purpose of validating this requirement, typing is to be performed by a trained human analyst viewing unprocessed and/or processed imagery for contiguous square areas having side length equal to the horizontal cell size specified below. The probability of correct typing is defined as the probability that a cell reported as being of type x is in fact of type x, where x is any of the 19 cloud types specified above.

Table 5. NPOESS requirements for Manually-Generated Cloud Type EDR.

Para. No.		Thresholds	Objectives
V40.2.3.2.1.2-7	a. Horizontal Cell Size	(TBD) times Imagery HSR	(TBD) times Imagery HSR
V40.2.3.2.1.2-3	b. Horizontal Reporting Interval	Horizontal cell size	Horizontal cell size
V40.2.3.2.1.2-4	c. Measurement Range	Clear, obscured/not cloudy, ST, CU, CI	Clear, obscured/not cloudy, all 17 cloud types
V40.2.3.2.1.2-8	d. Probability of Correct Typing	85 % at 95 % (TBR) confidence level	90 % at 95 % (TBR) confidence level

During the design phase of the VIIRS project, it was demonstrated that only three spectral channels were required to satisfy the threshold requirements for the VIIRS Imagery Application-Related manually-generated cloud products. These bands included one visible ($\sim 0.64 \mu\text{m}$), one mid-IR ($\sim 3.74 \mu\text{m}$), and one longwave-IR ($\sim 11.45 \mu\text{m}$). With the additional NPOESS-Explicit EDR requirement for a nighttime visible Imagery band and derived requirements for imagery resolution bands at $0.865 \mu\text{m}$ and $1.6 \mu\text{m}$, there became six total imagery resolution channels in the VIIRS sensor design.

From Table 3, it is seen that VIIRS imagery bands must have a NADIR resolution of no worse than 400m – the VIIRS design is 375 m. This resolution must be near-constant in the cross-track direction, i.e. it can degrade to no worse than 800 m at edge of scan. (Typically, AVHRR Local Area Coverage degrades from a nominal 1.1 km at nadir to over 5 km at edge of its scan.)

All remaining bands needed to support retrieval of VIIRS EDRs shown in Section 2.2 are called moderate resolution bands. For the purpose of constructing manually-generated cloud analyses, they are referred to as “*Imagery-Assist*” (IA) bands. The importance of

IA bands are two fold: (1) it is possible to achieve much higher signal to noise with moderate resolution bands, since the horizontal spatial resolution of 750 m at NADIR is double that of the imagery bands and (2) lower bandwidth is needed to transmit data collected in moderate resolution bands compared to imagery bands. Several bands were required both very high-resolution and very high signal-to-noise. In such instances, two channels were built into the VIIRS design for a single bandpass, i.e. the 1.6 μ m band exists as both an imagery and moderate resolution band to satisfy all VIIRS Threshold requirements. While it is an NPOESS requirement that VIIRS imagery bands satisfy threshold requirements for the Imagery EDR, moderate resolution bands can be used with imagery bands to meet Objectives requirements for VIIRS EDRs. Using Imagery and IA together is demonstrated in Chapter 6.

2.5 VALUE OF MANUALLY-GENERATED CLOUD ANALYSES

Manually-generated cloud analyses can serve several important functions in operational meteorology. Cloud cover analyses generated from the human interpretation of multispectral imagery can be defined as “ground truth” and then used to make quantitative comparisons with the results obtained with automated cloud analysis algorithms or models. In addition, manual analyses can be used to validate the accuracy of cloud forecast models or other numerical weather prediction models by creating manual analyses of imagery coincident with forecast verification time.

2.5.1 Performance Verification of Automated Cloud Models

In the 1990 timeframe, cloud cover analyses were generated from OLS imagery collected by the DMSP satellite series and ingested into the Real-time Cloud Nephanalysis (RTNEPH) Model (Keiss and Cox, 1985) at Air Force Weather Agency (AFWA). These automated cloud analyses were then used to initialize a cloud forecast model known as the High Resolution Cloud Prognosis (HRCP). The goal of the Cloud Model Enhancement Program (CMEP) was to determine the accuracy of the HRCP model and identify enhancements to improve the accuracy of forecasts. To accomplish the task, raw satellite imagery, automated cloud analyses, and automated cloud forecasts were collected for two, 30 day periods. Manual cloud analyses were generated for each satellite image. These ground truth cloud, no cloud (CNC) analyses were compared against time-coincident automated cloud analyses and forecasts. Sample results from this study are shown in shown Figure 2 for the 0-hour cloud analysis used to initialize the HRCP model and 3-hour HRCP cloud forecast. Similar results were obtained at each of the HRCP forecast verification times, e.g. covering 24 hours at 3-hour intervals.

Figure 2 shows that the RTNEPH failed to detect clouds, especially in regions that were less than 50% cloud covered. It was not a surprise to find that the under-specification of cloud cover in the 0-hour analysis resulted in an under-specification of clouds at each of the HRCP forecast verification times. This ability to manually detect clouds and create highly accurate CNC analyses from DMSP imagery allowed scientists to quantitatively evaluate automated cloud forecast model performance and resulted in a major improvement in cloud forecast accuracy, according to Air Force personnel. In addition,

quantifying the impact of automated cloud analysis on performance of the HRCF model led to a program initiative, known as the Cloud Depiction and Forecast System (CDFS) II project, to update the RTNEPH cloud analysis model (Hutchison and Janota, 1989).

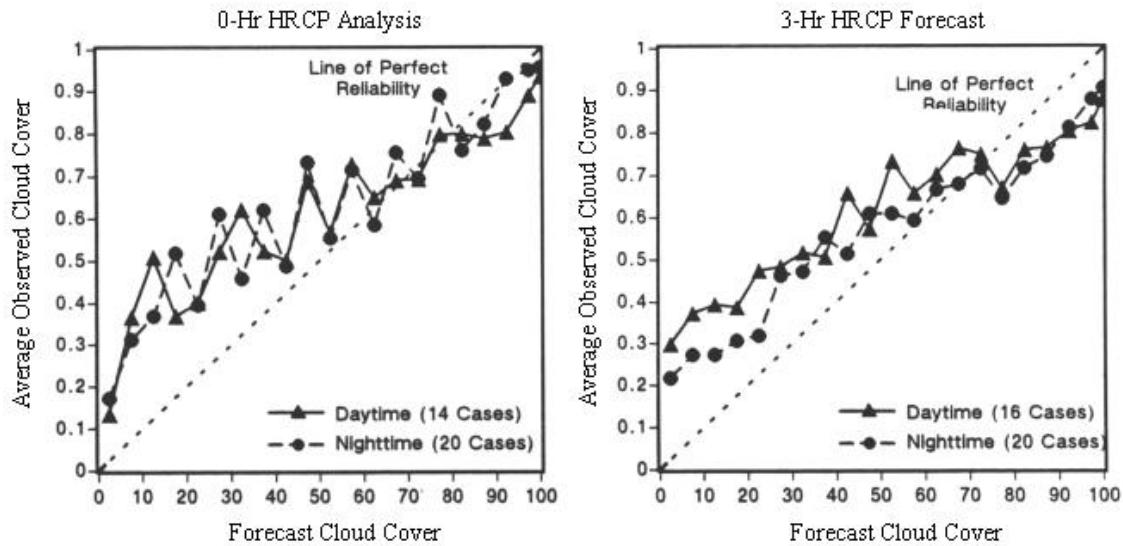


Figure 2. HRCF Cloud Forecast Reliability Established During 1990 CMEP Study (Hutchison and Janota, 1989).

2.5.2 Quality Control of Automated Cloud Analyses

While providing VIIRS imagery for manually-generated cloud analyses has great value to quantify performance of cloud forecast models, *the primary use of VIIRS imagery at the Air Force Weather Agency (AFWA) is to quality control (QC) automated cloud analyses, not to generate manual CNC analyses. Therefore, the implied VIIRS requirement for manually-generated cloud products is to provide imagery that supports the QC of automated cloud analysis models in a highly time-constrained environment.* The typical sequence of steps in the generation of automated cloud forecasts at AFWA includes:

- 1) Data ingestion functions:
 - Process imagery by the satellite processing mainframe computer
 - Process the imagery into the Satellite Data Handling System (SDHS)
- 2) Generate Automated Cloud Analysis
 - Generate cloud analysis with the RTNEPH Model

- Manual Quality Control (QC) of the RTNEPH analyses (referred to in the literature as the so-called “RTNEPH Bogus”)

3) Generate Automated Cloud Forecasts

- ADVCLD (Five-Layer) long range forecast model (+03 to +33 hours)
- HRCP (High-Resolution Cloud Prognosis) short range cloud forecast model
- Manual QC of Forecast Products (the so-called “Forecast Bogus”)

The entire process is nominally accomplished within a 55-minute timeline. The “clock” starts when the DMSP spacecraft begins transmitting data to the command readout site. Based upon the DMSP system, data ingestion typically requires 2-3 minutes. Automated cloud analysis is accomplished in another 5 minutes. Preparation for the RTNEPH Bogus occasionally begins prior to data readout (e.g., pre-mapping grid coordinates to satellite image space). The manual QC (Bogus) process is allocated 15 minutes, with generally two quarter-orbits of data being processed in parallel. At Bogus completion, approximately +22 minutes, RTNEPH edits are sent to the satellite processing mainframe to update the RTNEPH database. This database is used to initialize the various forecast models. Output cloud cover forecasts are displayed on the SDHS over the DMSP imagery alongside ancillary forecast aids (e.g., height, temperature, and moisture fields) and reviewed for correctness by forecasters. Forecast edits are retransmitted to the satellite processing mainframe for database update and final forecast product generation.

Historically, the RTNEPH Bogus on the SDHS was accomplished by displaying only two DMSP channels of smooth (1.5 nautical miles) broadband infrared and visual imagery for a quarter-orbit of data simultaneously on two monitors at 1024x1024 resolution in the nominal satellite projection. Up to four sets of these displays are ‘scanned’ in sequence from the northernmost to the southernmost sections of the quarter-orbit. A third monitor displays a 4:1 reduced view of the entire quarter orbit to provide the analyst with an overview of the entire scene. On the high resolution monitors, digits are displayed over the imagery at RTNEPH grid point locations to represent the automated cloud cover analysis. Only total cloud amount, in eighths, is displayed. Cloud cover of zero eighths is not displayed to emphasize distinctiveness of clear-cloud regions. Because digits are spaced closely in image space (typically no more than 16 pixels from center to center), a special character set is used to display digits with a minimum number of pixels. Additionally, the capability to toggle digits on or off rapidly is available.

Analysts use a multiple monitor slaved draw mode with a digitizing tablet to circumscribe cloud edits around sets of digits which are deemed unrepresentative of the true cloud field. Each single cloud edit label takes the form of a closed curve and may include up to three pairs of cloud amount and cloud type; one each for low, middle and/or high clouds. For example, one Bogus label might include 3 eighths of cumulus, 5 eighths of altocumulus, and 6 eighths of cirrus. Analysts generally estimate lower altitude cloud amounts based on their meteorological understanding of the scene. The RTNEPH bogus edit post-processor uses cloud type labels to assign default cloud base and top altitudes.

After a review of the displayed 1024x1024 frame for the quarter orbit is complete, another analyst performs a “quick” review of the edits; then, QC of the next frame of the quarter-orbit begins. The QC time schedule only allows the analyst approximately 2-3 minutes per 1024x1024 frame to ensure that a single quarter-orbit is processed within the required timeline. At the end of the allotted time or when the quarter orbit is completely reviewed, all edits are concatenated and shipped to the satellite processing mainframe to update the database. A hardcopy of the edits is generated and filed for subsequent review. Given the typical 15-minute time budget to review and correct a quarter orbit cloud analysis, the analysts typically are reviewing and correcting 1.5 million square kilometers per minute.

The integration of NPOESS data in general, and VIIRS data in particular, will significantly improve this cloud analysis and forecast system. Expected enhancements include:

- *The use of VIIRS imagery will significantly improve the quality of automated cloud analyses, resulting in fewer operations being needed to perform the QC, Bogus function.* Earlier studies quantified the accuracy of the cloud forecast system at AFWA and recommended further improvements in the cloud analysis and forecast system (Hutchison and Janota, 1989; Hutchison et al., 1990). Recommended enhancements were made to the cloud forecast models and subsequently the time required to perform QC on the automated cloud forecasts became negligible. These studies concluded that “After the recommended enhancements to cloud forecast models were made, the next major step necessary to improve the cloud forecast accuracy was to upgrade the cloud analysis model.” Subsequently, the Support of Environmental Requirements for Cloud Analysis and Archive (SERCAA) Program was undertaken to improve automated cloud analyses; however, these algorithms must continue to rely upon existing meteorological satellite DMSP, Television Infrared Observation Satellite (TIROS), and Geostationary Operational Environmental Satellite (GOES) data which have inadequate spectral data for generating highly accurate, global cloud analyses. Therefore, significant improvement in cloud detection accuracy will be possible with the added spectral data provided by VIIRS and improved automated cloud analyses will result after the cloud forecast system in AFWA is upgraded to process these NPOESS data.
- *The use of VIIRS imagery will provide analysts with the capability to more readily distinguish between clouds and cloud-free surfaces, using color composites, which will improve the speed and accuracy of the QC, Bogus processes.* During the NPOESS era, at a minimum, it is expected that all current SDHS terminals be upgraded to display VIIRS imagery as color composites (i.e. different VIIRS imagery channels, imagery assist channels, channel differences, and/or channel ratios assigned to each gun of a color display) to exploit the unique spectral signatures of cloud and backgrounds and enhance the analysts capability to quickly and accurately perform the QC process on automated cloud analyses. As experience is gained in using and

interpreting these color composites, the capability to more accurately and quickly quality control the automated analyses will be possible using a minimum of VIIRS color composites. *Again, it is a primary purpose of this manual to provide future users of VIIRS imagery with the fundamental knowledge and skills of image interpretation to fully exploit the spectral signatures in VIIRS imagery and improve support to various missions, including overall performance of the CDFS II system.*

Attention now turns to the primary focus of this text, which is to analyze the spectral signatures of clouds and various cloud-free surfaces in VIIRS channels. The analysis will include a brief overview of the phenomenology that characterizes signatures of clouds and surface features in meteorological satellite imagery and sample imagery of each VIIRS band that demonstrates this theory. A thorough representation of this phenomenology is important to fully understand the fundamental principles of meteorological satellite interpretation. Mastery of this basic knowledge will allow users of VIIRS imagery to apply these concepts to their unique applications that will ultimately extend the information base provided in this text. It is our hope that future users of VIIRS data will freely share their new knowledge with us so we may include additional applications in future revisions of this text.

Chapter 3

THEORETICAL BASIS FOR MANUAL CLOUD ANALYSES

3.1 PHYSICS OF THE PROBLEM

The ability to manually identify clouds in any given spectral band is based upon the contrast, measured in radiance, between the cloud and the surrounding cloud-free background. More precisely:

$$C = I_v(0)_{\text{cloud}} / I_v(0)_{\text{background}} \quad (1)$$

Depending upon the wavenumber (ν) of energy viewed by a given channel of the VIIRS sensor, the top of the atmosphere (TOA) radiance, $I_v(0)$, may be composed of reflected solar radiation, emitted thermal radiation, or both solar and thermal radiation when observations are made in the 3-5 μm wavelength interval under daytime conditions.

For simplicity, consider the case of thermal (infrared) radiation as a narrow (monochromatic) beam of energy emitted from a surface through a cloud-free atmosphere to space. The monochromatic, upwelling infrared energy arriving at the aperture of the VIIRS sensor is given by (Liou, 1980, p. 247):

$$I_v(0) = \varepsilon_v B_v[T_s] T_v(p_s) + \int_{p_s}^0 B_v[T(p)] \frac{\partial T_v(p)}{\partial p} dp + (1 - \varepsilon_v) \int_0^{p_s} B_v[T(p)] \frac{\partial T_v(p)}{\partial p} dp \quad (2)$$

- where: ν = wavenumber of emission
 $B_v[T(p)]$ = Planck function at wavenumber (ν) for temperature (T) in K°
 ε_v = emissivity of surface at wavenumber (ν)
 $T_v(p_s)$ = atmospheric transmittance between pressure level (p_s) and space
 $I_v(0)$ = monochromatic radiance arriving at satellite.
 p_s = surface pressure
 T_s = surface temperature

For imaging sensors, as opposed to sounders, the difference in atmospheric transmittance between adjoining pressure levels (p) is very small which makes the atmosphere a secondary source of energy arriving at the sensor, as described in the integral terms in Equation (2). Thus, for the purpose of creating a manual cloud analysis, Equation (2) may be closely approximated by:

$$I_v(0) = \varepsilon_v B_v[T_s] T_v(p_s) \quad (3)$$

Equation (3) states that the vast majority of energy arriving at the satellite sensor is dependent on three primary components: the Blackbody emission from the Earth's

surface, the emissivity of the surface, and the atmospheric transmission from the surface to the sensor.

Planck's Law for blackbody radiation defines the total energy of the emission as a function of monochromatic wavelength and surface skin temperature (Liou, 1980, p. 9). The emissivity is unity if the surface obeys the Laws for Blackbody radiation and less than unity otherwise as described by Kirchoff's Law (Liou, 1980, p. 12). The transmission is unity if the atmosphere is completely transparent at the wavelength (ν), exactly zero if the atmosphere completely absorbs all energy emitted by the surface at the wavelength (ν), and greater than zero but less than unity otherwise, as is typically the case. A similar equation can be written when the feature is a thick (blackbody) cloud rather than a cloud-free surface. In the cloudy case, the emissivity and temperature represent the cloud top rather than the surface and atmospheric transmissivity refers to the column of air extending from the cloud top to TOA.

For the case of solar radiation, the amount of monochromatic energy reflected by the Earth-atmosphere system into the sensor aperture is far more complex and given by Equation (4) as described by Liou (1980, p. 25):

$$I(0; \mu, \phi) = I(\tau_1; \mu, \phi) e^{-\tau_1 / \mu} + \int_0^{\tau_1} J(\tau'; \mu, \phi) e^{-\tau_1 / \mu} \frac{d\tau'}{\mu} \quad (4)$$

Term A Term B

where:

$I_\nu(0)$	= monochromatic radiance arriving at satellite
τ	= optical depth of each τ' layer, while the atmosphere is τ_1 thick
Term A	= surface energy contribution attenuated to space
Term B	= internal atmospheric contributions attenuated to space
μ	= cosine of angle between radiation stream and local zenith angle
ϕ	= azimuth angle.

The complexity of this calculation lies in the source function term, $J(\tau; \mu, \phi)$, which is described for solar radiation by Liou as (1980, p. 178):

$$J(\tau, \mu, \phi) = \frac{\omega}{4\pi} \int_0^{2\pi} \int_{-1}^1 I(\tau, \mu', \phi) P(\mu, \phi; \mu', \phi) d\mu' d\phi' \quad (5)$$

Term C

$$+ \frac{\bar{\omega}}{4\pi} \pi F_0 P(\mu, \phi; -\mu_0, \phi_0) e^{-\tau/\mu_0}$$

Term D

where:

Term C = multiple scattering of diffuse (scattered) energy

Term D = single scattering of direct solar irradiance, F_0 .

and:

ω = single scattering albedo

P = phase function

F_0 = solar irradiance

μ_0 = cosine of solar zenith angle

ϕ_0 = solar azimuth angle

In reality, monochromatic radiation does not exist because of line broadening from natural, pressure (collision), and Doppler (thermal velocity) effects. Also, since an instrument can distinguish only a finite bandwidth, the upwelling radiance measured by the satellite is integrated over the sensor transmission filter, which is also called the sensor response function, and is given by (Liou, 1980, p. 246):

$$I_v(0) = \int_{v_1}^{v_2} [I_v(0)_v dv] / \int_{v_1}^{v_2} \phi_v dv \quad (6)$$

where: ϕ_v = filter (sensor) response function at wavenumber (v)

v_1, v_2 = wavenumber range of filter response

In summary, the capability to manually detect a cloud in thermal (infrared) imagery is enhanced under the following conditions:

- (1) exploiting strong temperature contrasts between the cloud and its surrounding background in a single infrared channel in which the emissivities of the cloud and the surface are nearly the same,
- (2) viewing the cloud and its surrounding background that have the same temperature in a spectral band in which the cloud and background have significantly different emissivities, and

- (3) viewing features in a band in which atmospheric transmissivity is much less than unity such that the surface feature is masked by the atmosphere but the cloud is not.

The capability to manually detect a cloud in solar imagery is enhanced under the following conditions:

- (1) exploiting strong contrasts in reflectivity between the cloud and its surrounding background in a single channel,
- (2) viewing features in a band in which atmospheric transmissivity is much less than unity such that the surface feature is masked by the atmosphere but the cloud is not. The latter case is typical of the phenomenology exploited in the 1.378 μm channel, which suppresses the signatures of low-level cloud and surfaces features, and thus enhances the signatures of higher level clouds.

Finally, the capability to manually distinguish a cloud from its surrounding background is also enhanced by viewing the features in multiple spectral bands where the cloud and surface emissivities or reflectivities are significantly different. Examples of these cases will be shown in Chapter 5.

3.2 DEFINITION OF CLOUD TRUTH DATA SETS

It is now apparent that the VIIRS sensor must include bandpasses in which major cloud types emit or reflect energy with characteristics that are significantly different from the major surface classes to support manually-generated cloud data analyses. Before examining the phenomenology needed to select VIIRS bandpasses, it is useful to examine the methodology used in the VIIRS sensor design phase to quantify the accuracy of manually-generated cloud analyses based upon simulated VIIRS imagery.

The process of quantitatively defining the accuracy of manually-generated cloud analyses requires the creation of cloud “truth” data sets. There are two methods frequently used to create cloud truth data sets: (1) build ground truth by “manually-generating” CNC analyses from the human interpretation of clouds in multispectral imagery, preferably using temporally and spatially coincident imagery of much higher resolution than the sensor being evaluated, e.g. use 30 m Landsat imagery to create a ground truth CNC analysis for a coincident 375 m VIIRS scene, and (2) define ground truth by “constructing” a synthetic CNC map which is then used as an input field to simulated VIIRS imagery for a particular sensor model. Examples of both are provided since the VIIRS sensor design process used “constructed” ground truth CNC masks as input fields to simulate numerous sets of synthetic VIIRS images for a variety of scenes and VIIRS sensor models. Human interpretation of each simulated VIIRS data set produced a “manually-generated” CNC analysis. Pixel-by-pixel comparisons between the “truth” and “manually-generated” CNC analyses quantitatively determined conformance of the VIIRS Imagery and sensor model with NPOESS Threshold and Objective requirements. The preferred VIIRS sensor model and required number of VIIRS Imagery bands was the most cost-effective model that provided the human analyst with the capability of

constructing manually-generated cloud analyses that conformed to NPOESS Threshold requirements. Attention now turns to the process used to create “manually-generated” CNC analysis from synthetic VIIRS imagery.

3.2.1 Cloud Truth from Manual Interpretation of Multispectral Imagery

It is possible to create a manually-generated CNC mask of a single channel or multiple channels of meteorological satellite imagery. These CNC analyses are binary cloud maps generated with special software that identifies clouds in a given spectral band by making all pixels cloudy that have values that exceed a user-defined threshold. Similarly, all pixels less than the threshold value remain cloud-free. The image typically needs to be segmented into sub-regions to accurately delineate cloudy and cloud-free regions, especially for scenes of large geographic regions or highly heterogeneous conditions, since some cloud-free land surfaces may have pixel values larger than clouds in another part of the scene. In addition, CNC analyses from multiple bands may be merged into a single, total CNC analysis. This process is shown in Figure 3.

Clouds and snow are seen in Panel (a) of Figure 3 which contains the 0.9 μm band and Panel (b) that shows the 12.0 μm band of AVHRR imagery. The scene is centered near San Francisco, CA with the Sierra Mountains seen in the lower right corner extending toward the middle of the image. The California coast and Pacific Ocean are most visible in Panel (a) although much of the coast is obscured by clouds. Lake Tahoe is clearly visible in Panel (a) at the north end of the Sierra Mountain range just right of the image center.

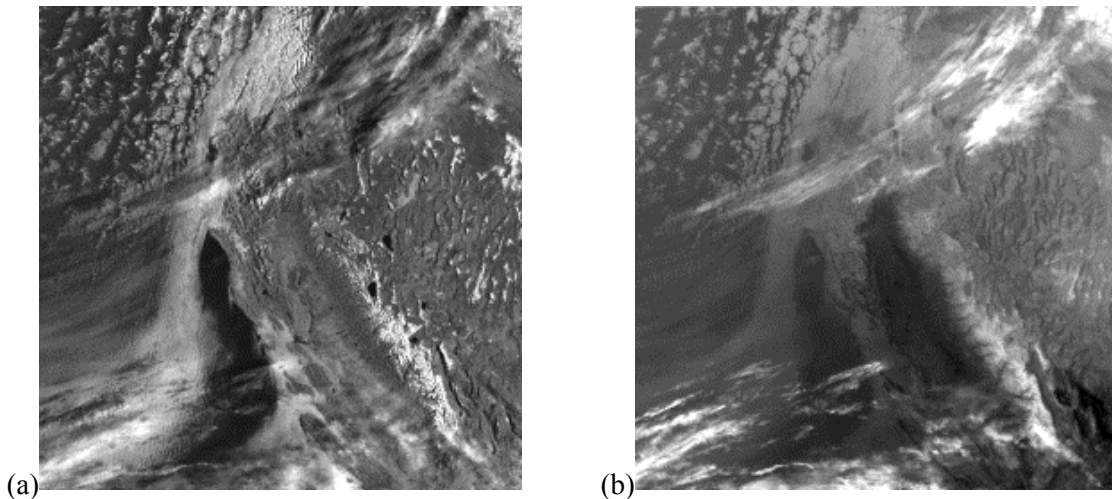


Figure 3. Clouds and snow are bright in AVHRR imagery Channel 2 (0.9 μm) at Panel (a) and Channel 5 (12.0 μm) at Panel (b) of a NOAA-12 scene collected on March 19, 1996 (Hutchison et al, 1997).

Using the principals discussed in Section 3.1 allows the contrast to be maximized between the clouds in some parts of the scene and the cloud-free backgrounds. For example, the maximum contrast occurs between clouds and both vegetated and ocean surfaces in the 0.6 μm AVHRR band (Channel 1). Using this band alone allows the human analyst to create a highly accurate manually-generated CNC analysis over these surfaces, as shown in Figure 4.

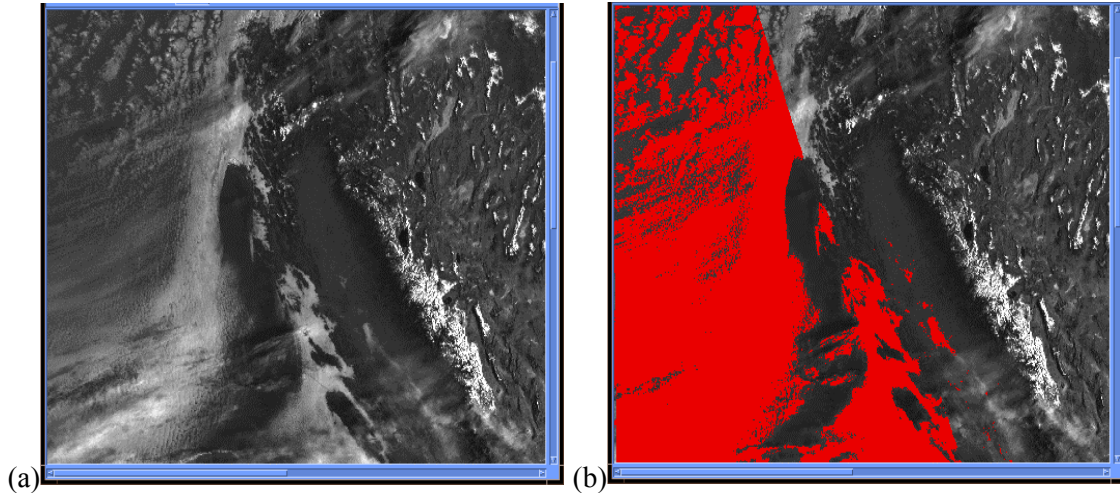


Figure 4. Clouds seen in the 0.6 μm band (Channel 1) of the AVHRR imagery in Panel (a) are contained the manually-generated cloud analysis, are shown as red, in Panel (b).

Prior to performing a manual analysis of the right half of the scene, the contrast between snow and clouds must be enhanced in order to differentiate between these features, since they appear very similar in the AVHRR Channels 1, 2, and 5 as shown in Figures 3 and 4. Prior to the launch of NOAA-15, which contains the 1.6 μm band, a methodology was developed to enhance the spectral signature of cirrus clouds and suppress the signature of snow in the daytime 3.7 μm band of AVHRR (Channel 3). The procedure was applied to this scene to enhance the snow/cloud contrast. Results are shown in Panel (a) of Figure 5 along with the manually generated cloud analyses of this portion of the scene in Panel (b).

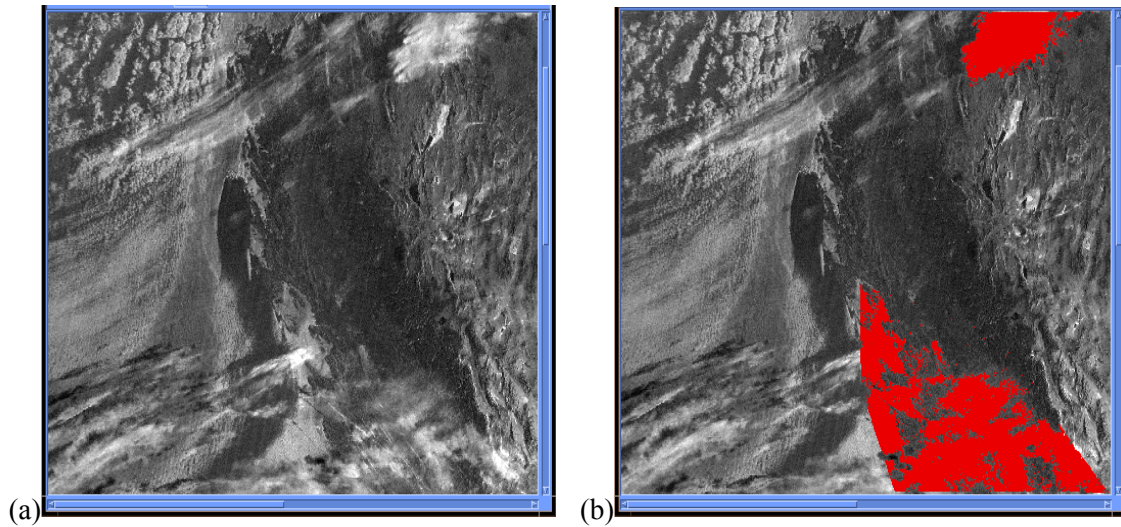


Figure 5. Snow now appears black in Panel (a) containing the albedo component of the $3.7\ \mu\text{m}$ band (Channel 3) of the AVHRR imagery while Panel (b) contains the manually-generated cloud analysis made using this image.

The total CNC analysis for the scene is constructed from the composite of the CNC analyses shown in Figures 4 and 5. These results are shown as green in Figure 6. This complete manually-generated CNC analyses of all clouds in the scene is useful for determining quantitatively the performance of automated cloud detection algorithms that might be generated with data from this particular scene.

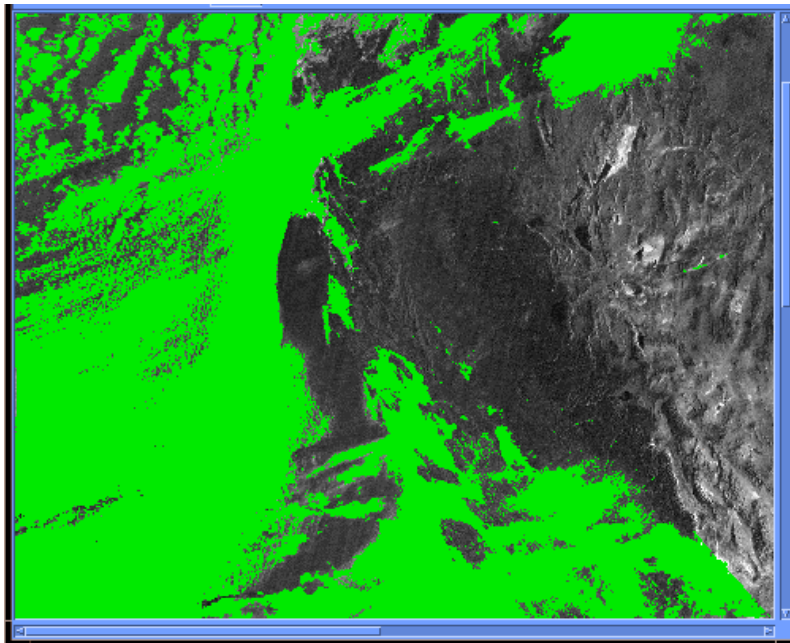


Figure 6. Example of a total CNC analysis created by merging CNC analyses from individual spectral bands shown in Figures 4 and 5 into a single CNC analysis.

3.2.2 Cloud Truth in Synthetic Scenes for Sensor Simulations

Manually-generated CNC masks can also be created from simulated VIIRS imagery to optimize sensor design parameters and their effects upon image quality. The process is shown in Figures 7 and 8. This procedure starts by defining a synthetic background, as shown in Panel (a) of Figure 7. This particular synthetic background contains a large region of ocean surface (darkest) selected to represent the Earth's since it is 75% water. Next, surface regions composed of sand (next darkest), snow (large area of light), and vegetated land (small island surrounded by ocean) are added in an attempt to simulate global conditions. Synthetic clouds are the final addition to the scene and are shown as white in Panel (b). In this particular case, large regions of water clouds are added to the simulation. Atmospheric models are then added to the scene to create the complete synthetic scene before the simulated VIIRS image is generated. The process of simulating VIIRS imagery was completed with PACEOS, which is an acronym for Performance and Analysis Capabilities for Earth Observing Systems. PACEOS has been partially described in the literature (Hutchison et al., 1999).



Figure 7. Synthetic background shown in Panel (a) are used with cloud mask, shown in Panel (b) to generate synthetic VIIRS imagery.

Any combination of CNC masks and synthetic backgrounds can be used to simulate VIIRS synthetic scenes. A cirrus cloud is shown in Figure 8. Once the simulated VIIRS imagery is generated (left panel in Figure 8), a manually-generated cloud mask can be created from this synthetic imagery as discussed above. The manually-generated cloud mask of the simulated VIIRS 12.0 μm imagery is shown in the top panel of Figure 8. Comparisons between the manually-generated cloud mask and the “truth” cloud mask used as input into the simulation, seen in the bottom panel of Figure 8, allow the performance of the manually-generated cloud mask to be quantified and the impact of sensor designs on image quality to be quantified. Differences between these two CNC analyses, shown in the right panel of Figure 8, are highly useful to identify problems and recommend solution to the sensor design.

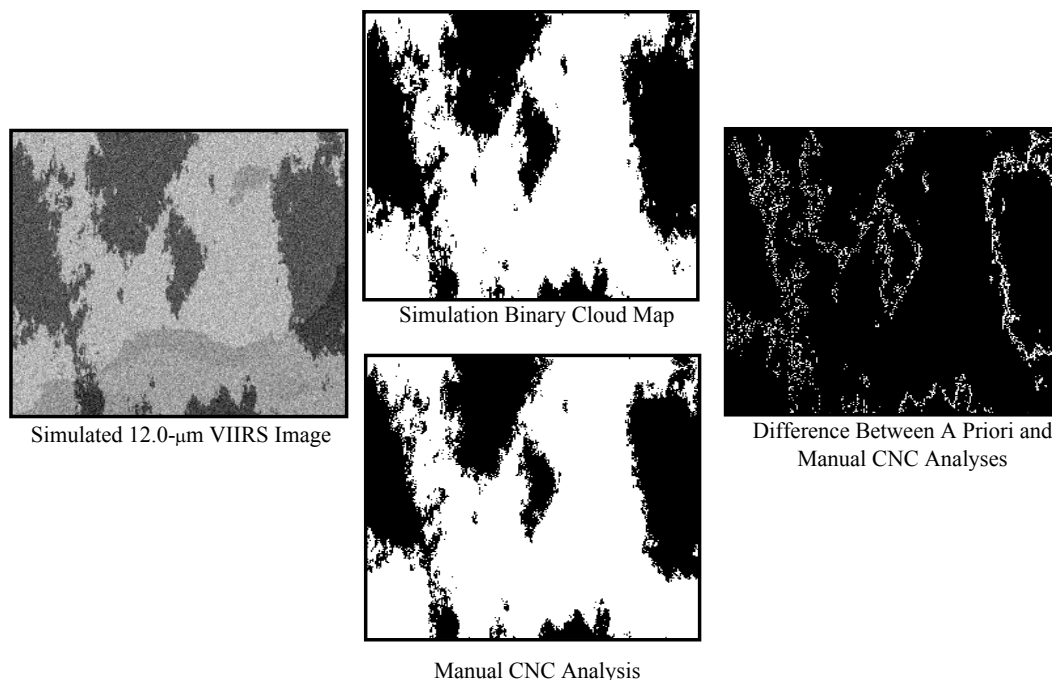


Figure 8. Synthetic 12.0 μm VIIRS image, manual and synthetic cloud masks, and difference fields show locations of inaccuracies in manually-generated cloud data product.

The pixel-level CNC masks, both truth and manually generated, can be summarized to any analysis resolution, e.g. for NPOESS this analysis size is referred to as the horizontal cell size (HCS) as shown in Table 4. Results of measurement uncertainty for the manually-generated CNC mask, compared to the ground truth CNC mask, are shown in Table 6 as a function of HCS. The results show that image quality produced by this particular VIIRS sensor model allowed the NPOESS Imagery EDR Threshold requirements (3x3 pixels in HCS shown in “green”) and Objective requirements (2x2 pixels in HCS shown in “blue”) for manually-generated cloud data products (measurement uncertainty not to exceed 0.1 as shown in Table 4) to be satisfied. It is clear from Table 6 that measurement uncertainty improves as HCS increases since errors in binary fields are either completely accurate or completely inaccurate.

Table 6. Comparisons of manually-generated cloud mask and simulation binary cloud mask for synthetic VIIRS imagery shown in Figure 8.

HCS	NUMBER OF HCS PIXELS IN SIMULATONS			BI-MODAL	UNCERTAINTY
(2 x 2 pixels)	Total	Clear	Overcast	(Percent)	(Fraction)
Truth	16,129	10,363	4677	93.25	n/a
Analysis	16,129	10,124	4969	93.58	0.099
(3 x 3 pixels)					
Truth	7140	4417	1890	88.33	n/a
Analysis	7140	4364	2010	89.27	0.078
(4 x 4 pixels)					
Truth	3969	2389	967	84.56	n/a
Analysis	3969	2373	1049	86.22	0.069
(8 x 8 pixels)					
Truth	961	528	170	72.63	n/a
Analysis	961	529	194	75.23	0.050
(25 x 25 pixels)					
Truth	100	40	3	43.00	n/a
Analysis	100	40	6	46.00	0.032

In summary, pixel-by-pixel comparisons between the “truth” and “manually-generated” CNC analyses are used to quantitatively determined conformance of the VIIRS Imagery and sensor model with NPOESS Threshold and Objective requirements. The preferred VIIRS sensor model and required number of VIIRS Imagery bands incorporates the most cost-effective sensor model that provides the human analyst with the capability of constructing manually-generated cloud analyses that satisfy NPOESS requirements. While the process of making manually-generated cloud data products is straightforward and simplistic, it is emphasized that sufficient contrast must exist between the cloud fields and surrounding backgrounds to allow these products to be created. Therefore, attention now turns to the methodology used to select both the VIIRS Imagery bands and the sensor model for each band in order to ensure sufficient contrast is present in global imagery to differentiate between clouds and a variety of backgrounds.

3.3 SENSOR BANDPASS SELECTION PROCESS

3.3.1. Basic Concepts of Satellite Radiometry and Instrument Design

The sensor design process requires extensive trade studies to optimize the VIIRS system parameters needed to meet NPOESS system requirements while maintaining financial responsibility. For example, a hyperspectral sensor can easily be designed that collects hundreds or even thousands of channels of data; however, major flaws of this design might include the expenses incurred to store the data on the spacecraft, communication downlinks to transmit the data from the satellite to the satellite readout facility, and computer resources necessary to prepare and fully utilize these data in an operational environment. Therefore, the Raytheon VIIRS design philosophy was to minimize the number of imagery bands required to meet NPOESS Imagery EDR requirements, discussed in Section 2.3, and to make all remaining VIIRS channels “Moderate Resolution Bands” as necessary to satisfy the remaining EDR requirements shown in Section 2.2. Key differences between imagery and moderate resolution bands are spatial resolution, as noted in Section 2.4, and band sensitivity. The effect of spatial resolution is straightforward in that the higher the spatial resolution, the larger the data volume and higher the communication costs necessary to transmit and process the data sets. The impact of band sensitivity on system cost may not be so straightforward, so it is discussed in some detail.

The sensitivity of radiometers depends on the ratio of their internally generated signal to that produced by incoming radiation (Stewart, 1985). The power available to the instrument is given by:

$$\Phi_{IN} = A \, d\Omega \, d\lambda \, L(\lambda) \quad (7)$$

where A is the aperture of the instrument, $d\Omega$ is the angular extent of the area viewed by the instrument, $d\lambda$ is the bandwidth, and $L(\lambda)$ is the spectral radiance of the area viewed. The power is usually focused on a detector that converts radiant power into electrical power which is then amplified and either recorded or transmitted to the ground. The output of the detector Φ_{out} is the sum of the incoming signal Φ_{IN} plus the noise, $\Delta\Phi$, generated within the transducer and is represented as:

$$\Phi_{OUT} = A \, d\Omega \, d\lambda \, L(\lambda) + \Delta\Phi \quad (8)$$

The signal-to-noise ratio, SNR or S_n , of an instrument or an individual band in a multispectral sensor is a common measure of performance for bands operating in the solar spectrum region (e.g. 0 - 5 μm). For example, each MODIS channel has a different SNR ranging between 57 for Band 18 (0.931-0.941 μm) and 1087 for Band 14 (0.673-0.683 μm). SNR is given by:

$$S_n = \Phi_{IN} / \Delta\Phi \sim [A \, d\Omega \, d\lambda \, L(\lambda)] / \Delta\Phi \quad (9)$$

Sensor designers seek to maximize S_n in a cost effective manner, which may only be done in a couple of ways. First, S_n may be enlarged by increasing: the size of the aperture (A); the field of view ($d\Omega$); and/or the bandwidth ($d\lambda$). Secondly, it is possible to increase S_n by reducing sensor or individual channel noise, $\Delta\Phi$, which is done with improved detector performance.

By convention, instrument noise is inserted into the Planck equation and converted to an apparent change in temperature, ΔT , or Noise Equivalent ΔT (NE ΔT) for bands operating in the thermal infrared spectrum region, e.g. 5-100 μm . In this case, the optimal sensor design minimizes NE ΔT in a cost effective manner. For MODIS, values of NE ΔT range from 0.05 K for Band 20 (3.660-3.840 μm) to 2.00 K for Band 21 (3.929 – 3,989 μm). In general, an increase in the channel bandpass, $d\lambda$, is a cost-effective way to lower the NE ΔT of a given channel and improve EDR retrieval accuracy (Hutchison, et. al., 1999).

Another option to maximize the function, S_n , is to observe the area multiple times, N , with the same instrument, assuming $L(\lambda)$ does not change between observations, as is done with the along-track scanning radiometer (ATSR) flown on the ERS satellite series (Za’vody, 1995). The average of these observations converge toward Φ_{IN} as N increases. If the noise in different observations is not correlated, then on average:

$$S_n = (N)^{0.5} [A \, d\Omega \, d\lambda \, L(\lambda)] / \Delta\Phi \quad (10)$$

Thus, the optimum NPOESS VIIRS sensor design becomes a trade study in 3-dimensional space: system capabilities, program costs, and user EDR requirements. For example, the aperture (A) can also be increased to maximize S_n at the expense of making the instrument larger and heavier but cannot exceed weight allocations provided for VIIRS on the NPOESS satellite. The field of view can also be increased; however, spatial resolution must be balanced against the increase in $d\Omega$ and horizontal cell size, which relates to field-of-view, as defined by the NPOESS program. Cooling VIIRS sensor detectors to lower temperatures can be used to decrease the NE ΔT but must be limited to NPOESS satellite power allocations. Finally, each channel band-center and bandwidth is constrained by (1) solar/thermal energy availability, (2) atmospheric transmission, and (3) phenomenology associated with the retrieval of a given EDR product. For example, shown in Figure 9 is the spectral irradiance distribution for solar illumination at the top of the Earth’s atmosphere and at sea level. Darkened areas represent regions of strong atmospheric absorption while the scale shows gaseous species absorbing the solar energy. If only solar irradiance was important, much higher values of S_n could be achieved by placing a band-center near 0.5 μm rather than at 2.5 μm . However, there are phenomenological issues in addition to available energy that must be considered before making bandpass selections, including atmospheric transmission and the interaction of electromagnetic radiation with a variety of surface features and cloud ice and water particles.

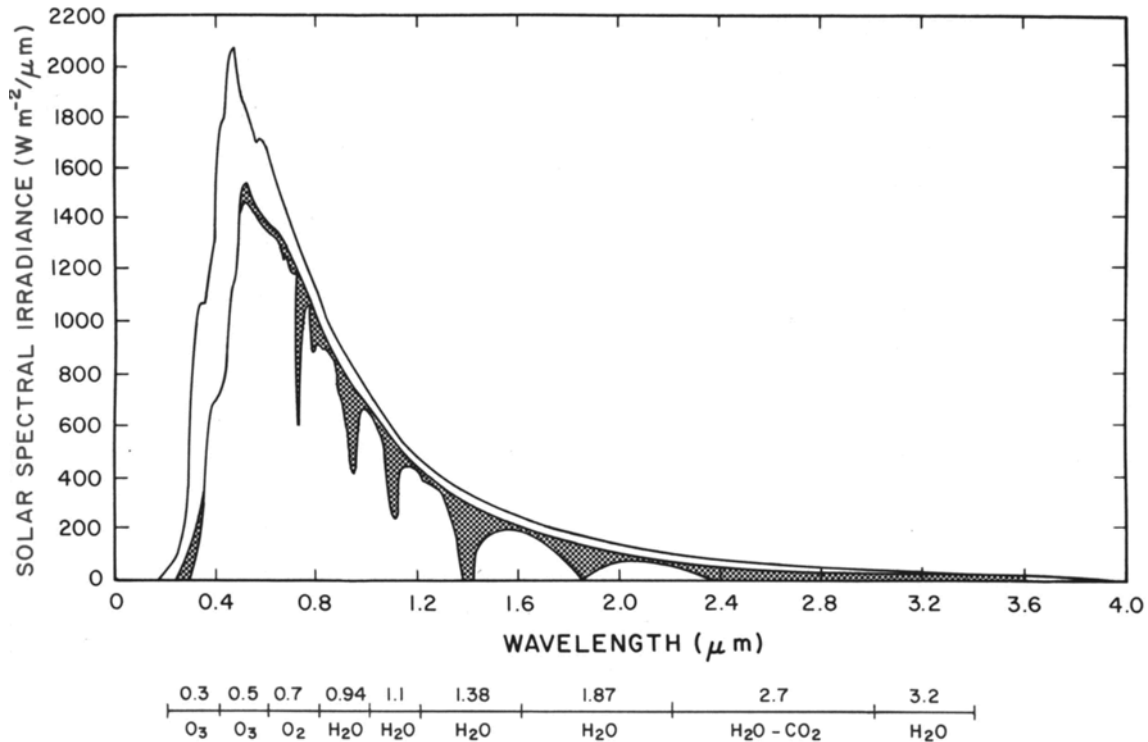


Figure 9. Solar spectral irradiance distribution for top of the atmosphere (TOA) and sea level along with primary atmospheric absorption bands and species. (Figure 2.6 from Liou, 1980).

The final set of design issues that must be considered involves interactions between the sensor hardware and the “observed” radiation impinging upon the optics of the sensor. Among these sensor hardware issues are efficiency of detector materials and size of focal planes to name a few. An overview of the VIIRS sensor hardware is provided in Chapter 4.

3.3.2 Phenomenology of Spectral Signatures

Attention now turns to an examination of the phenomenology that must be evaluated in order to select VIIRS bandpasses needed to perform manually-generated cloud analyses within the performance requirements of the NPOESS system. This process leads directly to the formulation of VIIRS bandpass sets for both Imagery and Imagery Assist bands.

In Section 3.1, it was shown that the capability to manually detect a cloud in infrared imagery is enhanced under the following conditions:

- significant temperature contrasts exist between the cloud and the surrounding background which have very similar emissivities in one infrared channel,
- a cloud and its surrounding background may have the same temperature but significantly different emissivities in one spectral band, or
- atmospheric transmissivity is markedly different in one band which masks the signature of the cloud from the background.

Furthermore, it was concluded that the capability to manually detect a cloud in visible and near-infrared imagery and distinguish it from the surrounding background is enhanced by using one or more spectral bands where differences in the cloud and surface reflectivities are significant by:

- exploiting strong contrasts between the cloud reflectivity and its surrounding background,
- viewing features in one band in which atmospheric transmissivity is markedly different such that the surface feature is masked by the atmosphere but the cloud is not.

A powerful method to differentiate between clouds and their surrounding cloud-free backgrounds exploits two or more channels simultaneously to examine changes in the spectral signature of either the cloud or its background. If only two spectral bands are used, this technique is commonly referred to as “bi-spectral” imagery analysis. Bi-spectral methods that use arithmetic manipulation, e.g. addition, subtraction, division etc., of multiple digital images have proven very powerful for the manual and automated detection of clouds as well as identification of various surface backgrounds. When different channels are assigned to guns of a color monitor, differences in spectral signatures are evident by their colors. More on bi-spectral and color composite methods is provided later in Chapter 6.

Shown in Figures 10 through 13 are the phenomenological data needed to begin the VIIRS bandpass selection process. These figures contain spectral signatures of cloud particles and various backgrounds along with solar illumination at the top of the atmosphere and atmospheric transmission for a mid-latitude summer profile, as described by Anderson et al. (1986). Together, the figures cover the 0.3 - 12.0 μm region of the solar and terrestrial spectral. All data were generated with the MODTRAN radiative transfer model (Berk, 1989). The key to the tables is as follows: indices of refraction for water and ice are shown by solid and dashed turquoise lines respectively, reflectivities of cloud-free surfaces are: (a) green for vegetated land, (b) dark blue for ocean, (c) snow is white, and (d) bare soil is yellow. Top of the atmosphere solar illumination is shown in gold while atmospheric transmission is the highly irregular black line that depict absorption by atmospheric gases and scattering by aerosols. VIIRS bandpass selections are shown as blue that extend to the top of each table.

It is seen in Figures 10-13 that the VIIRS Imagery channels are generally located in regions where atmosphere attenuation is relatively small and does not change significantly with height. These regions are known as “atmospheric windows.” There are several atmospheric windows in the region between 0.3 and 12.0 μm . The most commonly known windows are the 0.5 - 0.9 μm , 3-5 μm , and 8-12 μm windows. Others include two near-IR (1.5 - 1.7 and 2.1 - 2.3 μm) windows. While the 3-5 μm range is typically referred to as an atmospheric window, absorption spectra in Figure 12 clearly show the window is most clean (highest atmospheric transmission) between 3.5 - 4.0 μm . Strong absorption occurs near 4.2 - 4.5 μm due primarily to gaseous carbon dioxide and water vapor. In fact, almost no energy emitted in this wavelength interval by a cloud-free

surface on the Earth would arrive at the VIIRS sensor. Therefore, imagers necessarily operate in spectral regions where the atmosphere absorption tends to be minimal.

The International Geosphere-Biosphere Program (IGBP) recognizes 17 categories of land cover (VIIRS SRD, 2000). Figures 10 - 13 show the spectral reflectivities for the key land surface classes found on the Earth, i.e. ocean, vegetated land, bare soil, and snow.

To illustrate the value of these data, turn to Figure 10 and note the differences in spectral response for snow, vegetated land, and bare soil in the 0.5 - 0.9 μm region. The reflectivity of vegetated land is less than 10% at 0.5 μm , increases slightly to just over 10% at 0.55 μm and reaches a minimum of $\sim 0.5\%$ between 0.65 and 0.7 μm . On the other hand, the reflectivity of bare soil has its minimum at 0.4 μm and increases steadily to nearly 40% at 1.0 μm , while snow has a much higher reflectivity across the entire wavelength interval, i.e. over 90% from 0.3 - 0.8 μm , tailing to $\sim 73\%$ at 1.0 μm . At the same time, the index of refraction for water and ice clouds are initially small and increase constantly across the region. These curves suggest the following:

- Cloud-free, snow-covered surfaces can be differentiated from cloud-free vegetated surfaces and bare soil surfaces by comparing responses in two bands centered near 0.65 microns and 0.86 microns. This is possible since the reflectivity of snow decreases in these two bands while the reflectivity of vegetated land increases as does the reflectivity of bare soil. One might assume that absolute albedo alone would be adequate to make these distinctions; however, that is not the case. Problems result from the need to know the angular distribution of energy of each surface type. Typically, surfaces are assumed to scatter energy in a uniform shape, i.e. as isotropic scatterers. But this is not the case in reality. By examining the ratio between two bands, the absolute albedo is not important.
- A more powerful method to identify snow can be seen by examining its spectral signature in the 1.6 μm region in contrast to its value in the 0.65 μm region. The reflectivity of snow has a minimum near 1.5 μm ; unfortunately, atmospheric transmission is also a minimum at 1.4 μm but begins to increase rapidly near 1.5 microns. At wavelengths slightly shorter than 1.6 μm , the reflectivity of snow is very low while the atmospheric transmission is very high, e.g. over 90 percent. Therefore, the ratio of signatures in the 1.6 and 0.65 μm bands is positive proof of the presence of snow since this ratio approaches zero for snow, but is much greater than unity for vegetated and bare soils. Thus, the power of bi-spectral methods is demonstrated for positive feature identification. These differences in the spectral signatures of clouds and various backgrounds will be examined in Chapters 5 and fully exploited using color composites in Chapter 6.

3.3.3 VIIRS Imagery Bandpass Selection for Manual Cloud Detection

Based upon the preceding logic, a flowdown of sensing requirements was completed to identify the minimum number of Imagery bands needed to satisfy NPOESS threshold requirements for the manually-generated cloud data product EDR. Results of this analysis are shown in Table 7 for the Imagery bands centered at 0.64, 3.7 and 12.0 μm . Two additional VIIRS channels are included as Imagery bands due to requirements established by other EDRs. They are the explicit requirement for nighttime visible imagery band and the derived requirement for a 1.6 μm band needed for the snow-cover EDR. This flowdown was completed using principles outlined in Section 3.2.2 to address the NPOESS requirements shown in Tables 4 and 5.

Table 7. VIIRS Imagery Bands Needed to Satisfy Each NPOESS VIIRS Requirement for Manually-Generated Cloud Cover and Cloud Type EDRs (NPOESS VIIRS SRD, 2000).

NPOESS Attribute	Threshold Requirements	VIIRS Objectives	Comments
Cloud Detection (Measurement Uncertainty)	0.1 for HCS 3x3	0.1 HCS 2x2	Satisfies Objectives for worst case scenario using 3 Imagery channels with bandpasses centered near 0.64, 3.7, and 12.0 microns)
Cloud Typing (Probability of being Correct)	85% for Clear, Ci, St, Cu,	90% for all 17 cloud types	Requires spectral difference in 3.7 and 12.0 micron bands to distinguish between nighttime stratus and cirrus
VIIRS Capability	To Satisfy Thresholds	Toward Meeting Objective	Explanation
Clear from cloudy or obscured	0.088 detection (HCS 3x3) for cirrus as a worst case	0.099 (HCS 2x2) for cirrus as a worst case	objective satisfied for worst case scenario using 3 Imagery channels with bandpasses centered near 0.64, 3.7, and 12.0 microns)
Cirrus	100% typing compared to water clouds		objective satisfied using 12.0 and 3.7 micron band temperature difference to distinguish cirrus from stratus
Stratus	100% typing compared to cirrus clouds		3.7 micron needed both to detect nighttime stratus and distinguish it from cirrus
Cumulus	100% typing compared to other clouds based on shape		use 0.64 band over most surface along with 3.7 micron for detection over sand (i.e. thermal component) and 3.7 albedo over snow-covered regions along with texture
Obscured/Not Cloudy	0.1 detection accuracy for optical depth \geq 0.07 in 0.64 micron region		dark pixel method using 12.0 micron channel for thresholds, additional use of 0.4 micron channel for detection over bright (desert) backgrounds

The VIIRS sensor design includes a total of 22 spectral bands needed to satisfy all EDR requirements shown in Section 2.2. This design includes five imagery resolution bands, shown as I-bands in Table 8, and 17 “Moderate Resolution” bands designated as “M” bands. As previously noted, moderate resolution bands have a more coarse spatial resolution but a much higher signal-to-noise ratio than imagery resolution bands. In several cases, both imagery and moderate resolution bands were needed to satisfy all VIIRS requirements, e.g. 0.865, 1.6, and 3.7 μm channels. Both imagery and moderate resolution bands are available for use in the creation of the manually-generated cloud

data product EDRs. A detailed discussion of each VIIRS band is provided in Chapter 5 along with sample imagery to emphasize the features that can be positively identified with each band. In Chapter 6, color composites are shown of the imagery resolution channels. Also in Chapter 6 the value of using Imagery and Imagery-Assist bands together is demonstrated using color composites to quickly detect and type clouds, which is necessary to support the QC of automated cloud analyses or create manually-generated cloud data product EDRs.

Table 8. VIIRS Imagery and Imagery Assist Band Selected to Satisfy NPOESS Requirements.

Channel Number	VIIRS Designator	Central Wavelength λ_c (microns)	Bandwidth $\Delta\lambda$ (microns)	HSI @ nadir (km)	HSI @ 55.8° (km)
1	DNB	0.7	0.4	0.742	0.742
2	M1	0.412	0.02	0.742	1.6
3	M2	0.445	0.018	0.742	1.6
4	M3	0.488	0.020	0.742	1.6
5	M4	0.555	0.020	0.742	1.6
6	I1	0.640	0.080	0.371	0.8
7	M5	0.672	0.020	0.742	1.6
8	M6	0.746	0.015	0.742	1.6
9	I2	0.865	0.039	0.371	0.8
10	M7	0.865	0.039	0.742	1.6
11	M8	1.240	0.020	0.742	1.6
12	M9	1.378	0.015	0.742	1.6
13	I3	1.610	0.060	0.371	0.8
14	M10	1.610	0.060	0.742	1.6
15	M11	2.250	0.050	0.742	1.6
16	I4	3.740	0.380	0.371	0.8
17	M12	3.700	0.180	0.742	1.6
18	M13	4.050	0.155	0.742	1.6
19	M14	8.550	0.300	0.742	1.6
20	M15	10.763	1.000	0.742	1.6
21	I5	11.450	1.900	0.371	0.8
22	M16	12.013	0.950	0.742	1.6

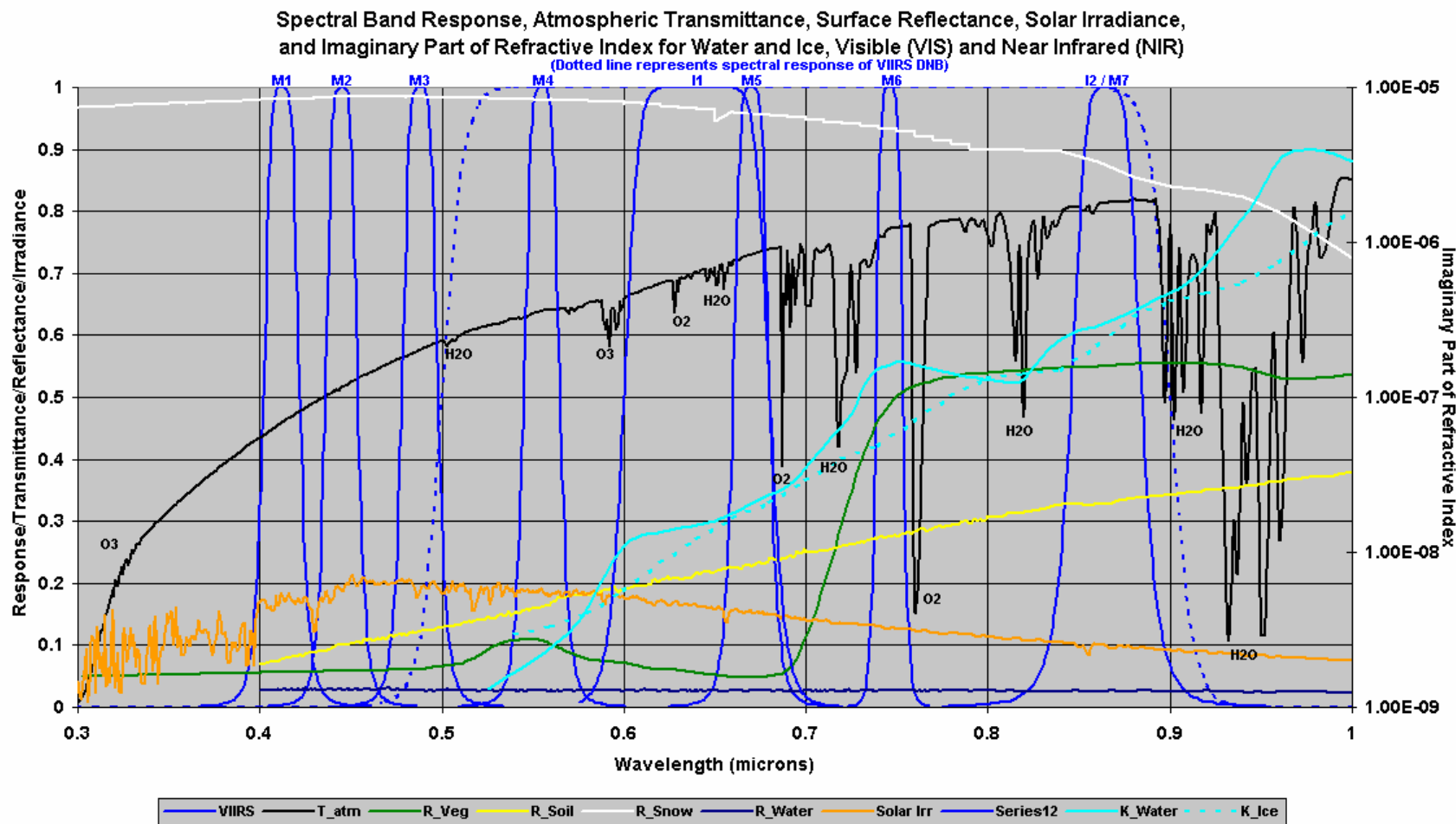


Figure 10. Spectral signatures of cloud particles and surface backgrounds in 0.3 - 1.0 micron range. (Key: Reflectivities: vegetated land = green, ocean = dark blue, snow = white, sand = yellow., solar illumination = gold and atmospheric transmission = black. VIIRS bands blue.)

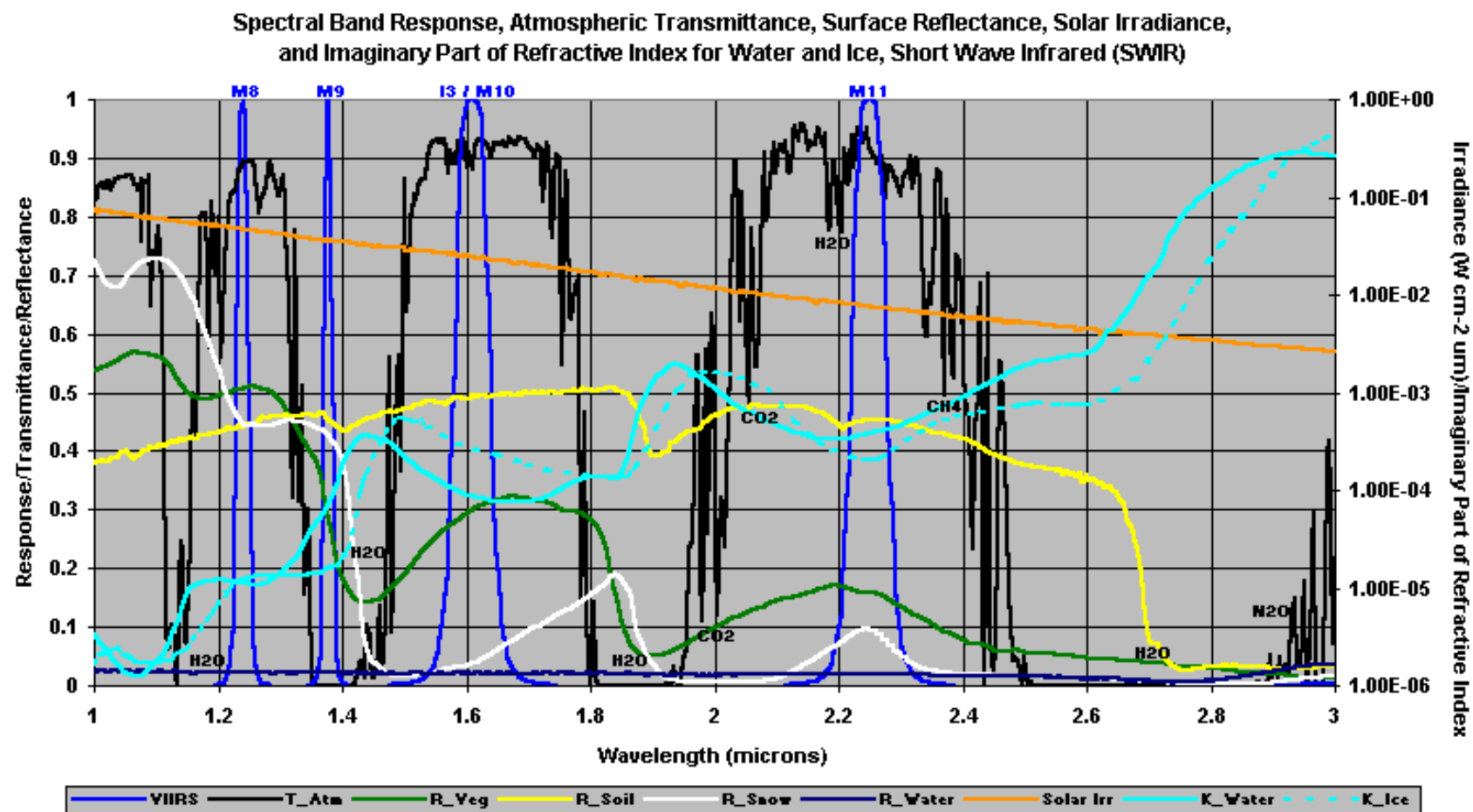


Figure 11. Spectral signatures of cloud particles and surface backgrounds in 1.0 - 3.0 micron range. (Key: Reflectivities of, vegetated land = green, ocean = dark blue, snow = white, sand = yellow. Solar illumination = gold and atmospheric transmission = black. VIIRS bands are shown in lighter blue.)

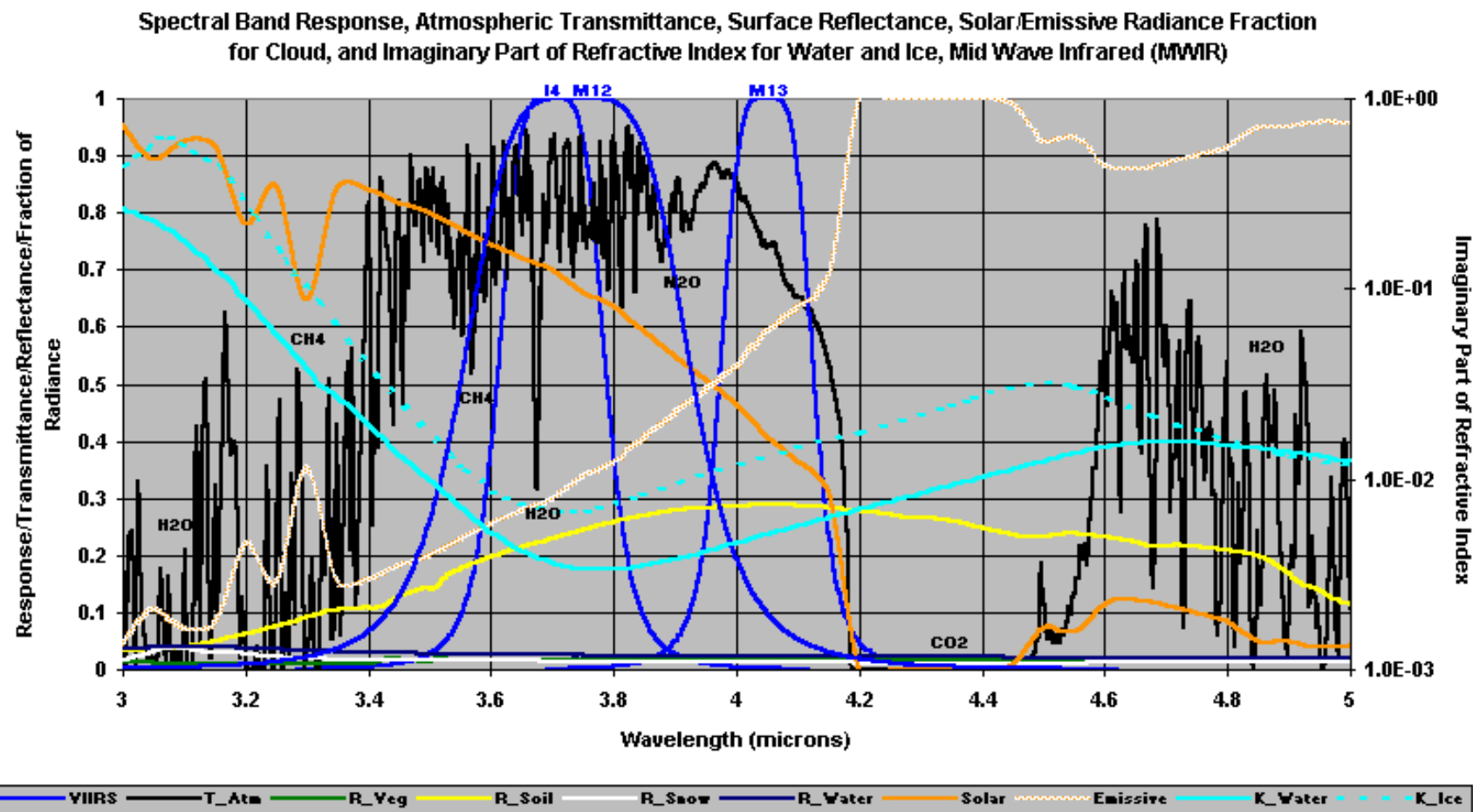


Figure 12. Spectral signatures of cloud particles and surface backgrounds in 3.0 - 5.0 micron range. (Key: Reflectivities of, vegetated land = green, ocean = dark blue, snow = white, sand = yellow. Solar illumination = gold and atmospheric transmission = black. VIIRS bands are shown in lighter blue.)

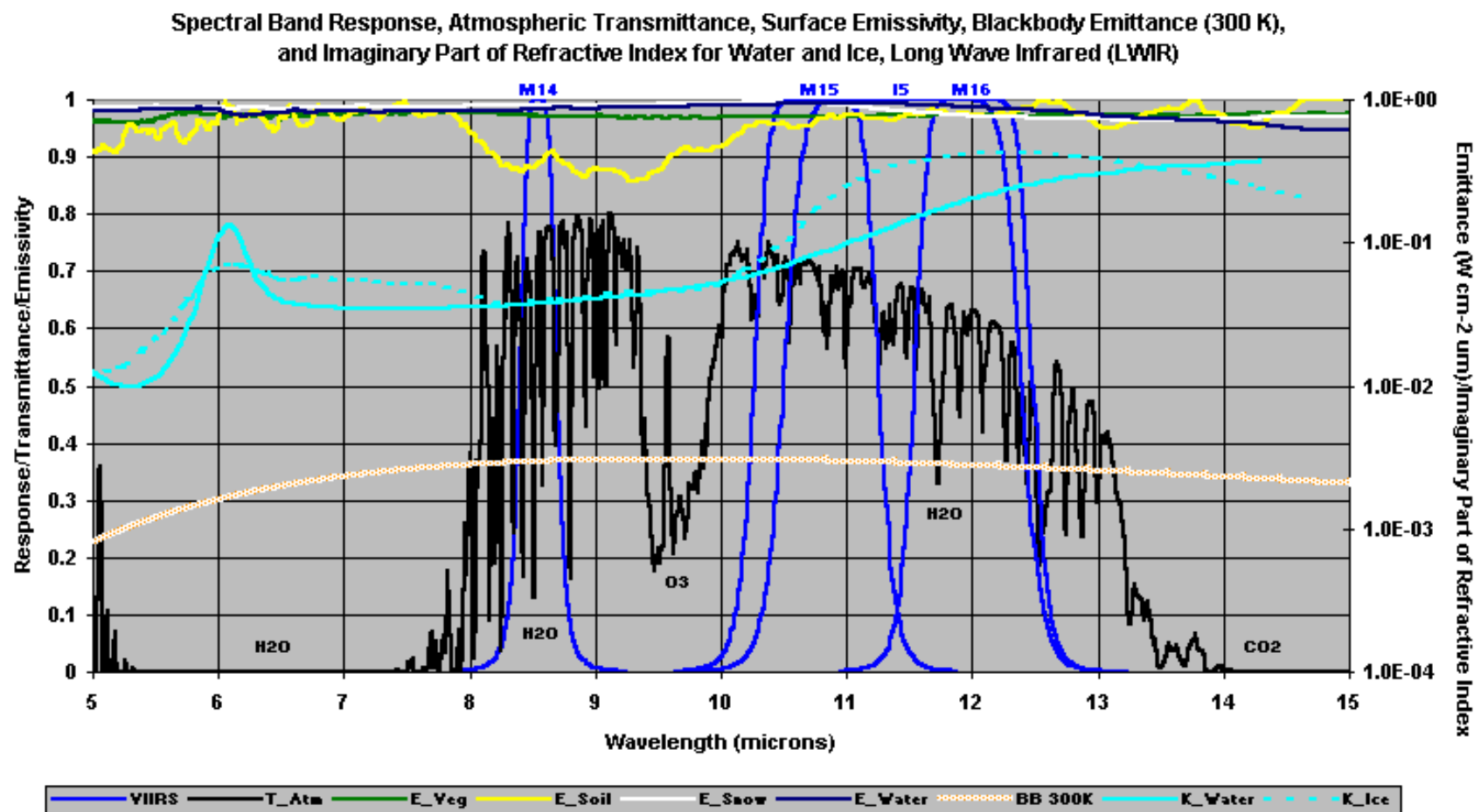


Figure 13. Spectral signatures of cloud particles and surface backgrounds in 5.0.- 15.0 micron range. (Key: Reflectivities of, vegetated land = green, ocean = dark blue, snow = white, sand = yellow. Solar illumination = gold and atmospheric transmission = black. VIIRS bands are shown in lighter blue.)

Chapter 4

VIIRS INSTRUMENT CHARACTERISTICS

The VIIRS instrument can be pictured as a convergence of three existing sensors, two of which have seen extensive operational use at this writing.

The Operational Linescan System (OLS) is the operational visible/infrared scanner for the Department of Defense (DoD). Its unique strengths are controlled growth in spatial resolution through rotation of the ground instantaneous field of view (GIFOV) and the existence of a low-level light sensor (LLS) capable of detecting visible radiation at night. OLS has primarily served as a data source for manual analysis of imagery. The Advanced Very High Resolution Radiometer (AVHRR) is the operational visible/infrared sensor flown on the National Oceanic and Atmospheric Administration (NOAA) Television Infrared Observation Satellite (TIROS-N) series of satellites (Planet, 1988). Its unique strengths are low operational and production cost and the presence of five spectral channels that can be used in a wide number of combinations to produce operational and research products. In December 1999, the National Aeronautics and Space Administration (NASA) launched the Earth Observing System (EOS) morning satellite, *Terra*, which includes the Moderate Resolution Imaging Spectroradiometer (MODIS). This sensor possesses an unprecedented array of thirty-two spectral bands at resolutions ranging from 250 m to 1 km at nadir, allowing for unparalleled accuracy in a wide range of satellite-based environmental measurements.

VIIRS will reside on a platform of the National Polar-orbiting Operational Environmental Satellite System (NPOESS) series of satellites. It is intended to be the product of a convergence between DoD, NOAA and NASA in the form of a single visible/infrared sensor capable of satisfying the needs of all three communities, as well as the research community beyond. As such, VIIRS will require three key attributes: high spatial resolution with controlled growth off nadir, minimal production and operational cost, and a large number of spectral bands to satisfy the requirements for generating accurate operational and scientific products.

The Explicit Imagery is obtained from the VIIRS EV_375M Sensor Data Record (SDR) and the VIIRS EV_DNB SDR. The SDRs are obtained from VIIRS Raw Data Records (RDRs) by an RDR to SDR process. The RDRs are obtained by a rotating telescope scanning mechanism that minimizes the effects of solar impingement and scattered light. Figure 14 illustrates the design concept for VIIRS, designed and built by Raytheon Santa Barbara Remote Sensing (SBRS). VIIRS is essentially a combination of SeaWiFS foreoptics and an all-reflective modification of MODIS/THEMIS aft-optics. Calibration is performed onboard using a solar diffuser for short wavelengths and a blackbody source and deep space view for thermal wavelengths. A solar diffuser stability monitor (SDSM) is also included to track the performance of the solar diffuser. The VIIRS scan will extend to 56 degrees on either side of nadir, providing a swath of 3000 km for the nominal satellite altitude of 833 km.

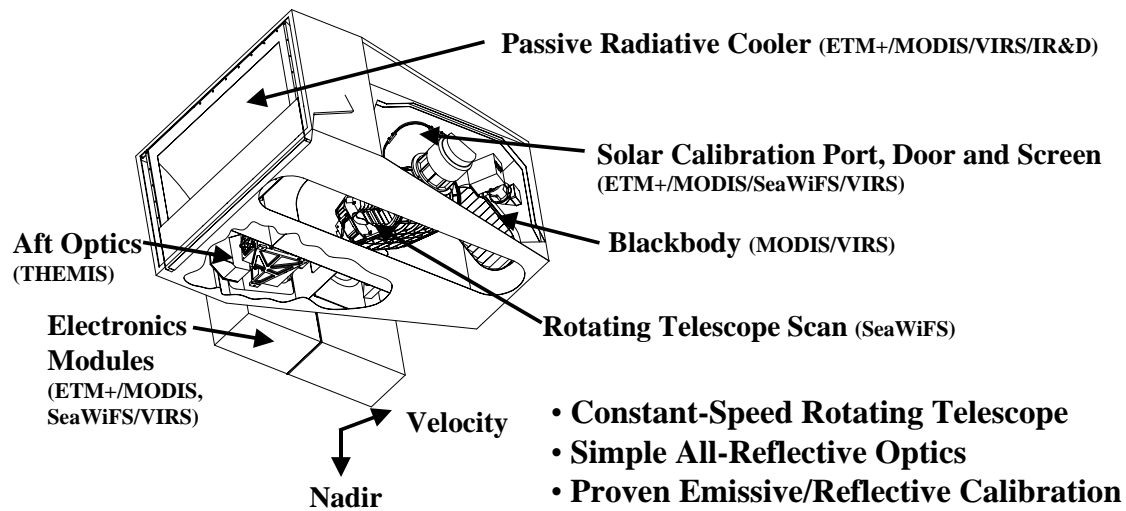


Figure 14. Summary of VIIRS design concepts and heritage.

The VIIRS SRD places explicit requirements on spatial resolution for the Imagery EDR. Specifically, the horizontal spatial resolution (HSR) of bands used to meet threshold Imagery EDR requirements must be no greater than 400 m at nadir and 800 m at the edge of the scan. This led to the development of a unique scanning approach which optimizes both spatial resolution and signal to noise ratio (SNR) across the scan. The concept is summarized in Figure 15 for the imagery (fine resolution) bands. The VIIRS detectors are rectangular, with the smaller dimension along the scan. At nadir, three detector footprints are aggregated to form a single VIIRS “pixel.” Moving along the scan away from nadir, the detector footprints become larger both along track and along scan, due to geometric effects and the curvature of the Earth. The effects are much larger along scan. At 31.59 degrees in scan angle, the aggregation scheme is changed from 3x1 to 2x1. A similar switch from 2x1 to 1x1 aggregation occurs at 44.68 degrees. The VIIRS scan consequently exhibits a pixel growth factor of only 2 both along track and along scan, compared with a growth factor of 6 along scan which would be realized without the use of the aggregation scheme. This scanning approach allows VIIRS to provide imagery at 800-m resolution or finer globally, with 375-m resolution at nadir. Additionally, due to the imagery requirements for VIIRS and the “sliver” detector design, MTF performance will be extremely sharp (0.5 at Nyquist).

Fine-Resolution Bands for Imagery

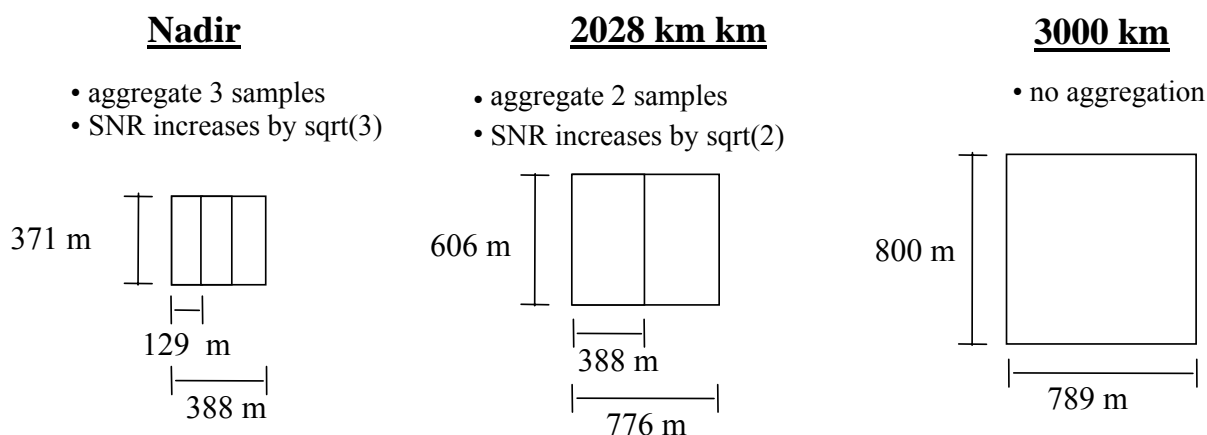


Figure 15. VIIRS detector footprint aggregation scheme for building Imagery “pixels”.

Figure 16, showing the Horizontal Sampling Interval (HSI) that results from the combination scan/aggregation scheme, illustrates the benefits of the aggregation scheme for spatial resolution.

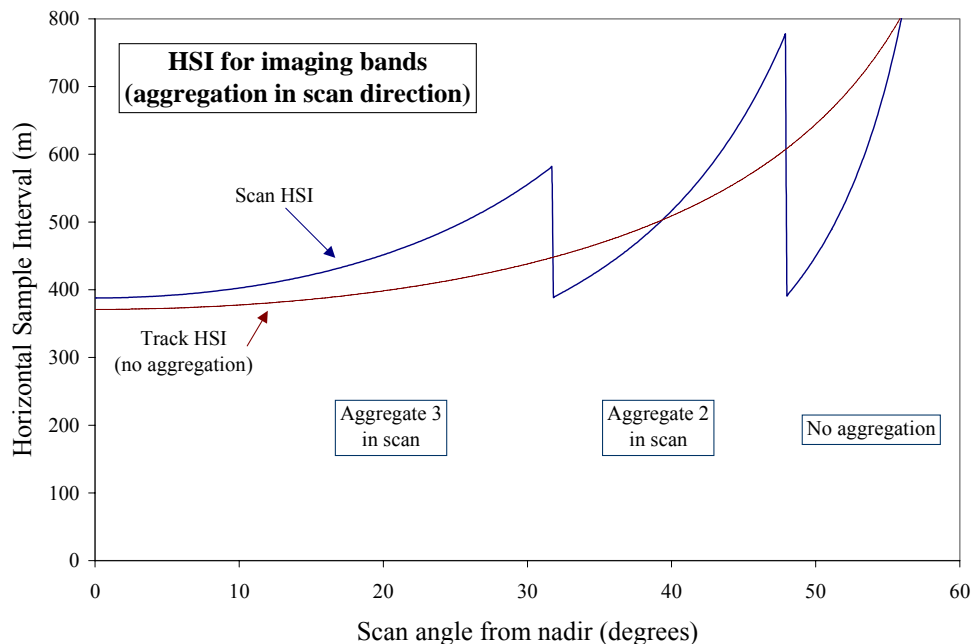


Figure 16. Horizontal Sampling Interval (HSI) for imagery bands (aggregation in scan direction).

The HRI of the Daytime Visible (DV), Long-Wave Infrared (LWIR) and Mid-Wave Infrared (MWIR) imagery will be the HSI. The Modulation Transfer Function (MTF) specification is 0.5 at the sampling Nyquist frequency, resulting in HSR equal to HSI. Therefore, the specification for HRI is equivalent to the imagery HSR specification.

Even though the aggregation scheme greatly reduces the growth in HSI across the scan, there is still a factor of 2 growth resulting in a residual “bow tie” effect. We achieve an additional reduction in the bow tie by deleting 4 of the 32 detectors from the output data stream for the middle (Aggregate 2) part of the scan and 8 of the 32 detectors for the edge (No aggregation) part of the scan. Figure 17 illustrates the resultant additional bow tie deletion.

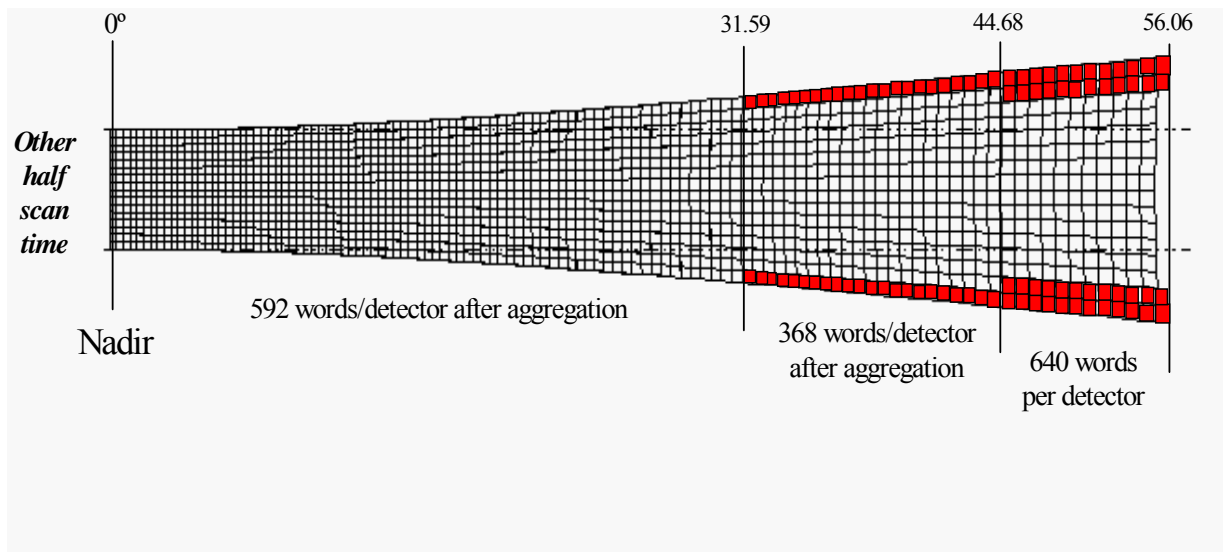


Figure 17. VIIRS aggregation and bow tie pixel reduction.

Chapter 5

PRINCIPALS IN IMAGE INTERPRETATION

5.1. INTRODUCTION

In this chapter, basic and more advanced concepts are discussed that deal with the manual interpretation of meteorological satellite data in general and MODIS/VIIRS imagery in particular. In Chapter 3, the surface energy from a cloud-free atmosphere arriving at the aperture of the satellite sensor was given in Equation II for terrestrial radiation and Equation IV for solar radiation. In Chapter 4, the path was described that takes TOA energy into the VIIRS sensor optics through the digitizer and downlinked to the ground processing segments where RDRs are converted into calibrated SDRs. In this section, information is provided on the energy sources observed by the VIIRS sensor and the implications of interpretation on each band.

Figure 18 shows the normalized emission spectra for three blackbodies emitting at 6000K, 770K, and 300K. These temperatures are typical of the sun's photosphere, a forest fire, and a global average of the Earth's surface respectively. The figure helps illustrate the characteristics of blackbody radiation (Chapter 1, Liou, 1980):

- (1) The wavelength of the maximum emission becomes smaller as the blackbody temperature becomes larger. *Knowledge of source emission spectra help users determine which MODIS/VIIRS bands provide the “best” information on phenomena under investigation.* The maximum emission at the Sun's photosphere is ~ 0.5 microns but is $\sim 10 \mu\text{m}$ for the Earth's surface. Forest fires typically burn at 700 K and have their maximum emission in the 3-5 μm region.
- (2) The shape of each blackbody radiation curve shown in Figure 18 is described by Planck's Law and can be calculated using Equation (11). Planck's Law relates blackbody energy of monochromatic intensity (B_λ) to the absolute temperature (T in degrees Kelvin) of the object and the wavelength (λ) of the emission, where c and K are the velocity of light and the Boltzmann constant respectively.

$$B_\lambda(T) = 2hc^2 / \{ \lambda^5 [\exp(hc/K\lambda T) - 1] \} \quad (11)$$

- (3) The total radiant energy (F) of a blackbody can be derived by integrating the Planck function $B_\lambda(T)$ over the entire wavelength domain. This energy is proportional to the 4th power of the absolute temperature according to the Stefan-Boltzmann Law where (σ) is the Stefan-Boltzmann constant.

$$F = \sigma T^4 \quad (12)$$

- (4) Finally, the wavelength of the maximum intensity (λ_m) for blackbody radiation is inversely proportional to the absolute temperature, according to Wien's Displacement Law where $a = 0.2897 \text{ cm degree}$.

$$\lambda_m = a / T \quad (13)$$

- Spectral signatures of features collected at wavelengths greater than about 5 microns are unchanged during daytime and nighttime conditions.
- Spectral bands that collect energy at wavelengths smaller than 3 microns receive an insignificant amount from the Earth in nighttime imagery, except for the Day-Night VIIRS visible (DNV) channel that has special amplifiers to detect lunar illuminated surfaces.
- The 3-5 micron region receives energy from both the sun and the Earth-atmosphere system. Therefore, signatures in this spectral range are complex and may change dramatically between daytime and nighttime conditions. Detailed information on this band is provided in Section 5.2.4.

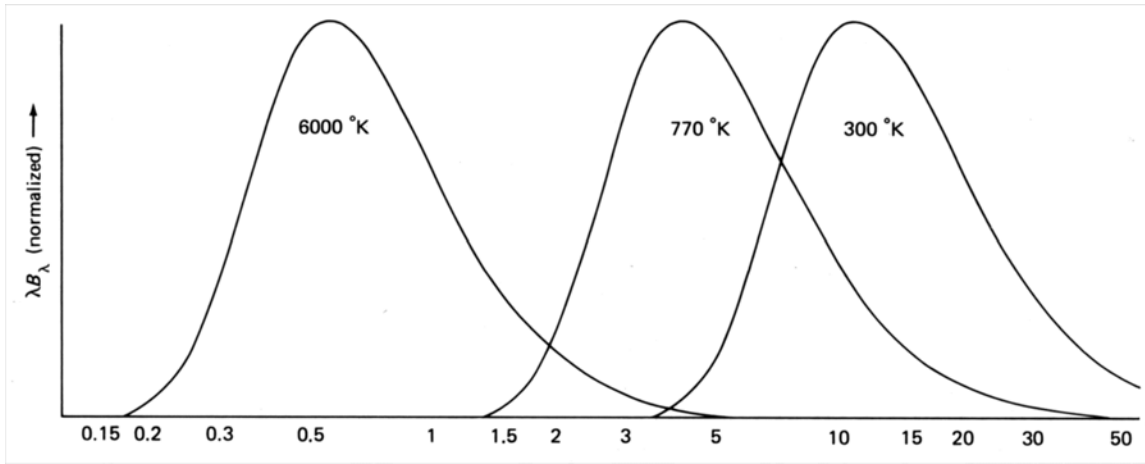


Figure 18. Normalized distribution of emission spectra for three blackbodies with absolute temperatures of 6000 K (Sun), 770 K (Forest Fires), and 300 K (Earth's surface) shows primary energy sources for each of the VIIRS spectral bands (Figure 2.7.1, Scorer, 1990).

The calibration process describes the conversion of energy measured by a meteorological sensor into engineering units of reflectance or brightness temperature and is critical to the accurate interpretation of VIIRS imagery. Since meteorological satellites “look” toward the Earth and emissions from the Earth are toward the direction of the same sensor, the engineering units for IR observations are in equivalent blackbody temperatures (EBBT). The term EBBT refers to the skin temperature required to produce the energy recorded by the sensor for a surface with unity emissivity. If two features in a satellite image had identical skin temperatures but different emissivities, the EBBT would be lower for the feature with the lower emissivity, as shown in Equation (2) or as approximated in Equation (3), if the observations were made through the exact, same atmosphere. In addition, if two features had identical skin temperatures and emissivities but were viewed through two different atmospheres, the EBBT of the features viewed through the most transmissive atmosphere would be higher.

At microwave wavelengths, Planck's Law shown in Equation (11) can be simplified, as shown in Equation 14. This expression, known as the Rayleigh-Jeans Law, states that energy emitted at microwave wavelengths is linearly proportional to temperature.

$$B_v(T) = (2K v^2 / c^2) T \quad (14)$$

The engineering units for the energy shown in Equation 14 became known as “brightness” temperature (BT). Initially, the term BT referred to the skin temperature required to produce the energy recorded by the sensor for a surface with unity emissivity. More recently, the term has since become widely used by those working in the infrared regions as well, although EBBT is the correct engineering unit for the infrared region. However, brightness temperature is more succinct and the concept is well recognized.

In addition, because meteorological satellites “look” toward the Earth, energy collected at wavelengths smaller than IR must be reflected from the Earth back toward the satellite sensor. Therefore, engineering units for bands that record reflected energy are in percent of the energy arriving at the top of the atmosphere (TOA), typically referred to as albedo or reflectance. There are two sources of energy to reflect to the sensor, solar and lunar. Only the DNV band is capable of collecting sufficient lunar energy to create a useful image.

The use of albedo or reflectance as engineering units for observations illuminated by the sun (or moon) eliminates variations in these observations that result from satellite position with respect to the local normal at the Earth’s surface, the sun, and the sensor scan geometry.

For example, assume that identical water clouds are observed at three locations:

- 1) at the satellite subpoint, over the equator, at the summer equinox, and with the sun directly overhead
- 2) at the satellite subpoint, over 40 degrees south latitude, at the summer equinox, and with the sun directly overhead
- 3) at 40 degrees south latitude at the summer equinox at the satellite subpoint with the sun setting on the horizon.

Clearly the total solar energy reflected from the cloud to the sensor is greatest for the first case, where the sun is nearly overhead, and continues to decrease for case 2 and even more for case 3. However, the microphysical properties or characteristics of the cloud have not changed in these three instances, only the characteristics of the observation. Therefore, it becomes necessary to compensate for variations in the meteorological satellite observations that are due solely to external factors. This correction is made in the solar regions by dividing the energy incident upon the sensor by the energy available at the top of the atmosphere, at the local normal to the Earth’s surface viewed by the sensor. The actual energy observed by the sensor is divided by the solar energy (F_o) in the VIIRS band multiplied by (1) the ratio of the mean Earth-Sun distance to the actual distance between the Sun and Earth and (2) the cosine of the solar zenith angle (SZA), i.e. the angle between the sun’s direct rays and the local normal to the Earth’s surface,. Thus, the actual TOA solar energy is also a function of the local normal of latitude (α), solar inclination (δ), and solar hour angle (η) as described in Equation (15):

$$F = F_o S (d_m/d)^2 \cos(SZA) \quad (15)$$

$$\text{Where } \cos(SZA) = [\sin \alpha \sin \delta + \cos \alpha \cos \delta \cos \eta] \quad (16)$$

Once the energy recorded at the VIIRS sensor is divided by TOA solar energy, as defined by Equation 15 and 16, an identical cloud observed in the three situations previously described will possess the same reflectances or albedos in each scenario.

5.2. VIIRS IMAGERY DATA

A detailed discussion is now presented on the spectral content of each VIIRS channel. The format followed is (1) an analysis of phenomenology of the bandpass, based upon theoretical calculations and (2) examples of the signatures in actual sensor data. A summary is provided in Table 9 of the bandpasses in the operational satellite sensors that most closely approximates the VIIRS imagery and moderate resolution channels.

Table 9. Bandpasses of Sensors that Closely Approximate VIIRS Imagery Resolution Bands.

Band	VIIRS Channel	Central Wavelength (μm)	Bandwidth (μm)	Satellite System and Channel	Wavelength Interval (μm)
1	DNB	0.7	0.4	DMSP/OLS L	0.58 - 0.98
6	I1	0.640	0.080	MODIS 1	.620-.670
9	I2	0.865	0.039	MODIS 2	.841-.876
13	I3	1.61	0.06	AVHRR 3A	1.628-1.652
16	I4	3.74	0.38	AVHRR 3B	3.55-3.93
21	I5	11.45	1.9	DMSP/OLS T	10.4 – 12.7

5.2.1. VIIRS Imagery Band I1 ($0.64 \pm 0.040 \mu\text{m}$)

5.2.1.1. Theoretical Basis for Band Interpretation

As shown in Figure 19, the VIIRS I1 band is contained within an atmospheric window with $\sim 30\%$ attenuation, resulting primarily from molecular scattering and to a lesser degree from absorption by ozone, oxygen and water vapor. Approximately 70% of the top of the atmosphere solar energy in this band arrives at the Earth's surface when water vapor concentrations are typical of a mid-latitude winter profile (Anderson et al., 1986). Energy in these relatively short wavelengths is scattered according to Rayleigh Theory, which means approximately equal amounts of energy are scattering in the forward and backward direction. The net effect of Rayleigh scattering on VIIRS Imagery is that the albedo or reflectance of pixels slowly increases as VIIRS scans from NADIR to edge of scan. Thus, in cloud-free conditions, over a relatively homogeneous, poorly reflective surface, such as the ocean, the albedo in the I1 Imager Band may increase from $\sim 2\text{-}3$ percent at NADIR and as much as 7-percent at edge of scan. While such effects are insignificant for manual cloud analyses, they may be important to other applications.

Noted in Figure 19 are the signatures for snow, vegetated land, bare soil, and ocean surfaces. The reflectivity of snow in this band is very high and appears very bright in the band while the ocean surfaces and vegetated land are very low and appear very dark. Bare soil has a moderate albedo of approximately 20 percent which should make it appear less bright than snow and much brighter than vegetated land and water regions.

Water clouds (e.g. stratus, cumulus, etc.) appear bright in this band because they typically have large particle “number concentrations.” Since the reflective power of a cloud is defined by its ability to scatter, known as its “scattering coefficient” and the particle drop size distribution and number concentration, these clouds are highly reflective. In terms of scattering efficiency, this means *water clouds have a relatively large optical thickness, even if their geometric thickness is relatively small*. Typical droplet concentrations for water clouds range between $100\text{-}500 \text{ cm}^{-3}$ (Table 4.2, Liou, 1992). On the other hand, cirrus clouds appear less bright in this wavelength because the optical depth of ice clouds is much smaller for a given geometric thickness due to their larger particle size and smaller number concentrations. Typical number concentrations for cirrus clouds are in the $0.01 - 0.1 \text{ cm}^{-3}$ range (Liou, 1992). In terms of scattering efficiency, this means *ice clouds have a relatively small optical thickness, even if their geometric thickness is relatively large*. Consequently, water clouds are typically very bright in this band while ice clouds may be only barely visible to the human analyst.

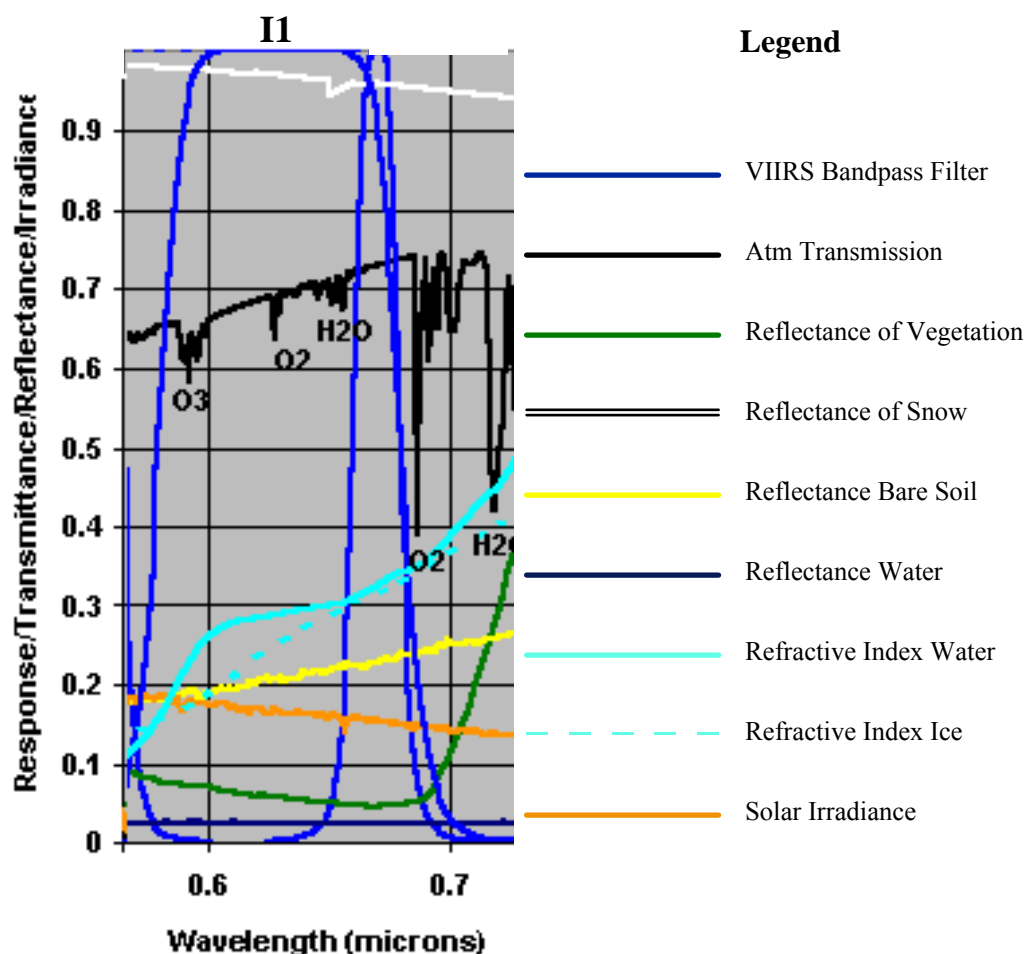


Figure 19. Spectral signatures in VIIRS I1 band shows snow with a very high reflectivity while vegetated land and ocean are very low. Signatures of water clouds and bare soil are similar.

5.2.1.2. Representative Imagery of the VIIRS I1 Band ($0.640 \pm 0.040 \mu\text{m}$)

Manual cloud detection of clouds in this band is based upon the concepts outlined in Section 3.1 that emphasized the importance of maximizing the contrast between clouds and the background. Manual cloud classification with the VIIRS I1 band emphasizes (1) texture, (2) spatial resolution of cloud elements, and (3) shadows which may be cast from clouds high in the atmosphere onto lower level clouds.

A manual interpretation of features contained in the VIIRS I1 band is demonstrated using the AVHRR Channel 1 imagery shown in Figure 20. This image was collected by NOAA-12 at about 7:05 AM local (1505 GMT) on March 19, 1996. Shown in the imagery is an area that extends approximately 1000 km in the north-south direction from near Portland, Oregon to Los Angeles, California and 1000 km in the east-west direction from the border of Utah and Nevada to the 130 degree west meridian. The large, San Joaquin Valley of California runs from the upper center through the bottom right of the image. The scene contains over a million AVHRR pixels with a nominal resolution of 1.1 km at NADIR.

An extensive area of highly reflective water clouds is evident over much of the left half of the image. These clouds are stratiform in the lower half and cumuliform toward the upper-left corner. Long, narrow cloud streaks, common with cirrus clouds, are seen in the middle-left through upper right corner of the scene and shadows from these cirrus clouds are cast upon lower-level water clouds. The presence of a frontal system is suggested in along the region where the cirrus is present and the lower-level water clouds change from stratiform to cumuliform. An extensive cloud-free, snow-covered region can be identified by the dendritic pattern seen in the right half of the scene, especially in the mountainous terrain contained in most of the lower right quadrant. However, it is very difficult to distinguish between land and water surfaces since the reflectivity of both are very low ($< 10\%$), as shown in Figure 19. A careful inspection does allow Lake Tahoe to be identified since it is nearly outlined by snow. Additionally, the arid regions of Nevada (far right hand side) which have a reflectivity greater than 20% are more pronounced than regions of the highly vegetated San Joaquin Valley, which have reflectivities less than 10%. Cirrus clouds are present in the bottom fifth of the scene, again identified by their smooth, wispy texture over the San Joaquin Valley and shadows cast upon lower-level water clouds toward the bottom-left corner of the scene.

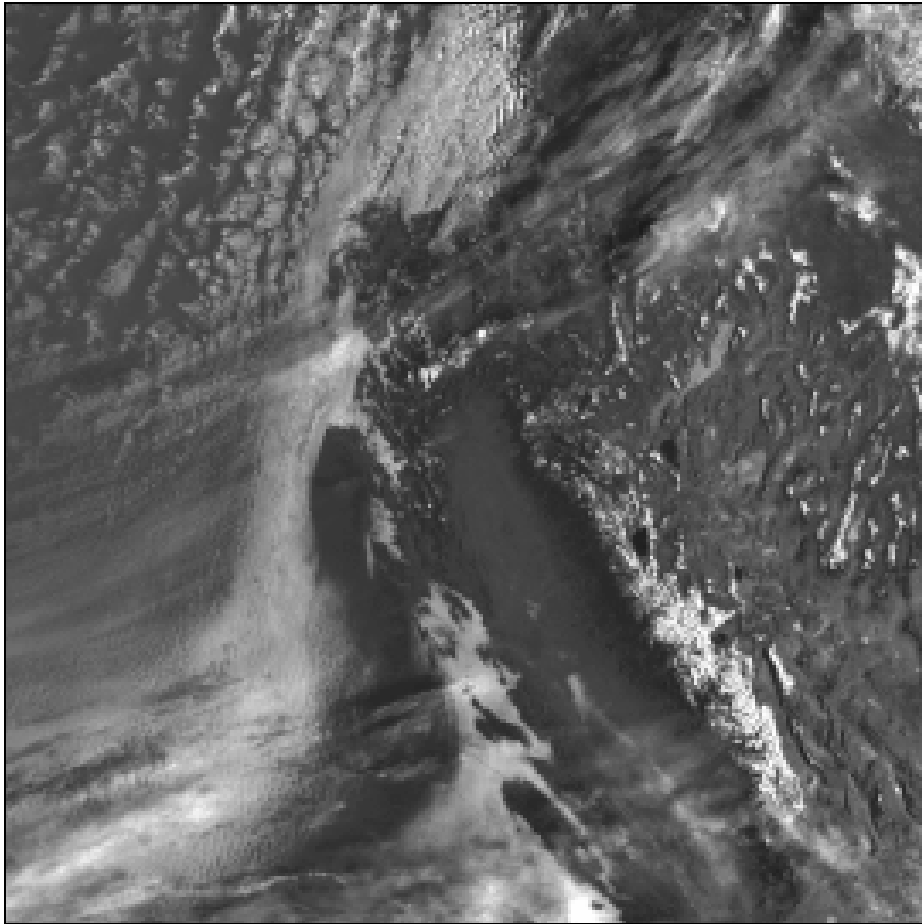


Figure 20. Signatures of clouds and land surfaces typical of those present in the VIIRS I1 band are seen in the NOAA-12 AVHRR channel 1 imagery collected near San Francisco, CA on February 19, 1996 (Hutchison et al., 1997).

5.2.2. VIIRS I2 Band ($0.865 \pm 0.020 \mu\text{m}$)

5.2.2.1. Theoretical Basis for Band Interpretation

As shown in Figure 21, the VIIRS I2 band is contained within an atmospheric window with less attenuation than that of the I1 band. This higher transmission results from a reduction in molecular scattering by the atmosphere because the longer wavelength is affected less by Rayleigh or molecular scattering. Also, notice that the I2 band contains no significant water vapor absorption bands which further increases transmission in the bandpass. Energy at wavelengths in the VIIRS I2 band is reduced by Mie scattering events, e.g. water vapor and aerosol particles, however, these particles make up only a small portion of the atmosphere in contrast to the molecular atmosphere which impacts the I1 band. Therefore, over 80% of the top of the atmosphere solar energy in this band arrives at the Earth's surface. Another significant difference between the I1 and I2 band is the increased reflectivity of vegetated land, compared to bare soil. The reflectivity of bare soil was greater than vegetated land in the I1 channel but the reverse is true in the I2 channel. The reflectivity of water clouds has also increased between the I2 and I1 bands, while the reflectivity of water surfaces remains very low as it was in the I1 band. Finally, the I2 band is designed to be more narrow than the earlier AVHRR Channel 2. Narrowing the band from $0.3 \mu\text{m}$ AVHRR bandpass to a $0.039 \mu\text{m}$ VIIRS bandpass reduces variations due solely to water vapor absorption. For example, one strong absorption band complex at $\sim 0.83 \mu\text{m}$ was contained in the AVHRR Channel 2 imagery but has no effect on the VIIRS I2 band. The reduction in channel bandpass has little effect on cloud signatures since these features reflect very large amounts of energy to the VIIRS sensor. However, narrowing the AVHRR band to the VIIRS $0.039 \mu\text{m}$ bandwidth significantly reduces global variations in the signatures of many lower reflectivity surfaces that would have changed due solely to variations in atmospheric water vapor content as the NPOESS satellite orbits the Earth. For example, VIIRS imagery will provide more accurate NDVI than AVHRR since VIIRS channels experience smaller day-to-day variations due to changes in the composition of the atmosphere.

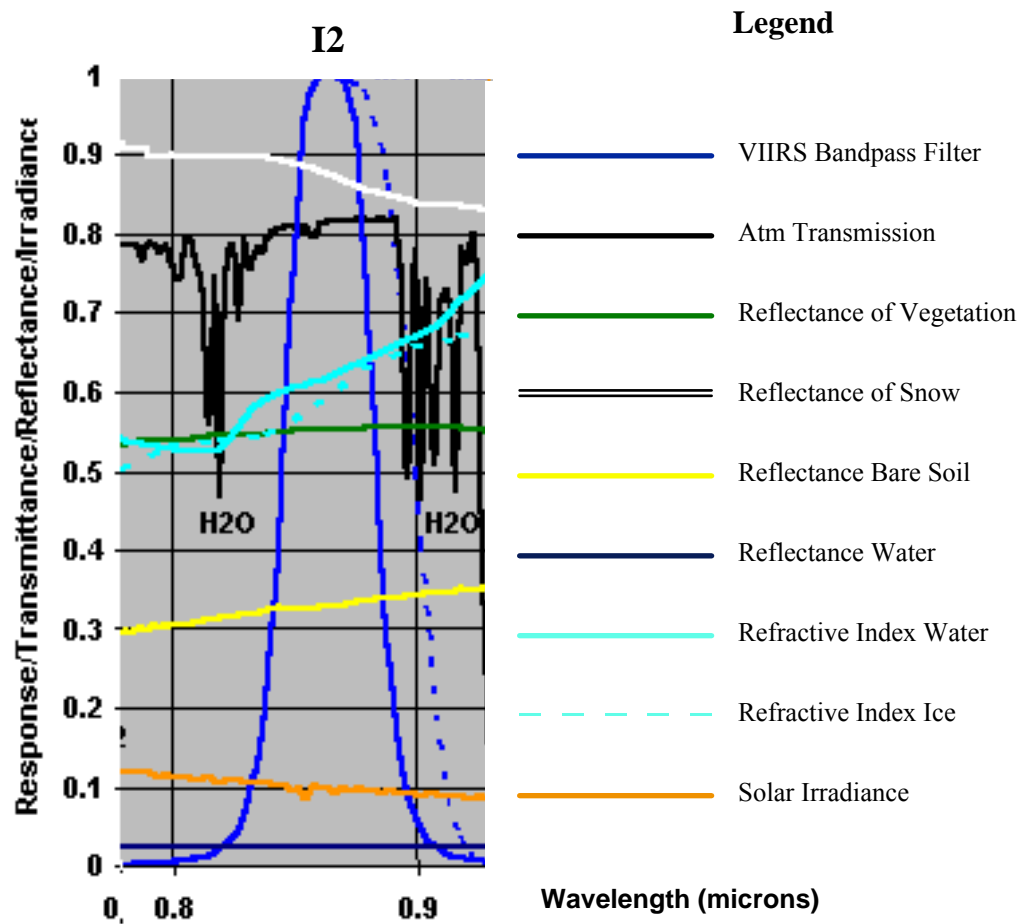


Figure 21. Spectral signatures in the VIIRS I2 band shows snow, water clouds and vegetated land with high values of reflectivity while water surfaces remain very low. The reflectivity of vegetated soil is now higher than that of bare soil.

5.2.2.2. Representative Imagery of the VIIRS I2 Band ($0.865 \pm 0.020 \mu\text{m}$)

A manual interpretation of features contained in the VIIRS I2 band is demonstrated using the AVHRR Channel 2 imagery shown in Figure 22. This image is of the same scene shown in Figure 20. The most striking difference between Figures 20 and 22 is the ability to clearly see fine details in the land structure of the latter where little was evident in the former, since the reflectivity of vegetated land is nearly 60% in the VIIRS I2 band but less than 10% in the I1 channel. Thus, the I2 band is highly useful for detecting land-sea boundaries, e.g. even the Sacramento River's basin is visible in this figure as it extends down the middle of the San Joaquin Valley just west of Lake Tahoe. Signatures of water clouds are similar in both the VIIRS I1 and I2 bands, although the I1 band is more useful for creating manually-generated CNC masks since the contrast between clouds and their surrounding backgrounds is greater in the I1 band than the I2 band.

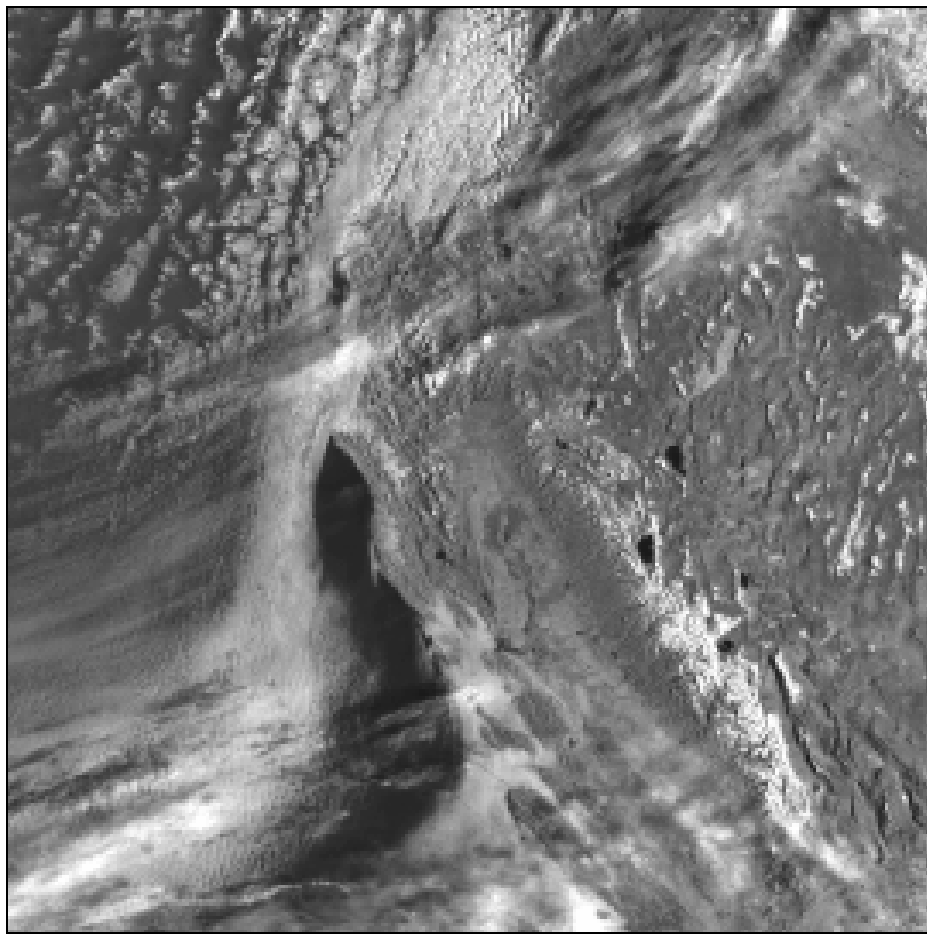


Figure 22. Signatures of clouds and land surfaces typical of those present in the VIIRS I2 band are seen in the NOAA-12 AVHRR channel 1 imagery collected near San Francisco, CA on February 19, 1996 (Hutchison et al., 1997).

Figure 23 contains SeaWiFS data collected in the very narrow 0.845 – 0.885 μm band planned for the VIIRS I2 band. This scene was collected on July 13, 2001 over the Gulf of California. Notice the sharp contrast between water and land boundaries. In addition, variations in surface vegetation can be seen, especially around the Salton Sea in the upper left portion of the image. Comparisons between these data and those contained in VIIRS 0.412, 0.488, and 0.555 μm bands show the effects of surface reflectivity upon these imagery contents.

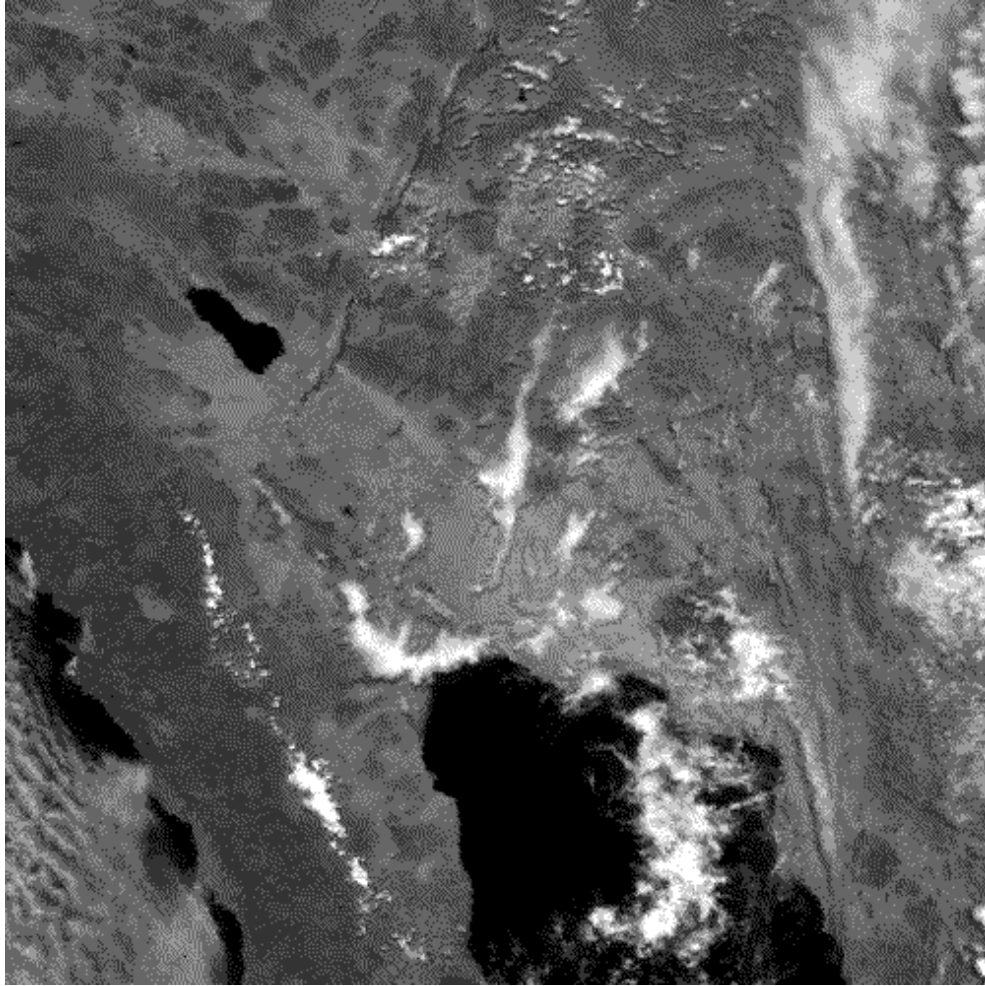


Figure 23. Signatures of clouds and land surfaces typical of those present in the VIIRS I2 band are seen in the SeaWiFS data collected over Southwestern US on July 13, 2001 as also shown in Figure 45.

5.2.3. VIIRS I3 and M10 Bands ($1.61 \pm 0.03 \mu\text{m}$)

5.2.3.1. Theoretical Basis for Band Interpretation

The VIIRS I3 and M10 bands are contained within a relatively clean atmospheric window with a transmission over 90 percent. Attenuation in this band comes from the wings of water vapor absorption lines that extend into the bandpass; however, attenuation does not reach 10% in the band even in relatively humid atmospheric conditions. From figure 24 it is seen that atmospheric transmission is nearly zero at $1.4 \mu\text{m}$ but rapidly increases to its maximum at about $1.58 \mu\text{m}$ where it remains through about $1.75 \mu\text{m}$. Therefore, the region from 1.58 - $1.75 \mu\text{m}$ is useful for a VIIRS channel.

The $1.61 \mu\text{m}$ band is most valuable for the interpretation of snow-covered surfaces due to the large differences in reflectivity between snow and other features in this band. For example, the reflectivity of snow is seen in Figure 24 to reach a minimum at about $1.5 \mu\text{m}$ and remain very small through $1.58 \mu\text{m}$ at which point it begins to slowly increase and reaches approximately 5% at $1.64 \mu\text{m}$. On the other hand, the reflectance of bare soil, vegetated soil, and water clouds are significantly larger, e.g. 30-50 percent. Therefore, the contrast between snow and these features is strong in the $1.61 \mu\text{m}$ band making the I3 band very useful to confirm the presence of snow when used in conjunction with the I2 band where only the signature of snow changes significantly.

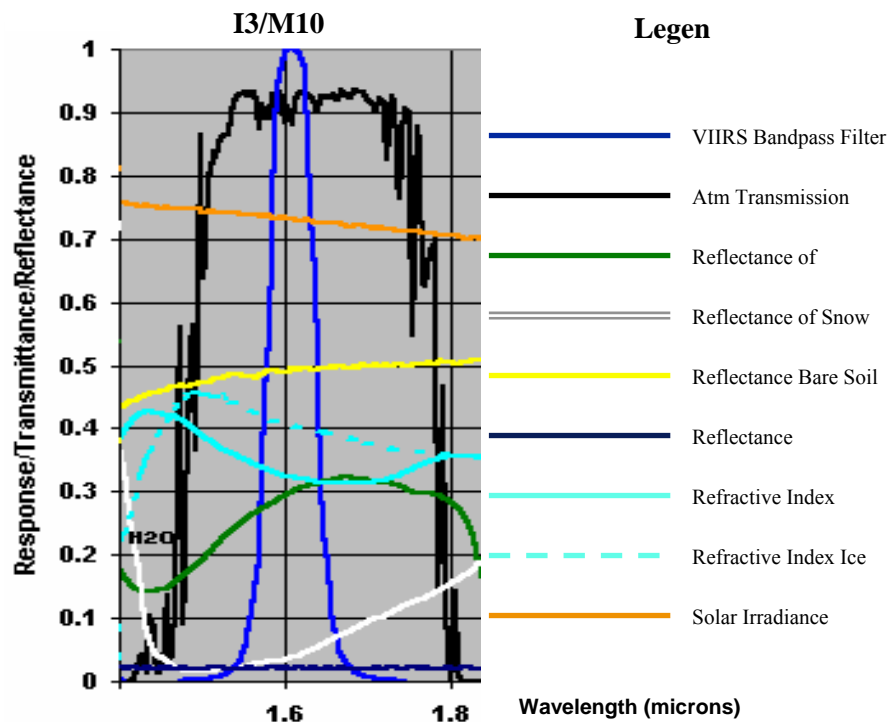


Figure 24. Theoretical calculations of atmospheric and surface properties in the $1.61 \mu\text{m}$ band that constitutes the VIIRS I3 and M10 channels

5.2.3.2. Representative Imagery of the VIIRS I3/M10 Band ($1.61 \pm 0.03 \mu\text{m}$)

The 1.61 μm channel was first carried in space by the DMSP sensor in the late 1970s based upon the theoretical work of Valovcin (1978). A sensor known as the Snow Cloud Discriminator was first flown on DMSP spacecraft in the late 1970s; however, data in the 1.61 μm channel were not routinely collected until NASA launched the Thematic Mapper (TM) sensor in the early 1980s onboard the Landsat Earth Resources Satellite series. NOAA launched the first operational 1.6 μm channel (i.e. Channel 3a or the albedo channel) on the TIROS NOAA-K system in 1999. However, due to bandwidth limitations, TIROS satellites could only downlink either Channel 3A or Channel 3B. Channel 3B, or channel given in brightness temperatures, collected data in the 3.7 μm band. Thus, there is a wealth of research and operational sensor data available to demonstrate the phenomenology described above. For convenience, data from the Thematic Mapper are shown in Figure 25 along with the 0.64 μm imagery typical of VIIRS Channel I1.

Snow is readily identified in Figure 25 by comparing features in the 0.645 and 1.61 μm channels. Snow appears very bright in the shorter wavelength and completely black in the 1.61 μm imagery. At the same time, clouds are relatively bright in both bands. Note also, the vegetation surrounding the lake region is much brighter at 1.61 μm than at 0.64 μm . From Figure 24 it is seen that the reflectivity of vegetated land is about 30 percent at 1.61 μm while its reflectivity was only about 5 percent in the I1 Band as seen in Figure 19. All features in Figure 25 are in good agreement with information shown in Figures 19 and 24.

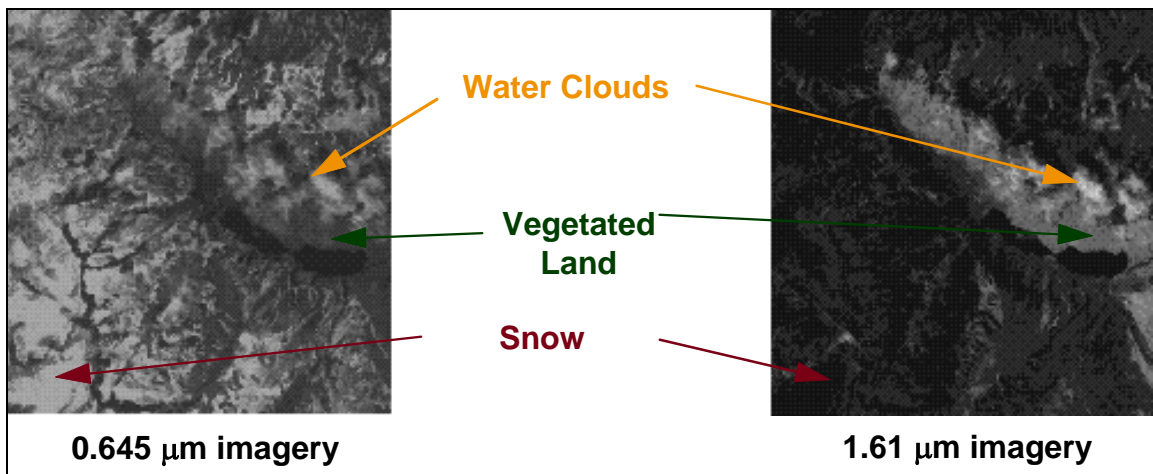


Figure 25. Thematic mapper data collected over the Sierra Nevada mountains show the value of 1.61 μm imagery for differentiating between water clouds (bright in both bands) and snow (black in only the 1.61 μm image).

5.2.4. VIIRS I4 Band $3.74 (\pm 0.19 \mu\text{m})$ and M12 Band $3.7 (\pm 0.09 \mu\text{m})$

5.2.4.1. Theoretical Basis for Band Interpretation

Due to the complexity of signatures within it, perhaps more information has been published in the literature about the $3.7 \mu\text{m}$ band than any other spectral band carried by meteorological satellites. Certainly, more space is allocated to $3.7 \mu\text{m}$ band in this text than any other VIIRS channel. The band was originally called AVHRR Channel 3 on early TIROS spacecraft but became known as Channel 3B with the launch of the NOAA-K or NOAA-13 satellite that carried the first $1.6 \mu\text{m}$ channel. During NPOESS era, the band becomes the VIIRS I4 Imagery Band with a bandpass of $3.55\text{-}3.93 \mu\text{m}$, very similar to the original AVHRR Channel 3. Highlights of information published in the literature on this bandpass are summarized in this section.

The $3.7 \mu\text{m}$ band was made a VIIRS Imagery Channel (band I4) to satisfy Threshold requirements for the VIIRS manually-generated cloud type EDR, i.e. the VIIRS I4 band is essential to manually distinguish between stratus and cirrus clouds in nighttime data. Information collected in the I4 bandpass is also needed at much higher signal-to-noise performance for the retrieval of other NPOESS EDRs, such as sea surface temperature – a NPOESS Key EDR. Therefore, it was also necessary to include the $3.7 \mu\text{m}$ bandpass as a separate (M12) moderate resolution band since the required signal-to-noise could only be achieved at a lower spatial resolution. The M12 moderate resolution (imagery assist) Band has a narrower bandpass ($3.61\text{-}3.79 \mu\text{m}$) than the I4 Band to reduce the effects of global variations in atmospheric attenuation due primarily to water vapor as shown in Figure 26.

Interpretation of signatures in the I4 band ($3.55\text{-}3.93 \mu\text{m}$) is more difficult than most VIIRS channels since it, as well as moderate resolution bands M12 and M13, may contain energy from two sources: the sun and the Earth. This is seen by close inspection of Figure 18, which showed the normalized distribution of emission spectra for blackbodies with absolute temperatures of 6000 K (sun) and 300 K (Earth's surface). These curves overlap in the $3\text{-}5 \mu\text{m}$ region. From Figure 26, it is seen that solar irradiance falls off sharply at wavelengths longer than about $4.2 \mu\text{m}$, which correlates with an extremity of the M13 bandpass. Even though interpretation of $3.7 \mu\text{m}$ imagery may be complicated, the wealth of information that can be extracted from this channel ensures it will remain most valuable throughout the foreseeable future.

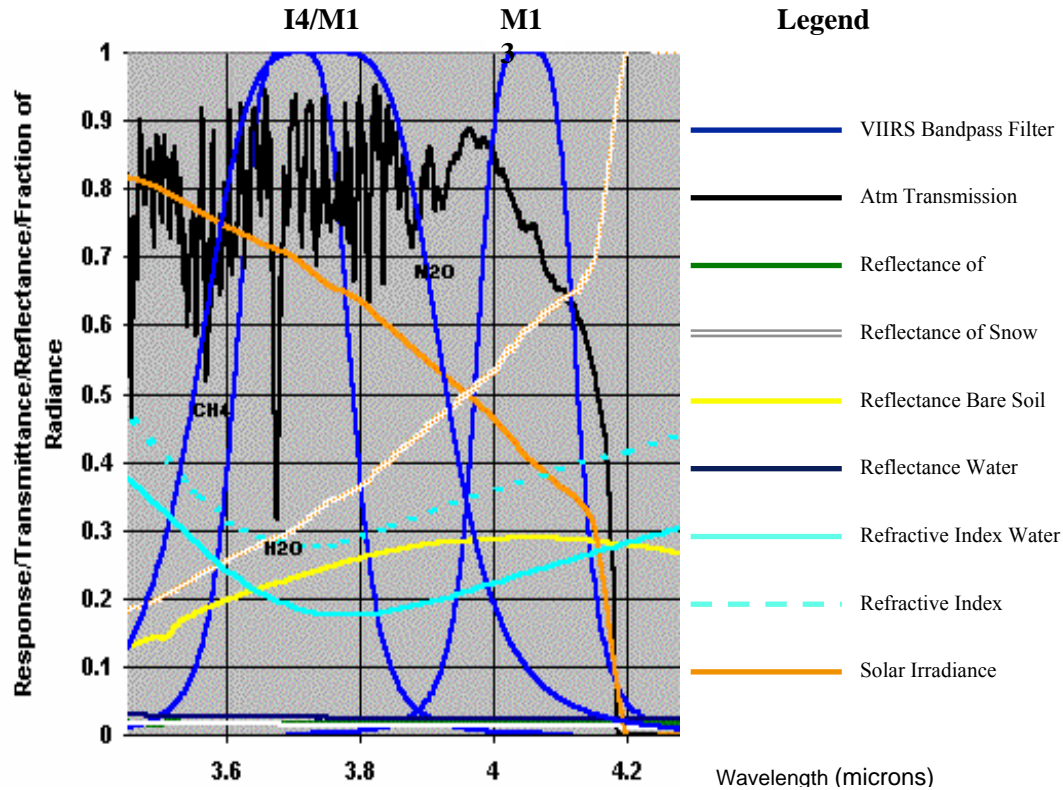


Figure 26. Theoretical calculations of atmospheric and surface properties in the 3.7 μm band that constitutes the VIIRS I4 and M12 channels

As previously noted, the 3.7 μm bandpass was first flown on NOAA's TIROS series satellite to improve sea surface temperature retrievals through better atmospheric correction of attenuation caused by water vapor. Observations in two spectral bands in which water vapor attenuation was sufficiently different allowed the amount of water vapor to be estimated based upon the brightness temperature difference in the bands, assuming a priori knowledge of ocean emissivity (Anding and Kauth, 1970, 1972). It was concluded that SST retrievals with an accuracy of 1K would be possible using observations made in multiple infrared (McMillin, 1984). Soon thereafter, all AVHRR satellites also carried the long-wave, split window channels known as AVHRR Channel 4 and Channel 5. The relationship between total atmospheric water vapor and attenuation in AVHRR IR channels is shown in Figure 27. In the VIIRS sensor, corresponding channels are I4, M15, and M16. For the M12 band, attenuation due to water vapor absorption is less than shown in Figure 27.

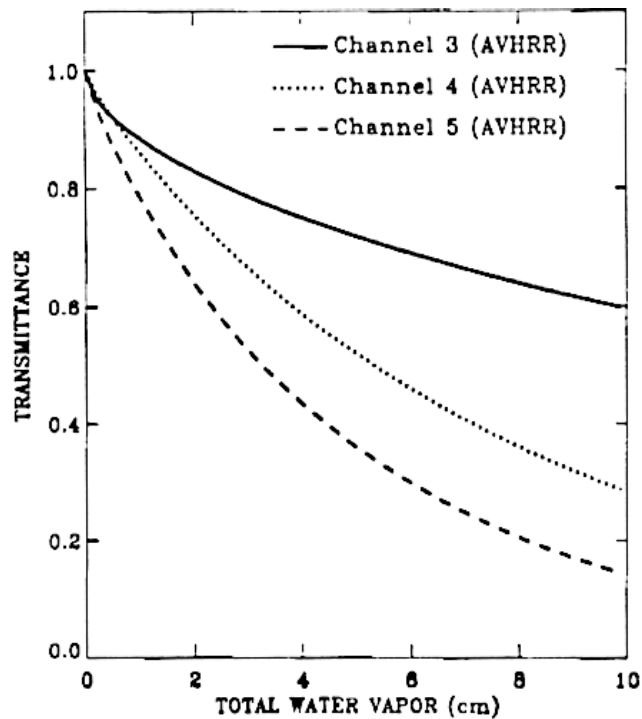


Figure 27. Atmospheric attenuation in AVHRR 3.7, 10.8, and 11.8 μm IR channels as a function of total atmospheric water vapor (Hutchison et al., 1995).

While the feasibility of retrieving improved SST fields was demonstrated soon after the launch of the AVHRR sensor, there remained the challenge of detecting cloud contamination pixels and removing them from the SST analyses. In particular, identifying stratus in nighttime imagery and thin cirrus in both daytime and nighttime imagery was problematic. Prior to the launch of AVHRR, even the most sophisticated automated cloud classification schemes, such as the RTNEPH Model developed by the United States Air Force (USAF) Weather Agency (AFWA), had difficulty detecting these clouds due to the relatively small thermal contrasts that could exist between them and their cloud-free surroundings. Therefore, significant effort was expended to correct bad analyses by highly trained satellite meteorologists who performed quality control (QC) of the automated cloud analyses by manually comparing them against high-resolution satellite imagery collected by the Operational Linescan System (OLS) flown by the Defense Meteorological Satellite Program (DMSP). The OLS collected imagery at 0.65 km with a near-constant cross scan resolution and carried a photo-amplified sensor that allowed visible imagery to be collected at night under conditions of at least one-quarter lunar illumination. This nighttime visible sensor is the forerunner to the VIIRS Daytime/Nighttime Visible (DNB) Imagery channel (c.f. Section 5.2.6). However, the positive identification of nighttime stratus clouds by human analysts continued to be very difficult.

The automated detection of clouds, especially nighttime stratus and thin cirrus clouds, was greatly enhanced using the multiple spectral bands carried by AVHRR. In 1984, Wang (1984) demonstrated that the contrast between nighttime stratus and ocean surfaces was greatly enhanced in the brightness temperature difference (BTD) field which is

created by subtracting the AVHRR 3.7 μm brightness temperatures from the AVHRR 11.0 μm brightness temperatures, i.e. ($\text{BT}_{11.0} - \text{BT}_{3.7}$). The increased contrast resulted from differences in emissivity of stratus clouds at these two wavelengths, not in the blackbody temperatures of the cloud and surrounding background. Stratus clouds have an emissivity of about 0.8 at 3.7 μm but nearly 1.0 at 11.0 μm . Based upon Equation 3, this difference in emissivity results in a nearly 20 percent difference in energy measured in these two bands. Thus, brightness temperatures of stratus in the 3.7 μm band are as much as 4 K colder than in the 11.0 μm band.

The impact of undetected cirrus clouds upon SST analyses is more critical than stratus due to the colder radiating temperatures and variations in transmissivity of these clouds. Inoue (1985) demonstrated that the contrast between cirrus and its surroundings could be greatly enhanced by looking at the feature $\text{BT}_{11.0} - \text{BT}_{12.0}$ in a composite of two AVHRR images. Saunders and Kriebel (1988) summarized and extended the work of numerous earlier investigations in new formalism that exploits bi-spectral methods for improved cloud clearing for SST analyses. From this point forward, multispectral analyses became the fundamental technology used in the meteorological analysis of remote-sensed satellite data. More recently, the increased value of using bi-spectral test based upon the 3.7 μm and 12.0 μm channels was demonstrated to further improve the capability for automated thin cirrus detection (Hutchison et al., 1995; Stowe et al., 1991).

Snow-cloud discrimination became another very useful application for the 3.7 μm imagery. As seen in Figure 26, the reflectivity of snow is nearly zero in the 3.7 μm band. In fact, its reflectivity is even smaller in the I4 band than it is in the 1.6 μm region. Therefore, it was believed that accurate snow maps could be generated from daytime AVHRR Channel 3 data if the thermal or terrestrial radiation in the observed radiance could be isolated and removed from the solar component. Initial attempts proved successful in differentiating between snow and water clouds; however, the presence of cirrus (ice) clouds was problematic (Allen et al., 1990). Subsequently, a different approach was taken to segregate the thermal and solar components of the 3.7-micron band for snow and cloud detection (Hutchison et al., 1997a). This new approach simultaneously enhanced the signature of thin cirrus clouds and suppressed the signature of snow making it possible to (1) differentiate water clouds from snow, (2) differentiate snow from ice (cirrus) clouds, and (3) differentiate water clouds from thin cirrus clouds, although some ambiguity exists for cirrus clouds with larger optical depths (Hutchison et al., 1997b). In fact, the procedure even allowed snow to be manually classified in the presence of overcast thin cirrus clouds using only signatures in the solar channels rather than longwave infrared channels (Hutchison and Locke, 1997).

Numerous additional applications have been developed with the 3.7 μm channel, including (1) forest fire detection and (2) retrievals of cloud optical depth and cloud effective particle size to name a few. In addition, other phenomenology effects on 3.7 μm signatures have been described in the reference materials (Scorer, 1990; Chapter 5 titled: Channel 3).

5.2.4.2. Representative Imagery of VIIRS I4 Band ($3.74 \pm 0.19 \mu\text{m}$)

The phenomenology contained in the $3.7 \mu\text{m}$ channel is now demonstrated with sample imagery. By convention, the engineering unit of the $3.7 \mu\text{m}$ channel is brightness temperature since albedo is meaningless unless the thermal radiances are removed from the signature. In general, warmer surface temperatures produce more energy at the sensor than colder temperatures. Digital data generated by the sensor associates larger amounts of energy with higher digital values and smaller amounts of energy with lower digital data. Since most satellite analysts prefer to see “white” clouds, IR data are typically displayed in the inverted mode, i.e. colder temperatures appear brighter than warmer temperatures, opposite the way visible data are displayed. Thus, warmer radiating surfaces appear darker in inverted IR imagery because they produce higher energy levels at the sensor. Conversely, colder radiating temperatures produce smaller energy levels at the sensor and appear brighter in imagery displayed in the inverted mode.

Confusion can arise in the display $3.7 \mu\text{m}$ imagery because the total radiance consists of a thermal emission and a solar reflection terms. Unlike normal situations in which the amount of energy scattered by water clouds increases with particle size, in the $3.7 \mu\text{m}$ channel, the energy scattered by water clouds increases as the particle size decreases. Therefore, solar radiation in the $3.7 \mu\text{m}$ band is totally absorbed by large ice particles and cumuliiform water clouds (Scorer, 1990). On the other hand, solar energy scattered to the sensor increases for stratiform clouds that have smaller droplet sizes. Thus, low-level (warm) stratiform clouds appear most bright and high-level (cold) ice clouds appear most dark when $3.7 \mu\text{m}$ imagery is displayed in the inverted mode. Detailed discussions follow on the signatures in the $3.7 \mu\text{m}$ band.

5.2.4.2.1. Sea Glint and the Absence of Sky Light (excepts from Scorer, Chapter 5)

There is a ‘blip’ in the curve of the refractive index of water that overlaps the VIIRS I4 band of wavelengths. This blip has the effect of producing a very strong reflected beam when radiation in the $3.7 \mu\text{m}$ imagery band impinges on a water surface, including oceans and inland lakes. (Scorer, 1990) No similar effect is indicated with ice. The reflection can be so bright at low angles of incidence, such as occur towards the eastern horizon for the early morning satellite or the western horizon of the afternoon satellite, that it may be possible to saturate most radiometers. No detail is available in the area of such strong sun glint unless the sea is quite rough. Conversely, when the sea is rough in an area of very bright glint, it is darkened.

In the region of sea glint, the sun appears as a very bright source of $3.7 \mu\text{m}$ radiation in an otherwise very dark sky, much as it appears on the moon due to an absence of sky light. Thus, illumination in the band results from direct sunshine and shadow areas are very dark. Evidence to the absence of skylight is seen in very sharp boundaries on the dark shadows that cirrus projects onto layers of lower clouds (Scorer, 1990). The terminator (which is the boundary of direct sunshine) is very difficult to identify in the $3\text{--}7 \mu\text{m}$ band because the thermal emission from the surface and clouds is comparable with the weak

sunshine in such areas. For example, it is easy to view clouds and some shadows in the I2 band for an area deep into regions where the sun has not risen or long since set due to illumination from the atmosphere above the cloud. But in the $3.7\mu\text{m}$ band, no such shadows are seen and as clouds are located further toward the nighttime areas, only the sun-facing edges of progressively higher clouds show any illumination. The lack of skylight coupled with simultaneous emission of thermal energy creates imagery that appears completely different than that seen in any other band (Scorer, 1990). Examples are shown from the early morning NOAA AVHRR scene contained in Figure 28. These data show an extensive area of sunglint surrounding Florida with the terminator located near the left-bottom corner of the scene.

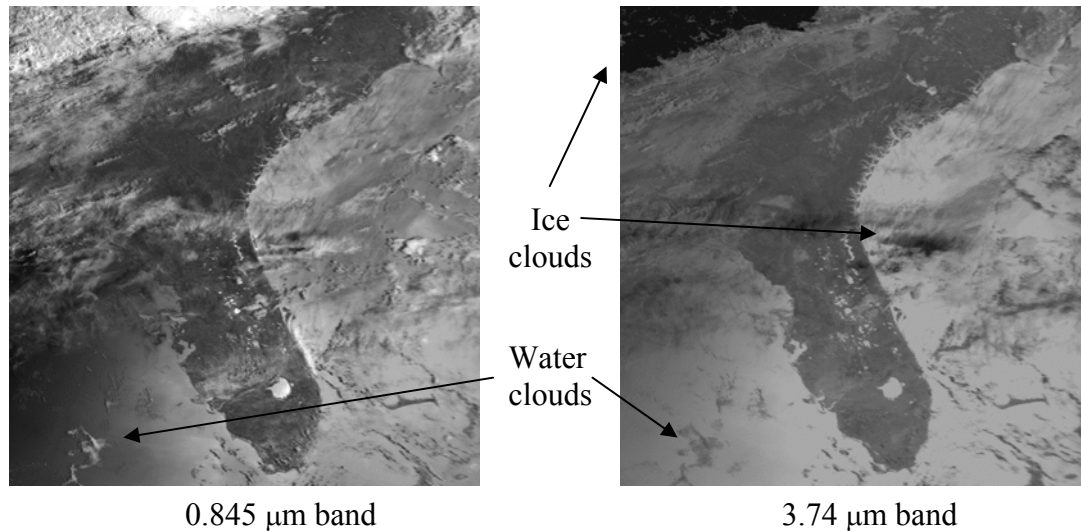


Figure 28. Sunglint in AVHRR Channel 2 and Channel 3 bands of NOAA-15 mission over southeastern United States.

Notice in Figure 28 that land and cloud-free ocean features appear similar in both AVHRR Channel 2 ($0.845\mu\text{m}$ band) and Channel 3 ($3.7\mu\text{m}$ band). Water surfaces appear very bright with sea glint occurring on most of these surfaces. However, clouds appear very different in these two spectral bands. Dense clouds in the upper left-corner appear very bright in the Channel 2 imagery but black in Channel 3. Also, note that in the Channel 2 imagery shadows are cast from the high clouds upon lower clouds just east of Cape Canaveral but no shadows are seen in Channel 3 owing to the absence of skylight. This region simply appears black due to the strong absorption by large particles in this region of thunderstorms. At the same time, cumulus “streets” running in a north-south direction over land west of the Cape appear bright in both bands while similar clouds in the lower left-corner of the image are more bright toward the center in Channel 2 but more dark toward the center in Channel 3. In Channel 2, the thickest part of the cloud produces the brightest signature because this part of the cloud is most highly reflective to the source of radiation which is the direct rays of the sun. In Channel 3, the thickest part of the cloud is most dark because these particles strongly absorb solar radiation and in this case, in the absence of skylight, the source of radiation is the reflected solar energy from the oceans surface. Thus, the centers of the clouds must attenuate solar energy more strongly than the edges in order for the centers to appear

more dark and the edges more bright.

The combined effects of the absence of skylight and presence of sunglint in 3.7 μm satellite imagery are summarized as follows. Together these effects make clouds appear as though the human were viewing the clouds in direct sunlight from the Earth's surface (Scorer, 1990). The thickest part of a water cloud appears most dark because less energy from below penetrates them. The thinner parts of a water cloud appear brighter because the sun's energy reflected from the ocean surface is transmitted through them. Cirrus clouds, however, appear black because these large particles strongly absorb energy in the 3.7 μm band whether its source is sky radiation from above or reflected solar energy from the ocean below.

5.2.4.2.2. Nighttime Stratus Clouds

As noted earlier, the accurate detection and typing of nighttime stratus requires the use of data in the 3.7 μm spectral band. Before data were available from the 3.7 μm region, nighttime stratus was difficult to detect over surfaces where the Earth's skin temperature was nearly identical to the cloud top temperature in the long wavelength (12.0 μm) IR bands. The contrast between nighttime stratus and ocean surface skin temperature is greatly enhanced in the 3.7 μm band due to differences in emissivities between stratus clouds and the ocean's surface. As noted in Equation 3, there are three primary factors that determine the amount of IR radiation arriving at the VIIRS sensor: emissivity of the surface, blackbody temperature of the surface, and transmission of the atmosphere across the channel bandpass. Thus a difference of 20 percent in emissivity between the cloud-free surface skin temperature (1.0) and the stratus cloud (0.8) results in as much as 4 K difference in brightness temperature between these features when viewed in the 3.7 μm band.

The NEdT performance estimate for VIIRS band I4 is 0.92 K for a source brightness temperature of 270 K. Thus, we expect the difference in emissivity between the stratus cloud and the cloud-free ocean surface to be sufficient to allow the clouds to be detected and identified in the VIIRS I4 band. This is demonstrated in the AVHRR imagery shown in Figure 29.

Figure 29 contains an extensive area of stratus that is routinely found off the coast of San Francisco, especially during the summer. In the right panel is the long wavelength IR channel typically available on most sensors, even before the launch of AVHRR. This particular image contains Channel 4 which is centered near 11.0 μm . Skin temperatures of water surfaces are shown for Lake Tahoe at 18.6 C since the ocean was completely cloudy. The stratus temperature is 11.0C in the same band. On the other hand, the brightness temperature in the 3.7 μm band is 1.1K warmer for cloud-free Lake Tahoe but 5.4 K colder for the stratus cloud. Since Lake Tahoe is rather high in the Sierra Nevada mountains, atmospheric attenuation due to water vapor (shown in Figure 27) causes the 1.1K difference in brightness temperatures between these bands while the variation in surface emissivity causes the 5.4K difference in these bands in the stratus cloud brightness temperatures. Certainly, in difference between brightness temperatures for stratus is explained primarily by difference in emissivity of the stratus at these two wavelengths. The leading edge of the stratus cloud is clearly seen extending into the San Joaquin Valley in the 3.7 μm imagery while the same edge is not distinct in the 11.0 μm channel.

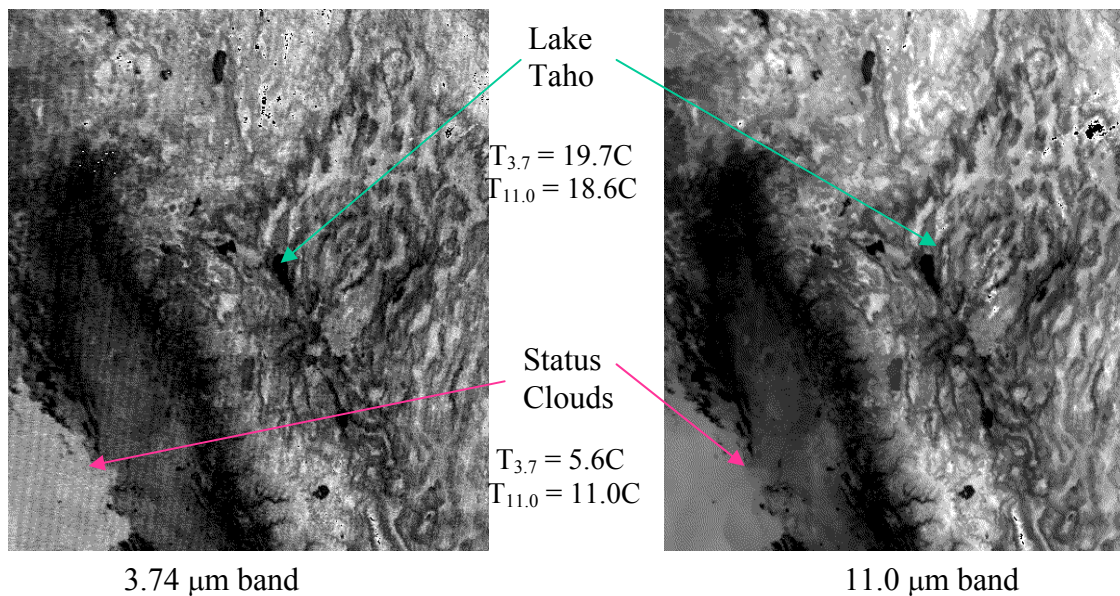


Figure 29. Stratus over San Francisco Bay and coastal California in nighttime 3.7 μm and 11 μm imagery collected by NOAA-14.

5.2.4.2.3 Snow/Cloud Discrimination

Figure 30 demonstrates the challenge of differentiating between snow and clouds in AVHRR imagery using only bandpasses similar to the VIIRS I1 and I5 channels. The scene is from NOAA-14 collected at 2:20 PM PST [2220 GMT] on December 18, 1996. It covers the same area described in Figure 20. From left, the panels contain AVHRR channels 1, 3, 5, [similar to VIIRS I1 band at $0.64\text{ }\mu\text{m}$, I4 band at $3.74\text{ }\mu\text{m}$, and I5 band at $11.5\text{ }\mu\text{m}$]. An extensive area of stratus is seen in the San Joaquin Valley, in the center of the $0.64\text{ }\mu\text{m}$ band, nearly parallel to the snow-covered Sierra-Nevada Mountains. In the $3.75\text{ }\mu\text{m}$ channel, ice clouds appear white along with snow while thicker [colder] cirrus appears brighter in the $12.0\text{ }\mu\text{m}$ band. It is apparent from these images that the spectral signatures of cirrus clouds and snow are similar in all the AVHRR channels and differ only in relative strength. Thus, while the dendritic pattern in Channel 1 makes snow along the mountains relatively easy to recognize, other snow-covered areas are difficult to identify with certainty.

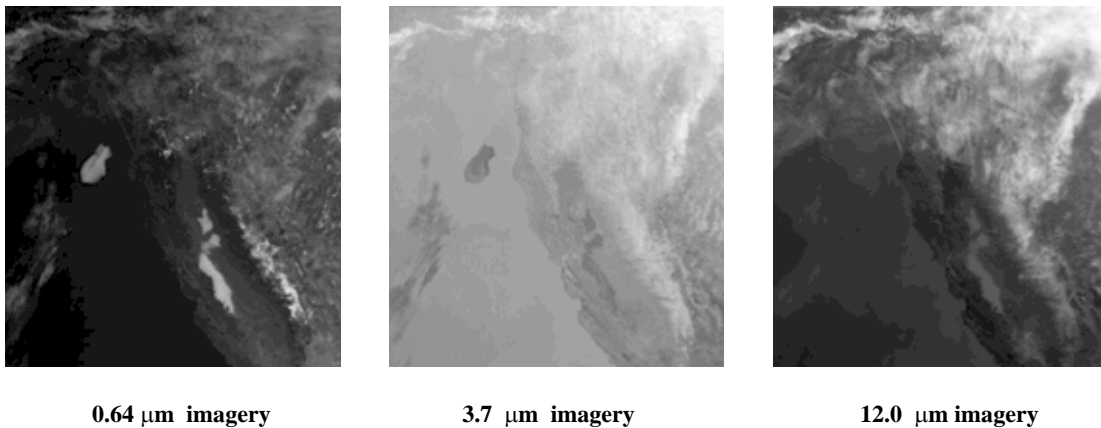


Figure 30. Channels 1,3, and 5 of NOAA-12 imagery collected at about 7:05 AM PST on March 19, 1996 over western United States and Pacific coastal regions.

The solar and thermal components of the I4 band can be segregated into two distinct images that are highly useful for several applications, including snow-cloud discrimination and cloud top phase classification, as discussed in the next section. The former is most valuable for differentiation between snow and ice clouds. It is also useful for detecting water clouds and snow in the absence of $1.6\text{ }\mu\text{m}$ data, which could result from VIIRS sensor degradation. Analysis of cloud phase is useful for the vertical placement of clouds in the atmosphere, since ice clouds are typically higher in the atmosphere than water clouds. A brief overview of the procedure used to create two spectral bands is provided next.

The $3.7\text{ }\mu\text{m}$ daytime albedo (reflectance) band can be created by modifying the observed VIIRS radiances for thermal emissions and converting the resultant values into albedo as follows. The $12.0\text{ }\mu\text{m}$ skin temperature of each pixel is calculated, using Equation 3, by inverting the Planck function, shown in Equation (11), after it is obtained by dividing the

observed radiance by the atmospheric transmission, shown in Equation (3). Atmospheric transmission is taken from the curves shown in Figure 27 using a priori knowledge of total water vapor, e.g. from conventional weather data or a numerical forecast model. The thermal emission in the $3.7\text{ }\mu\text{m}$ band is then calculated using the Planck function for the skin temperature of each pixel and attenuated to space. The calculated radiance in the $3.7\text{ }\mu\text{m}$ band is subtracted from the measured radiance in the $3.7\text{ }\mu\text{m}$ band, leaving a useful approximation to the reflected solar energy component in the $3.7\text{ }\mu\text{m}$ band. This energy is converted to albedo by dividing by the fractional solar radiance at the top of the atmosphere for each pixel, as shown in Equations (15) and (16). The resultant albedos or reflectances values have been called the "derived" Channel 3a image. (The derived $3.7\text{ }\mu\text{m}$ albedo image should not to be confused with the $1.6\text{ }\mu\text{m}$ band designed as Channel 3A in the TIROS series satellites.)

While the procedure used to separate the thermal and solar components of $3.7\text{ }\mu\text{m}$ radiation provides only an estimate of the albedo in each pixel, the derived $3.7\text{ }\mu\text{m}$ albedo channel has proven adequate for creating manual and automated snow masks in complex scenes. (Inaccuracies in knowledge of cloud top temperatures, especially of thin cirrus clouds, and the assumption that surface emissivity does not vary between the two bands makes this a gross correction.) The reason only an estimate of the actual solar component is valuable can be seen by examining Figure 11 and Figure 12 which show the reflectivity of snow in the $3.7\text{ }\mu\text{m}$ region is actually smaller than in the $1.61\text{ }\mu\text{m}$ channel. Figure 12 shows that the reflectance of snow in the $3.7\text{ }\mu\text{m}$ band is extremely small, especially when compared to the $0.64\text{ }\mu\text{m}$ band for example, which means that an approximate measure of the $3.7\text{ }\mu\text{m}$ albedo can be useful for identifying surfaces that are snow-covered.

Figure 31 shows the 3.7 μm imagery and derive 3.7 μm albedo component of the scene contained in Figure 30. Notice that in the “albedo” image, snow covered regions of the Sierra Nevada mountains are dark, indicative of very low reflectance values. Also note that the long, narrow stratus cloud in the San Joaquin Valley of California has been changed from dark in the 3.7 μm image, which indicates a warm cloud, to bright in the derived albedo image, indicating high reflectivity. Finally, notice that the thin cirrus clouds present over much of the image in the 12.0 μm band, shown in Figure 30, are more visible in the albedo image shown in Figure 31. Thin cirrus is more pronounced in the 3.7 μm albedo image because it is essentially a 3.7 μm minus 12.0 μm brightness temperature difference field, which is known to enhance the signature of cirrus clouds. Thus, the derived 3.7 μm imagery is useful for snow detection and cirrus cloud classification.

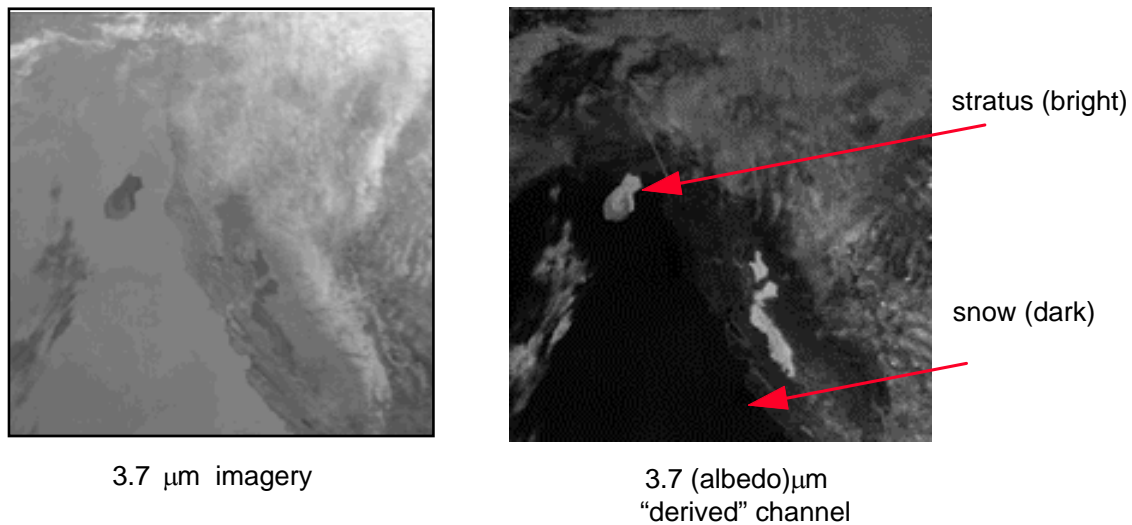
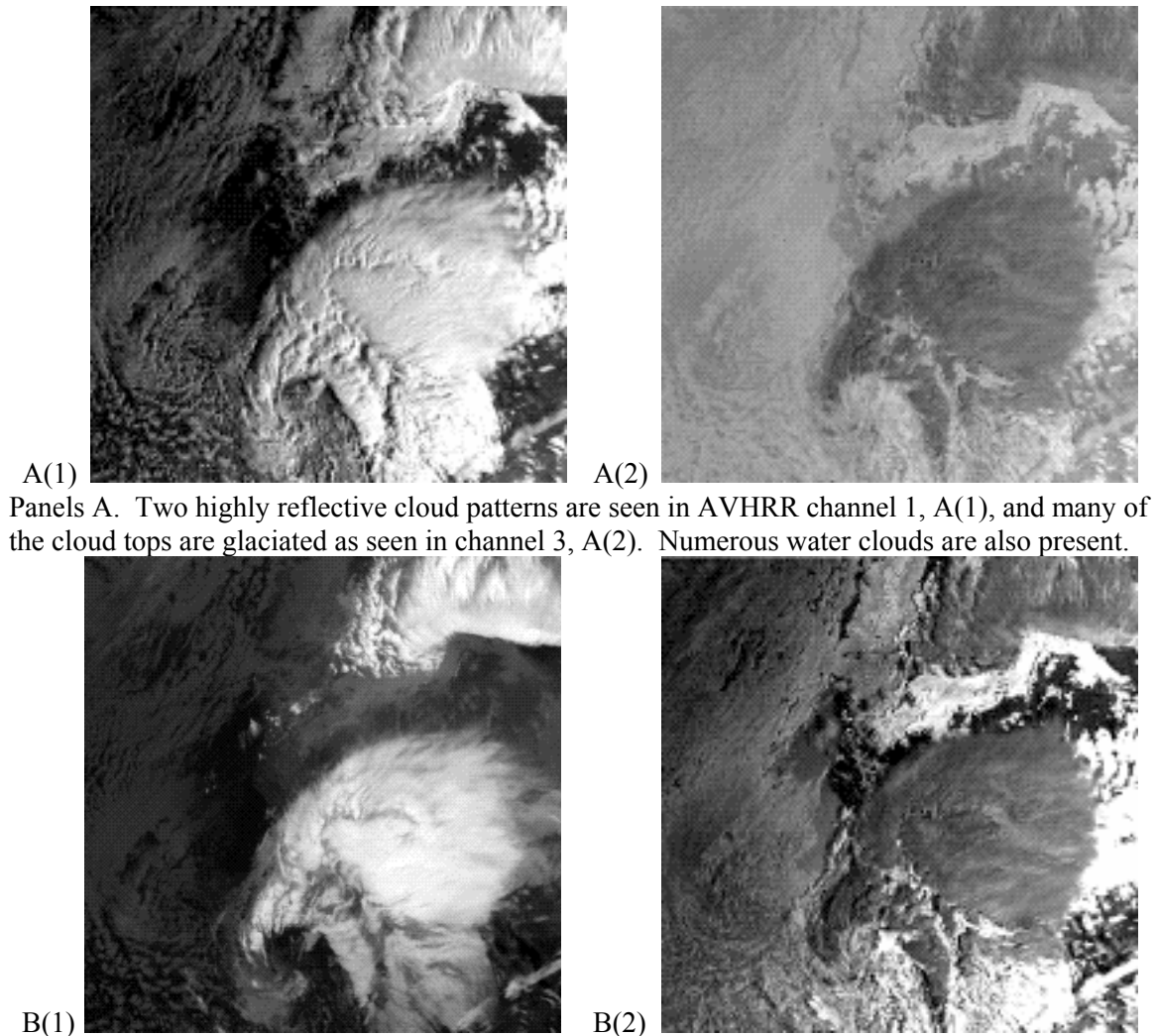


Figure 31. NOAA-12 scene collected at about 7:05 AM local PST (1505 GMT) on March 19, 1996 over western United States and Pacific coastal regions (Hutchison and Locke, 1997).

5.2.4.2.4 Application of 3.7 μm Imagery for Cloud Top Phase Classifications

As previously seen, the derived Channel 3a imagery provides valuable information for the discrimination of clouds and snow covered surfaces. In addition, these data are useful for the determination of cloud top phase, since thin cirrus in the albedo component of this band are enhanced while water clouds signatures are not. However, care must be taken when attempting to determine cloud top phase due to ambiguities in the spectral signature of ice clouds.

Examples of ambiguities in cloud phase are seen in Figure 32. Panels A(1), A(2), B(1), and B(2) contain daytime AVHRR Channels 1, 3, 5, and derived Channel 3a respectively and show two large areas of highly reflective, cold clouds surrounded by lower-level clouds in a NOAA-12 scene collected at 7:58 AM (1558 GMT) on March 12, 1996. The location of these data are the same as those in the previous section.



Panels B. The coldest clouds approach -55°C in channel 5, B(1), and appear very dark in the derived channel 3a, B(2) while thin cirrus clouds in the lower right corner appear much brighter in channels 3 and 3a.

Figure 32. NOAA-12 scene collected at about 7:58 AM local (1558 GMT) on March 12, 1996 over western United States and Pacific coastal regions (Hutchison et al., 1997)

Data in both Channel 3 and derived Channel 3a images show a large, comma-shaped system that has glaciated tops evidenced by very dark signatures in Channel 3 and Channel 4 with temperatures as cold as -53°C . (Water droplets become glaciated in a vacuum at -40°C according to the Theory of Homogeneous Nucleation. Water droplets may freeze at warmer temperatures due to nucleation particles in the atmosphere but all droplets become ice at temperatures of -40°C or less.) Many cloud elements surrounding the comma-shaped cloud pattern appear to be water clouds (bright in Channel 3 and much warmer in Channel 4).

The spectral signatures of ice clouds can be ambiguous when both thick and thin cirrus appear in the same scene. This is illustrated in Figure 33 which is a magnification of the lower-right corner of Channel 5, shown in C(1), and the derived Channel 3a, in C(2) of Figure 32. Glaciated cloud tops are present at point (a) where the Channel 3a signatures appear black. However, clouds in the vicinity of (b) appear bright in Channel 3a suggesting the possibility that their tops are composed of liquid water. Upon examining the shadows these clouds cast onto the adjacent high, cold clouds, seen in Channel 1 at panel A(1), it becomes apparent that these clouds are actually high clouds, i.e. thin cirrus. Thus, the cloud top phase of pixels between points (a) and (b) is ambiguous, since cloud emissivity transitions from large to small values as indicated by the Channel 3a signature changing from dark to light.

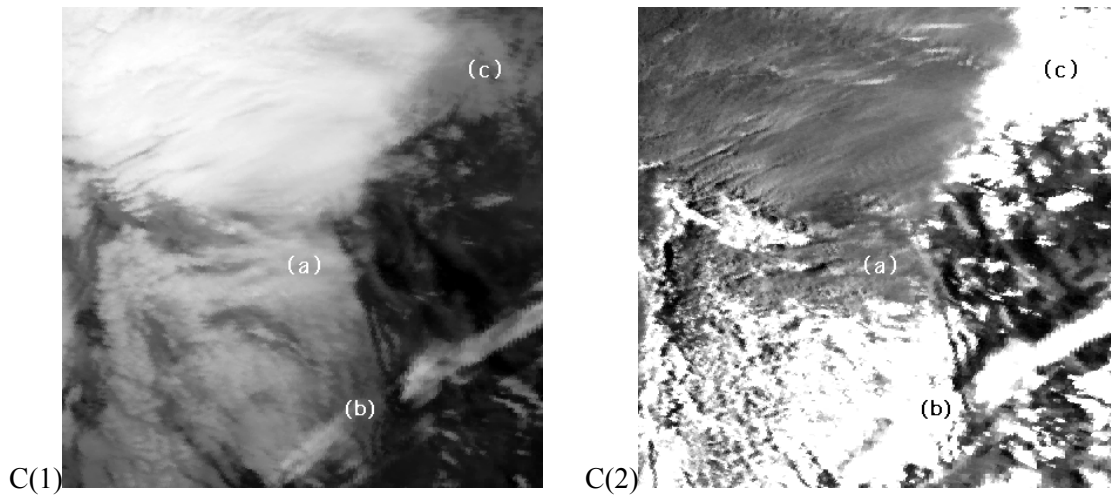


Figure 33. Ambiguities in spectral signatures can impact a-priori cloud top phase analyses of this NOAA-12 AVHRR scene collected at 1558 GMT on March 12, 1996. Zooming in on the lower-right quadrant of channel 5, C(1), and channel 3a, C(2), shows the difficulty in manually classifying cirrus since ice appearance changes as optical thickness decreases from (a) to (b) (Hutchison et al, 1997).

Ambiguity is also seen in cloud signatures along the right side of the scene in the brightest part of Channel 3a, shown at point (c) in panel C(2). With the sun near the horizon, energy reflected off of water clouds overwhelms the normal poorly reflective signature of the ice in Channels 3 and 3a, which makes the cirrus transparent in these data. In addition, the signature of these very thin cirrus clouds over the lower-level water clouds is not distinct in Channel 5, at point (c) in panel C(1). Thus, it is difficult to precisely determine the edge of the thin cirrus shield in any of these AVHRR bands.

Theoretical calculations demonstrate the reason for the variations observed in the $3.7\text{ }\mu\text{m}$ albedo channel for ice clouds. Figure 34a shows simulated nighttime $3.7\text{ }\mu\text{m}$ minus $12.0\text{ }\mu\text{m}$ brightness temperature differences (BTD) for cirrus clouds having a temperature of 236 K , versus optical thickness for ice particles of different sizes in a mid-latitude summer atmosphere. (Recall that the $3.7\text{ }\mu\text{m}$ albedo signature is in fact identical to the BTD35 field.) The results show that the BTD35 feature approaches a maximum of about 20 K at a small optical thickness of about unity. However, the BTD field changes dramatically as optical depth increase or decreases. Cirrus optical depths generally fall within the $0.05 - 10$ range. Figure 34b shows results from additional nighttime simulations of the BTD35 feature versus Channel 4 brightness temperature for a cirrus cloud with a 10 km base and variable Channel 3 emissivities (thickness') in a sub-Arctic winter atmosphere. These data show that the BTD35 feature remains rather large even in a relatively cold, dry atmosphere. Both panels confirm that the BTD35 feature starts small but increases as the emissivity or optical thickness of the thin cirrus cloud increases then drops rapidly as the cloud becomes more optically thick and its radiative characteristics approach that of a blackbody. Thus, it is this thermal signature feature against the poorly reflective snow background that makes the presence of the very thin cirrus clouds readily detectable in the Channel 3a image but it is the potential for large variations in the BDT field that can make the classification of cirrus clouds difficult.

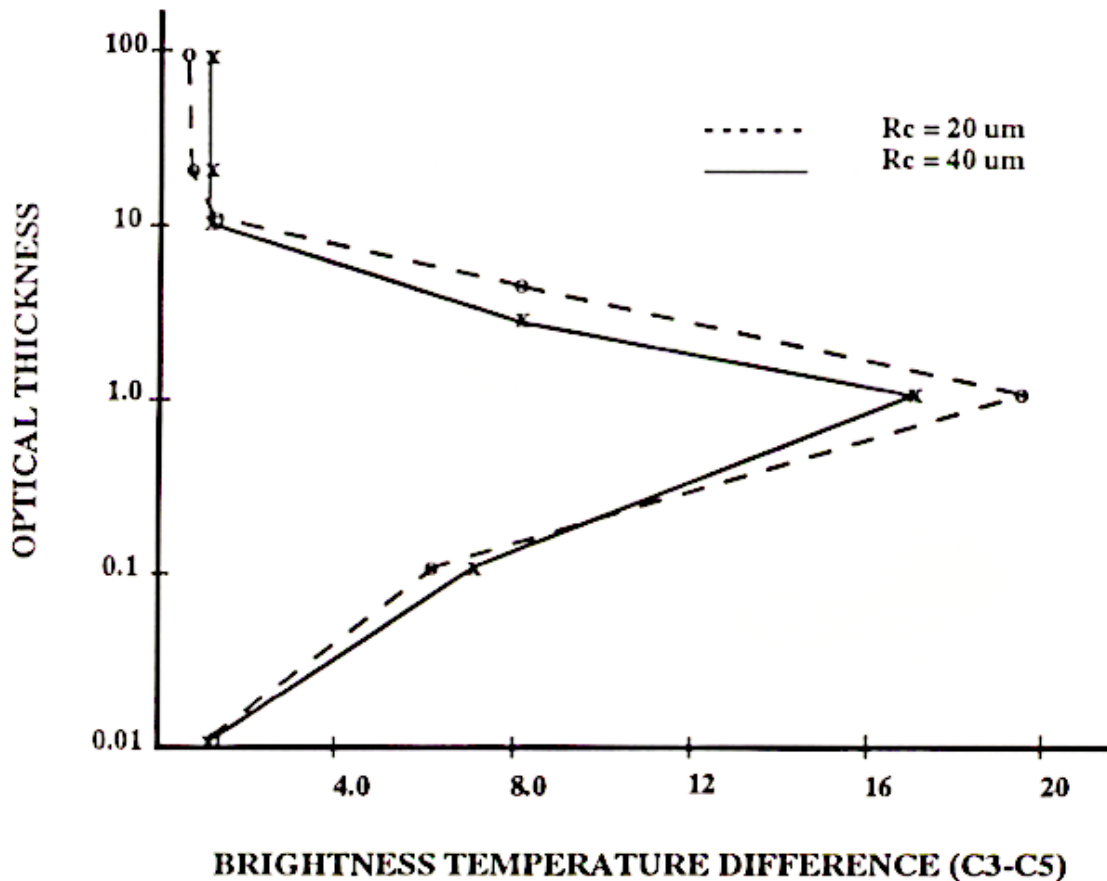


Figure 34a. Simulated AVHRR (ch3-ch5) brightness temperature difference versus optical thickness of cirrus in mid-latitude winter atmosphere with cloud temperature of 236 K and radii of 20 and 40 microns (Hutchison et al., 1997).

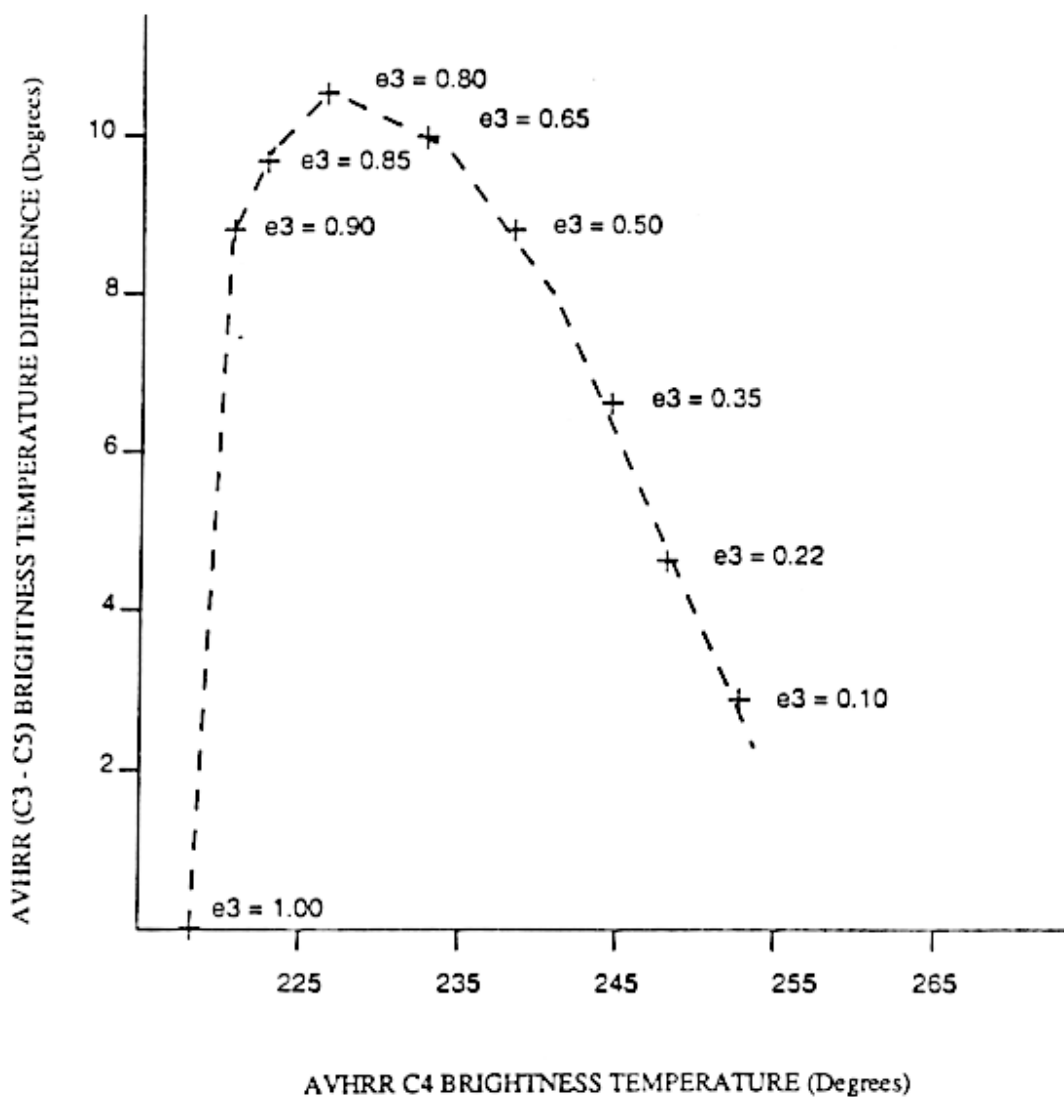


Figure 34b. Simulated AVHRR (Channel 3 minus Channel 5) brightness temperature difference versus Channel 4 temperature for cirrus of variable emissivity at 10 km in sub-arctic winter atmosphere (Hutchison et al., 1997).

5.2.4.2.5 Forest Fires

Forest fires burn at great intensity with temperatures in the 500-1000K range which means their wavelength of maximum emission occurs in the 3-5 μm region as shown in Figure 18. Therefore, these fires are readily observed in the 3.7 μm spectral bandpass. Figure 35 and 36 contain several examples of forest fires in NOAA-12 imagery collected at 2319 GMT on May 11, 2000.

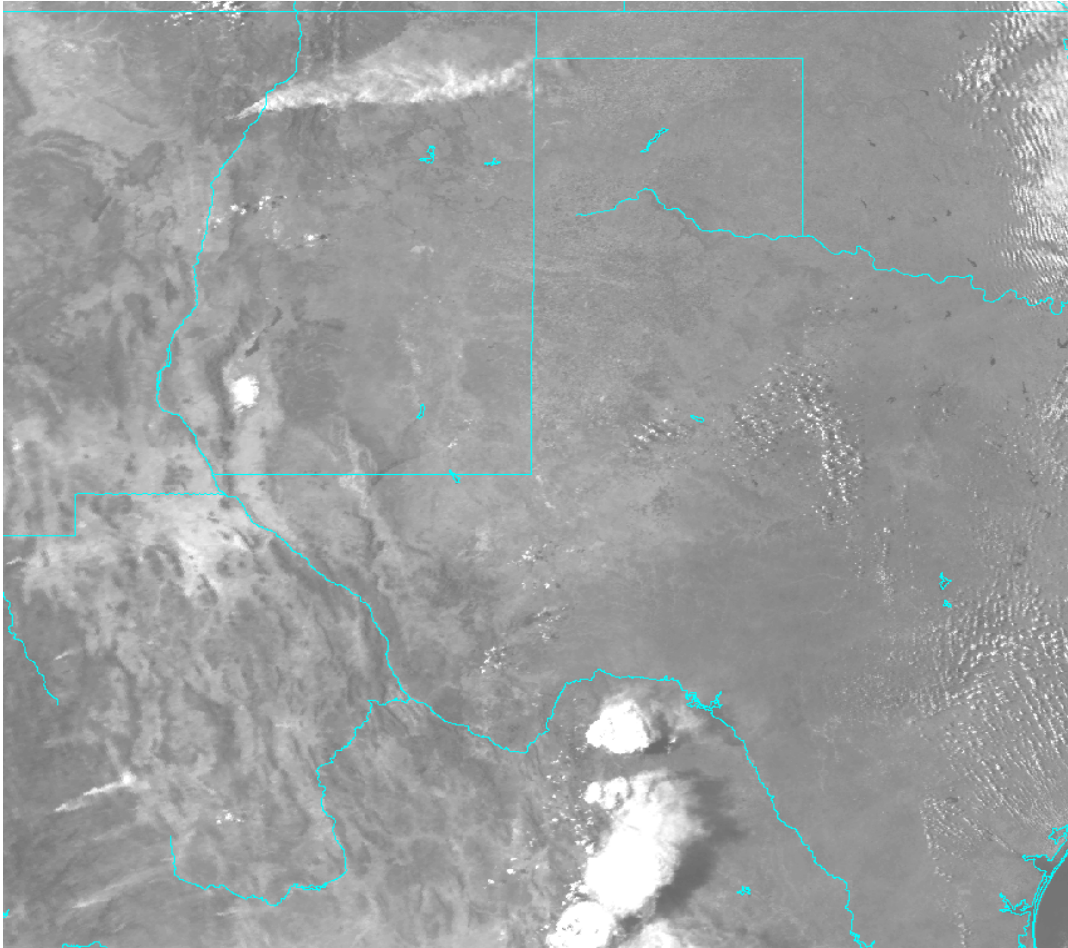


Figure 35. Plumes from several forest fires (including the one near Los Alamos, New Mexico) are evident in Channel 2 of the NOAA-12 AVHRR scene collected at 2319 GMT on May 11, 2000.

Most evident in Figure 35 are the thunderstorms just south of the Rio Grande River near Big Bend National Park in Texas. Next, a large plume of smoke is seen originating from an apparent point source near Los Alamos, New Mexico. The US news services carried extensive coverage of this fire since it was intentionally set by the US Forestry Service to clear brush as a means of reducing the risk of fires during a particularly dry period in the southwestern US due to several years of drought conditions. Less obvious are several plumes in the mountains of Mexico, seen in the lower-left corner of the scene.

The 3.7 μm channel is particularly valuable for detecting “hot spots”, that appear black in Figure 36, in the early stages of the forest fire evolutionary cycle. In particular, these data can be used to identify potential forest fires before they become sufficiently large to generate a smoke plume that is visible in the shorter wavelength bands, as shown above in Figure 35.

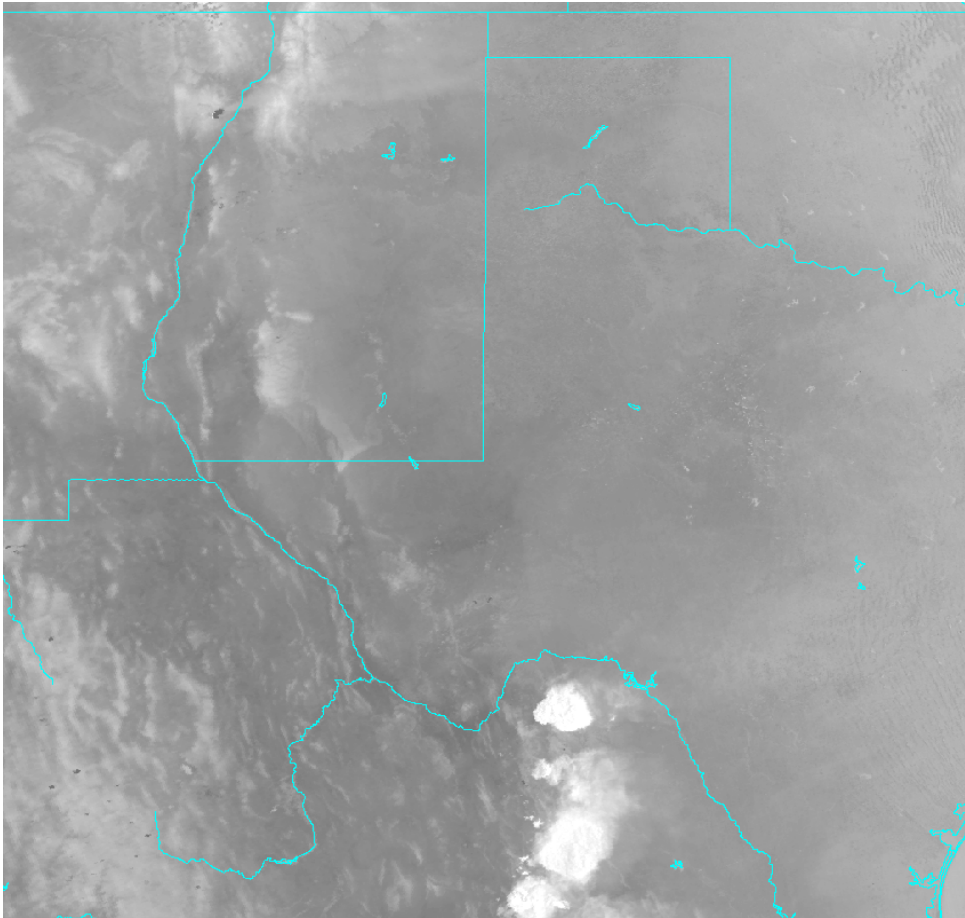


Figure 36. Hot spots in the forest fires are evident in Channel 3 of the NOAA-12 AVHRR scene collected at 2319 GMT on May 11, 2000. Several in the mountains of Mexico show no plumes.

The hot spot associated with the fire near Los Alamos, New Mexico is clearly visible as a large black spot in the 3.7 μm imagery shown in Figure 36. In addition, 4-5 smaller hot spots can be seen in the mountains of Mexico and upon careful inspection, two other black spots are seen north and west of the most northern thunderstorm. These two hot spots are associated with a forest fire that burned for several days in the Glass Mountains of West Texas. While the Cerro Grande fire at Los Alamos received national attention, the Cook Ranch fires went unnoticed by most. However, this particular fire ultimately scorched more than 47,000 acres of timber and came dangerously close to natural gas wells near Odessa, Texas. More insight into the value of 3.7-micron imagery for detecting forest fires is found in the VIIRS Active Fires ATBD [Y3252].

5.2.5. VIIRS I5 Band ($11.45 \pm 0.95 \mu\text{m}$)

5.2.5.1. Theoretical Basis for Band Interpretation

The VIIRS I5 Imagery Channel has a heritage in both the AVHRR Channel 4 and Channel 5 infrared bands. It has a broad bandpass that contains the combined information of the M15 and M16 moderate resolution bands but at the VIIRS Imagery resolution of 371 m at nadir. For those more familiar with DMSP, the VIIRS I5 imagery could be considered very similar to an enhanced DMSP OLS thermal fine (TF) band. The main difference between VIIRS I5 and DMSP OLS/TF data is that the VIIRS data are highly calibrated and radiometrically accurate while OLS/TF data are not well calibrated, e.g. more typical of infrared photographs. Additionally, VIIRS M15 and M16 bands are very similar to AVHRR Channels 4 and 5. Spectral signatures in these bands are shown in Figure 37.

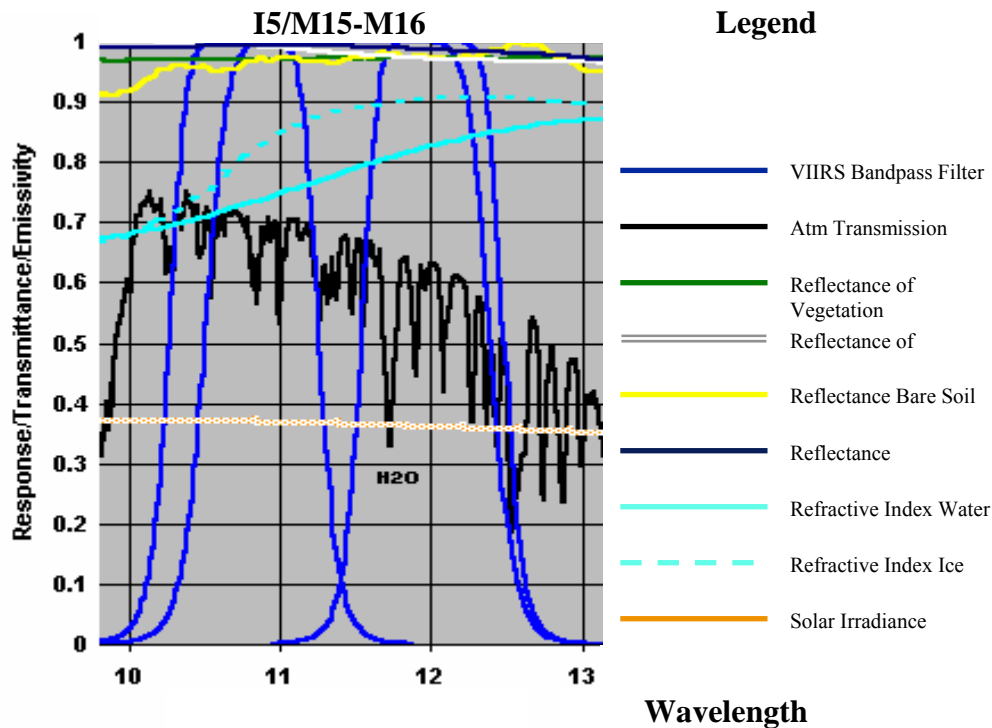


Figure 37. Spectral signatures in VIIRS I5 imagery, M15 and M16 moderate resolution bands.

While the I5 channel is useful for manual detection of cloud with temperature much colder than the radiating surface, such as cirrus, it is also critical for the manual analysis of the 18 cloud types defined in Section 2.4. Many of the requirements for manually-generated cloud types are based simply upon cloud height, e.g. stratus versus altostratus, stratocumulus versus altocumulus. A deficiency is that actual cloud type classifications were created from surface observations that reference the altitude of cloud bases, while satellite observations reference cloud top heights.

Therefore, a primary goal of manual cloud typing is to accurately identify the cloud top height for the QC Bogus process described in Section 2.5.2. The VIIRS I5 band is unique for this task since the emissivity of water droplets, bare soil, and vegetated soil are more close to unity in the VIIRS I5 band, as seen in Figure 37, than any other channel. Since emissivity is nearly unity for many features, brightness temperature can be readily correlated with skin temperature after correcting for atmospheric attenuation due to water vapor concentration along the line-of-sight between the feature and the VIIRS sensor. (Cirrus clouds are the exception since the emissivity of cirrus continues to be highly variable in this and all VIIRS bands.) As shown in Figures 37 above and Figure 27, atmospheric transmittance in the I5 Imagery Band is reduced substantially by water vapor absorption. Water vapor above the cloud top absorbs some of the energy emitted by the cloud and re-radiates energy at a colder temperature, due to the lapse rate in the atmosphere, e.g. temperature generally decreases with increases in altitude throughout the troposphere. Thus, the VIIRS sensor receives less energy from a cloud in a humid atmosphere than it would from a cloud in a drier atmosphere. If uncorrected, the effect of this atmospheric attenuation would result in the cloud top height being estimated higher than its actual location in the atmosphere.

Attenuation of energy by atmospheric water vapor in the I5 Imagery Band is relatively small for dry atmospheric conditions so that brightness temperatures are usually only about 1-2 degrees C colder than actual cloud top temperatures. In more humid conditions, brightness temperatures may be 3-6 degrees C colder than actual cloud top temperatures. Assuming a pseudo-adiabatic lapse rate of $\sim 6^{\circ}\text{C}/\text{km}$, estimates of cloud top heights would be in error by at most about 500–1000 m if no correction is made for atmospheric water vapor. With corrections, these errors should be no more than several hundred meters for water clouds. Cloud top temperatures from the VIIRS I5 band, used in conjunction with atmospheric profile information from another NPOESS sensor or NWP products, readily support the classification of both low and mid-level water clouds and differences between them. Differentiation between classes within these groups, e.g. stratiform and cumuliform, is based upon cloud texture and is best done with the added use of visible imagery.

Alternatively, it is possible to differentiate between cloud top heights (low versus middle for example) by examining differences in brightness temperatures between each cloud top. For example, assuming the brightness temperature differences between two groups is 18 degrees C, the difference in cloud tops between these clouds would be approximately 3 km again assuming a pseudo-adiabatic lapse rate. Using the same technique, the height of the cloud could be compared to the cloud-free surrounding surface to estimate cloud top height above the ground since the emissivity of many surfaces is unity in the I5 band. Even this simplistic methodology supports the manual classification of water cloud types.

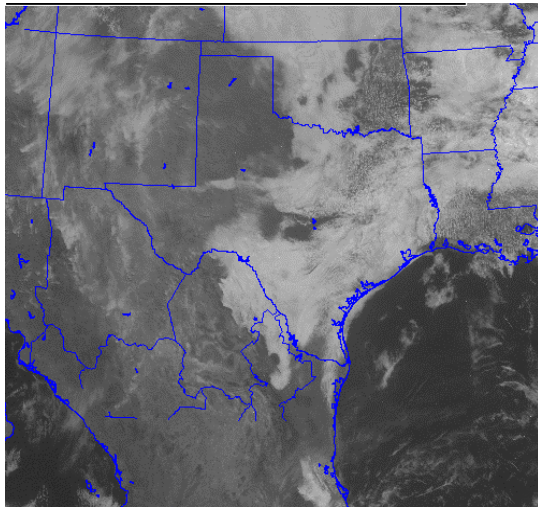
While cirrus clouds are readily detected and manually typed in the VIIRS I5 band, it becomes more of a challenge to manually identify the altitude of these clouds. Cirrus clouds can vary in altitude greatly depending upon where they occur across the globe. Since they are generally present near the tropopause, they may be found at very low

altitudes in the high latitude regions or at much higher altitudes in the mid-latitude regions and the tropics. If precise information is needed on cirrus cloud top height, it may not be possible to obtain with the simplistic method described above. Most cirrus clouds are optically-thin which means these clouds normally allow some energy emitted from lower-levels of the atmosphere to pass unattenuated to space, unlike water clouds that are near blackbodies in this part of the spectrum. In other words, the emissivity of cirrus is highly variable as shown in Section 5.2.4.2.4. Some energy emitted at lower levels passes unattenuated through cirrus clouds which can result in VIIRS I5 brightness temperatures being as much as 30 degrees C warmer than the actual cloud top temperatures. Techniques similar to those used to estimate water cloud tops could easily be in error by 5 km or more if used to analyze the tops of optically-thin cirrus clouds. Thus, if accurate cloud top heights of cirrus clouds are needed, they should be taken from the VIIRS automated Cloud Top Height EDR which uses a multi-channel retrieval algorithm to simultaneously retrieve cloud top height, emissivity, and cloud top temperature. There is no VIIRS manually-generated cloud top height EDR and the information content in the VIIRS I5 band does generally support the differentiation between ice clouds and water clouds, especially with additional information on textural.

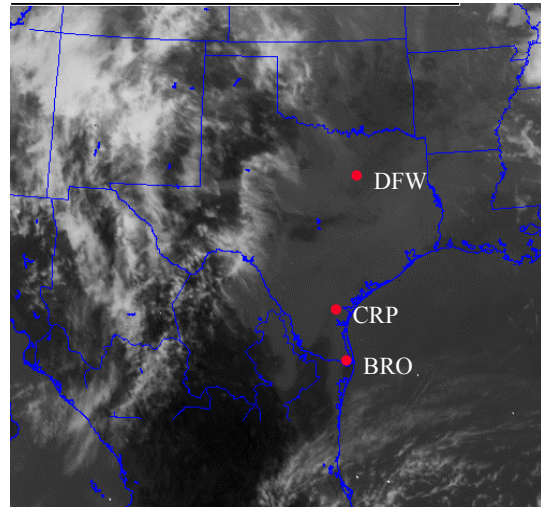
Therefore, most clouds listed in Section 2.4 can be manually classified with VIIRS imagery resolution bands 1-5, with several exceptions. First, nimbostratus cannot be classified from imagery alone since the presence of rain distinguishes this cloud from other clouds such as altostratus. Use of ancillary data, e.g. rain mask from microwave imagery could support the distinction between these cloud types. Also, altocumulus constellatus may be difficult to identify since the distinguishing feature of these clouds is typically of a scale much smaller than VIIRS imagery, which has 371 m horizontal spatial resolution.

5.2.5.2. Representative Imagery of the VIIRS I5 Band ($11.45 \pm 0.95 \mu\text{m}$)

Attention now turns to a demonstration on the use of the imagery in the $12.0 \mu\text{m}$ band for cloud detection and cloud typing. Figure 38 contains daytime visible and IR imagery of clouds over Texas on April 4th at 1600 GMT. Extensive areas of water clouds are seen over the eastern half of Texas in the visible imagery while a large amount of cirrus is seen over the western half of the state in the IR imagery. The fact that these cirrus clouds are not readily seen in the visible data demonstrates that they are optically-thin clouds.



GOES-E Visible Imagery 4/4/01, 1600 GMT



GOES-E Infrared Imagery 4/4/01, 1600 GMT

Figure 38. GOES-East visible and IR imagery of Texas on April 4, 2001 at 1600 GMT show extensive water clouds over the eastern and thin cirrus clouds over western Texas.

In an attempt to determine cloud top temperatures that are needed to define cloud types, additional images of this area are analyzed along with coincident radiosonde observations valid at 1200 GMT earlier in the morning. The coincident NOAA-14 AVHRR Channel 4 imagery shown in Figure 39 has a data time of 1127 GMT on April 4th along with brightness temperatures of various cloud tops associated with radiosonde stations. Figure 40 shows the radiosonde observation and thermodynamic plot of these data for Corpus Christi (CRP), TX.

The radiosonde observation for Corpus Christi shows a rapid decrease in the humidity and simultaneous increase in temperature that marks the cloud top height. From the mandatory and significant levels of data reported in the radiosonde, it is possible to accurately identify the cloud top height and cloud top temperature. In this case, the radiosonde observation reveals the cloud top temperature is 19.6°C and the cloud top height is 615 meters.

An examination of the NOAA-14 12.0 μm IR imagery collected at 1127 GMT shows the clouds over Corpus Christi have a brightness temperature of 19.3 C which is just 0.3 C colder than the temperature measured by the radiosonde. This relatively small difference is due to the absorption of energy by water vapor above the cloud and re-emissions by these gases at a colder temperature. In this case, the atmosphere is relatively dry - if more water vapor were present in the atmosphere, the Channel 4 brightness temperature would be colder and this difference larger. Several small cloud-free regions over the ocean have brightness temperatures of 21.5 C. Thus, from the 12.0 μm satellite imagery alone, the manually-generated cloud top height is estimated to be $(21.5-19.3)/(6\text{C}/1\text{Km}) = 367$ meters. The error in cloud top height is slightly greater than 200 m. Based upon the cloud's texture and altitude, it is classified as a stratus cloud.

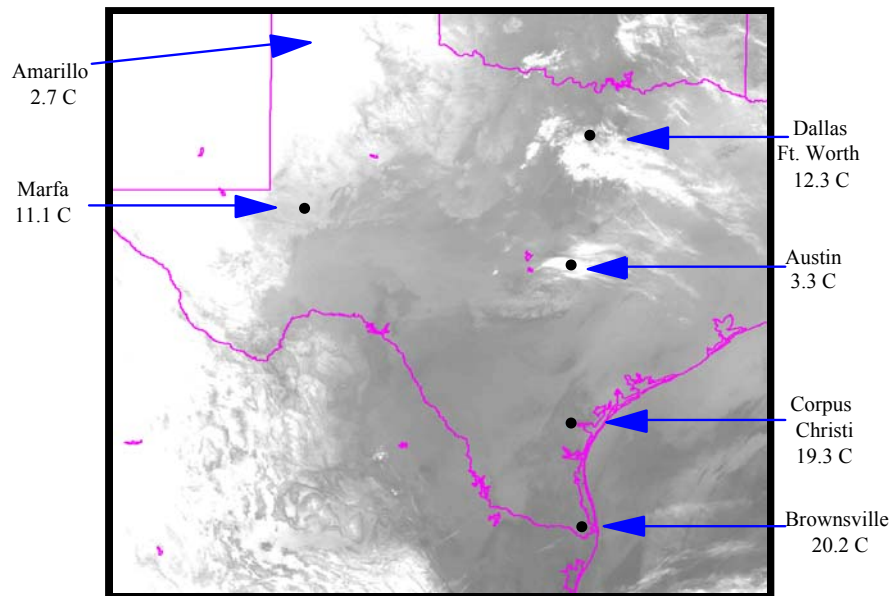


Figure 39. Brightness temperatures in AVHRR Channel 4 imagery of various clouds located over Texas at 1127 GMT on April 4, 2001.

1	12924	72251	27.77	-97.50	14	1103
2	200	1741	500	74	7	3
3		CRP		99999	kt	
9	10100	14	216	204	130	7
4	10000	102	218	207	140	10
6	9767	304	99999	99999	170	18
6	9427	609	99999	99999	185	23
5	9420	615	196	183	99999	99999
4	9250	778	204	171	185	27
6	9105	914	99999	99999	185	29
5	8940	1071	212	152	99999	99999
6	8788	1219	99999	99999	190	30
5	8780	1227	226	96	99999	99999
4	8500	1512	214	44	200	24
6	8193	1828	99999	99999	200	21
5	7930	2108	208	-22	99999	99999

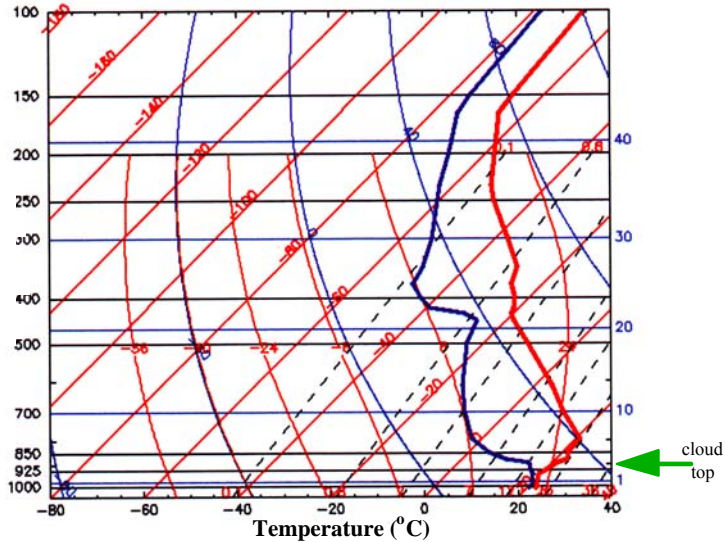


Figure 40. Radiosonde for Corpus Christi, Texas at 1200 UTC on April 4, 2001 along with thermodynamic (SkewT-LogP) chart of these data show cloud top temperature of 19.6C.

This simplistic approach for the manual classification of cloud and estimation of cloud top height does not work well in the presence of optically-thin cirrus. While it is apparent that cirrus clouds extend over the Dallas/Ft.Worth (DFW) region, it is difficult to estimate the height of these clouds from 12.0 μm imagery. For example, the brightness temperature in Figure 39 for Dallas/Ft.Worth is 12.3 C. A correlation of this height to the DFW radiosonde would suggest cloud top heights of 740 mb which is approximately 8,000 feet for this atmosphere. Clearly these clouds are much higher - probably 25,000 feet or more. Unfortunately, it is often not possible to detect cirrus clouds in radiosonde observations. Thus, 12.0 μm imagery cannot be used to estimate cloud top heights of optically-thin cirrus clouds because these clouds allow lower-level energy to pass unattenuated to space so cloud top temperatures appear much warmer than they are, which causes cloud top heights to be placed too low in the atmosphere using only the VIIRS I5 Imagery band.

5.2.6. VIIRS Day Night Band (DNB)

5.2.6.1. Theoretical Basis for Band Interpretation

The VIIRS Daytime/Nighttime Visible Imagery band (also called the Day Night Band, or DNB) has a heritage in the DMSP/OLS L channel, and indeed will be the operational successor to the OLS. The main purpose of the band is to provide low light visible imagery at the terminator and for lunar illuminated nighttime scenes. The spectral response of the DNB has been designed to operate efficiently under lunar illumination conditions, as shown in Figure 41.

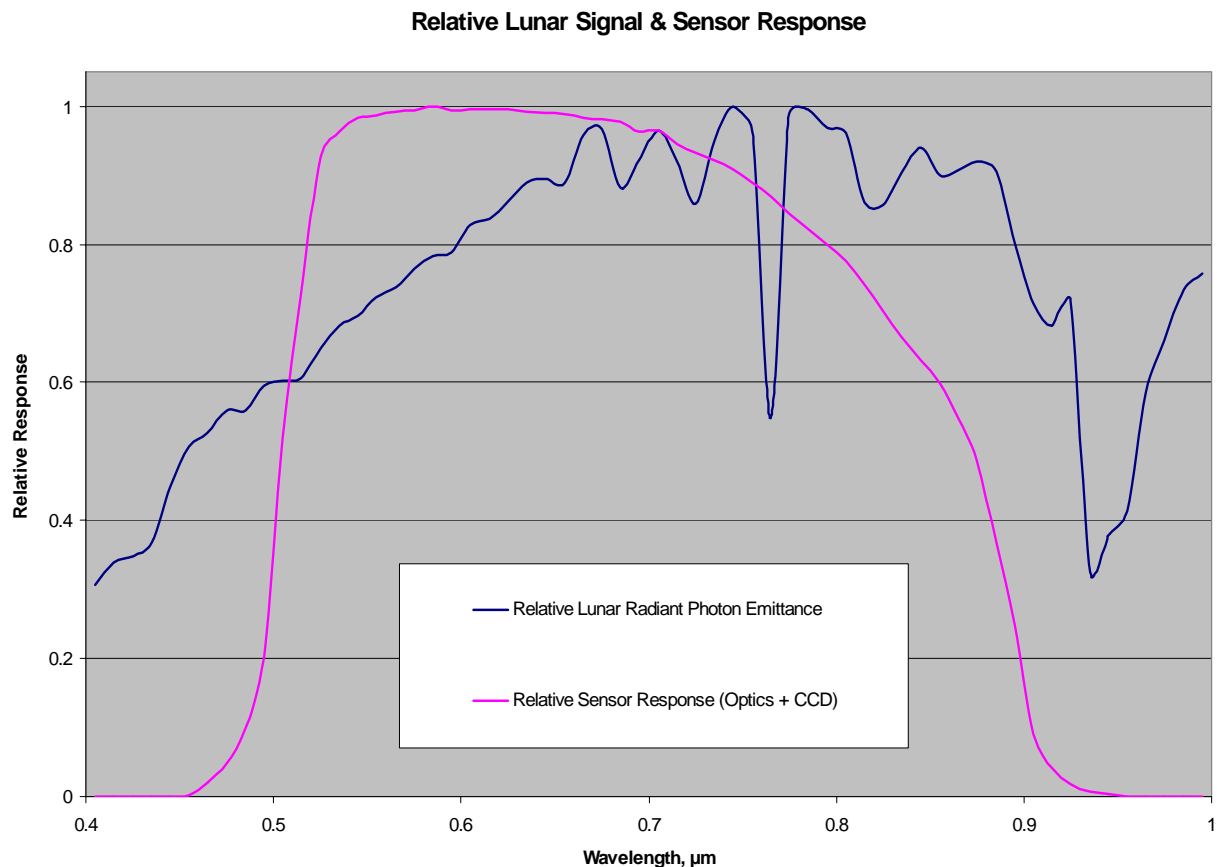


Figure 41. Spectral Response of the Daytime/Nighttime Visible Imagery band, compared with the lunar signal.

The spectral response of the DNB is designed to decline sharply at 0.5 microns, as can be seen in Figure 41. The purpose of the short-wave cut-off is to reduce contamination by atmospheric path radiance, which is more pronounced at shorter wave lengths. The design is compatible with OLS heritage.

The DNB measurement range (c.f. Table 3) will provide useful cloud imagery under quarter moon illumination. SNR performance at night will vary with lunar phase, lunar elevation angle, and scan angle. An example for quarter moon phase is shown in Figure 42.

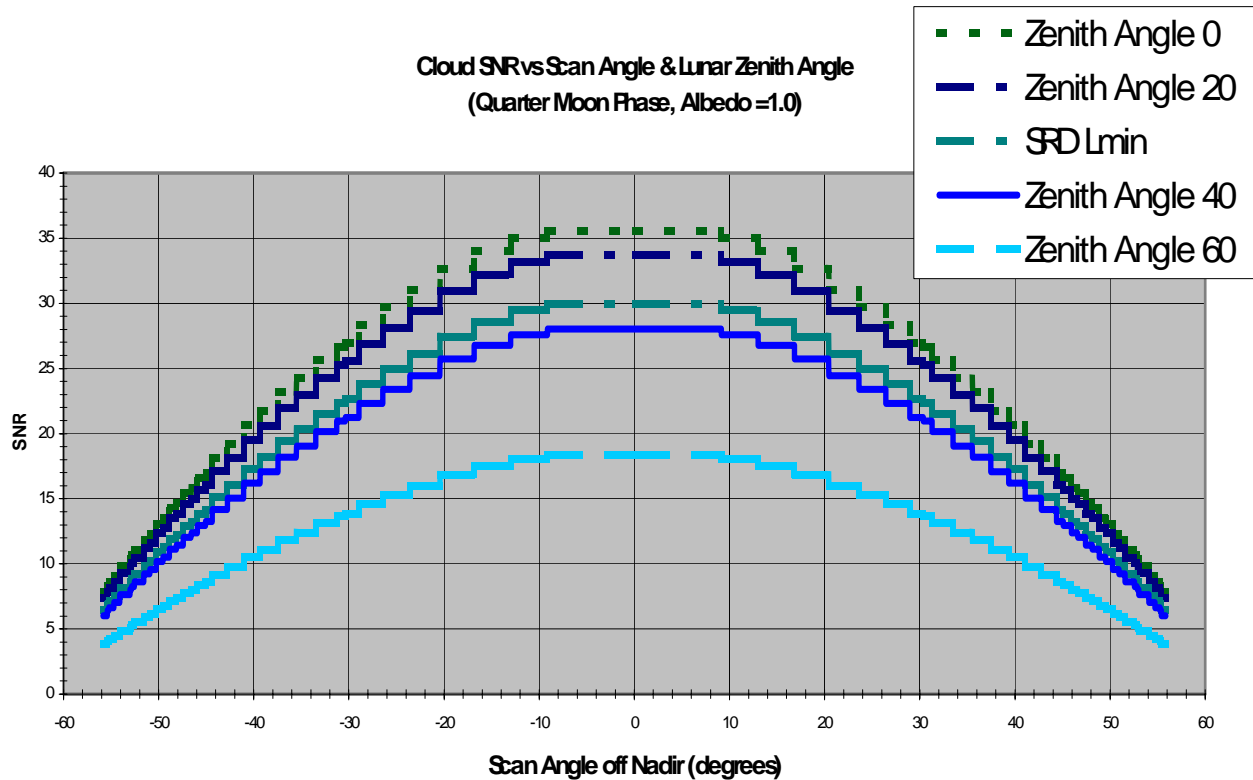


Figure 42. SNR Performance of the Daytime/Nighttime Visible Imagery under quarter-moon illumination conditions, as a function of scan angle.

The top two curves and bottom two curves represent lunar zenith angles of 0, 20, 40, and 60 degrees respectively. The middle curve corresponds to the minimum measurement range of $4\text{E-}9 \text{ W/cm}^2/\text{sr}$. SNR greater than 10 is achieved at the minimum radiance for almost the entire scan. SNR as high as 30 is achieved at the minimum radiance for a nadir view.

The characteristics of DNB imagery are similar to those of the I1 imagery band (Section 5.2.1). Reflectivity from clouds and snow is very high, while vegetated land is noticeably darker, and ocean surfaces are very dark. Manual detection of clouds is based on the reflectivity contrast between clouds and darker surfaces, though snow/cloud discrimination is more challenging. As with the I1 band, manual cloud classification with the VIIRS DNB emphasizes (1) texture, (2) spatial resolution of cloud elements, and (3) shadows which may be cast from clouds high in the atmosphere onto lower level clouds.

5.2.6.2 Representative Imagery of the VIIRS DNB ($0.7 \pm 0.2 \mu\text{m}$)

An example of DNB terminator imagery can be seen in Figure 43.

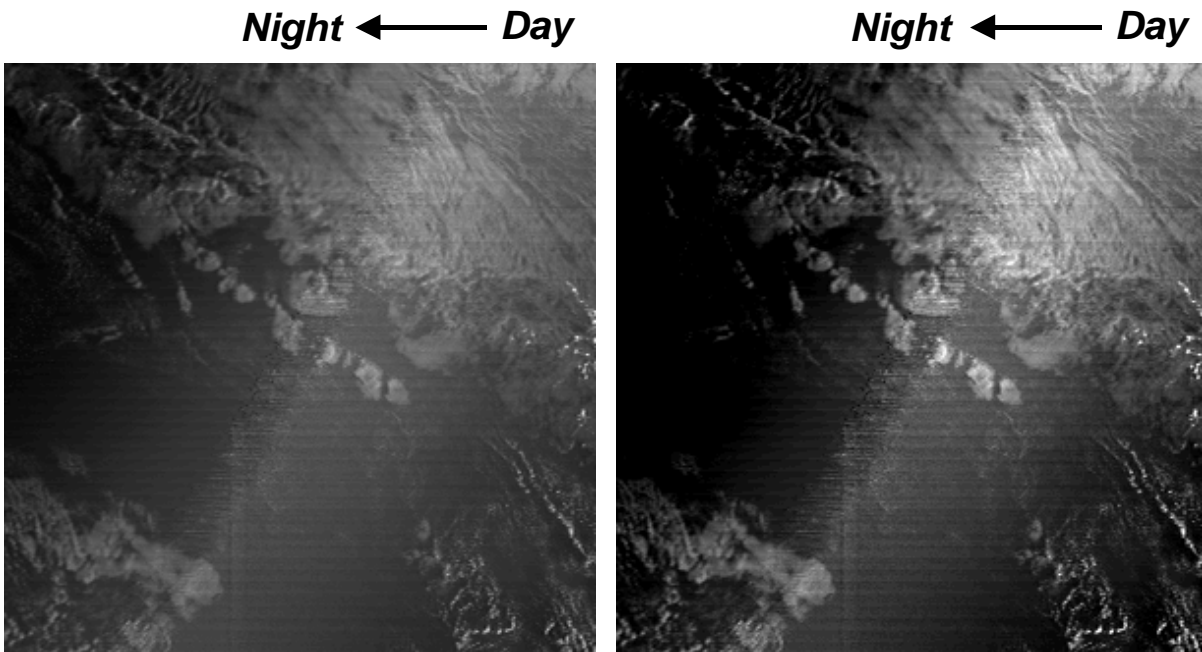


Figure 43 – F13 OLS Visible (HRD) image for the first terminator crossing of the July 20, 2001 1131 UT orbit.

The image in Figure 43 displays 300 scan lines for a scan angle range of $240 - 470^\circ$. The daytime/nighttime sides are indicated. The full dynamic range is displayed in the LEFT image. The RIGHT image is contrast-enhanced to highlight the terminator crossing effects (e.g., path radiance from atmospheric scattering). Figure 43 demonstrates how well the OLS on board gain management algorithm (GMA) works, as the source radiance has a dynamic range over the scene greater than six orders of magnitude. Our baseline algorithm for NCC Imagery is designed to capture the on board OLS GMA within the data processing architecture of the VIIRS Ground Segment. We therefore expect VIIRS DNB performance to be comparable to that of the OLS.

In Figure 43, clouds are bright and the underlying surface is dark, allowing for cloud detection. Cloud classification can be made from the texture and shadowing structure evident in the imagery. The figure also illustrates the difficulty in snow/cloud discrimination with visible band imagery. The bright features in the lower right section of the image are distinguishable as snow, because the section is cloud-free, allowing the analyst to observe the terrain structure of the bright/dark contrast. It is probable that snow is present in the upper left section of the image, but this is more difficult to determine, as the section contains clouds.

5.3. VIIRS IMAGERY ASSIST DATA

Channel characteristics for the VIIRS moderate resolution bands are shown in Table 10 along with band characteristics of existing systems. In some cases, these bands are useful for cloud detection and cloud typing and are referred to as Image Assist (IA) bands. IA Bands are not considered essential to meet NPOESS Threshold requirements for manually-generated cloud data products, although some are useful for pushing toward Objective requirements.

Table 10. Bandpasses of Sensors that Closely Approximate VIIRS Moderate Resolution Bands.

Band	VIIRS Channel	Central Wavelength (μm)	Bandwidth (μm)	Satellite System and Channel	Wavelength Interval
2	M1	0.412	0.02	MODIS 8	.405-.420
3	M2	0.445	0.018	MODIS 9	.438-.448
4	M3	0.488	0.02	MODIS 10	.483-.493
5	M4	0.555	0.02	MODIS 12	.546-.556
7	M5	0.672	0.02	MODIS 13	.662-.672
8	M6	0.746	0.015	MODIS 15	.743-.753
10	M7	0.865	0.039	MODIS 2	.841-.876
11	M8	1.24	0.02	MODIS 5	1.230-1.250
12	M9	1.378	0.015	AVIRIS	1.370-1.380
14	M10	1.61	0.06	MODIS 6	1.628-1.652
15	M11	2.25	0.05	MODIS 7	2.105-2.155
17	M12	3.7	0.18	MODIS 20	3.660-3.840
18	M13	4.05	0.155	MODIS 21	3.929-3.989
18	M13	4.05	0.155	MODIS 22	4.020-4.080
19	M14	8.55	0.3	MODIS 29	8.400-8.700
20	M15	10.763	1	MODIS 32	11.77-12.27
22	M16	12.013	0.95	MODIS 32	11.77-12.27

5.3.1. VIIRS M1 – M4 Bands ($0.412 \pm 0.010 \mu\text{m}$, $0.445 \pm 0.009 \mu\text{m}$, $0.488 \pm 0.010 \mu\text{m}$, $0.555 \pm 0.010 \mu\text{m}$)

5.3.1.1. Theoretical Basis for Band Interpretation

The spectral signatures of the Earth's atmosphere and key surface backgrounds in the VIIRS M1 – M4 bands are shown in Figure 44. The bands are considered here as a set since the signatures shown in the figure change little with each band center. The figure shows the available solar irradiance is large in these bands since the wavelength of maximum emission for the sun with its 6000K blackbody surface temperature is near $0.5 \mu\text{m}$. In addition, it is seen that the reflectivity of snow is very large, at $> 95\%$, while atmospheric transmission is relatively low, averaging about about 50%.

The large attenuation of solar energy is primarily due to Rayleigh (or molecular) scattering while the wings of some ozone absorption lines extend into the shorter wavelengths. Rayleigh scattering results from the interaction of the very short wavelengths of solar radiation with the molecular structure of the atmosphere, consisting primarily of the permanent gases (those with constant mixing ratios) which are oxygen and nitrogen, along with variable constituents (gases with mixing ratios that vary within the vertical) such as water vapor. The reduction in solar illumination due to molecular scattering causes unprocessed M1 data to appear bright and washed out, even over surfaces that have a low (< 10 percent) reflectivity such as bare soil and vegetated land. In fact, Rayleigh scattering has the effect of turning on a uniformly bright light in a scene being photographed. This brightness can be corrected in several ways: (1) the contrast of the entire scene can be reduced at the loss of scene content since all features are uniformly darkened, (2) pixel radiances can be corrected for Rayleigh scattering which is a function of atmospheric path length or sensor scan angle, and (3) composite images can be formed with other bandpasses which do not experience the effects of Rayleigh scattering. The second and third methods tend to preserve the information content of surfaces and allow information to be extracted over desert surfaces.

The VIIRS M1-M4 bands were justified to provide information on the chlorophyll content of the ocean's surface, as previously demonstrated with SeaWiFS and MODIS sensors. The reflectivity of chlorophyll is strong in these VIIRS bands; unfortunately the retrieval of chlorophyll is complicated by the strong reduction in the signal arriving at the spacecraft. Since 90% of chlorophyll's spectral signature is lost by this atmospheric attenuation, both SeaWiFS and MODIS create a Level_2 product called "water leaving radiances" which provides useful estimates of ocean surface radiances. Recall that all other VIIRS data previously examined were referenced against the top of the atmosphere.

The M1 band is very useful for distinguishing between lower-level water clouds and backgrounds in semi-arid regions of the world. At 412 nm, bare soil has a reflectivity of about 5 percent, as shown in Figure 44, while the reflectivity of water clouds and snow are much larger. The reflectivity of bare soil increases constantly across the VIIRS M1 – I2 spectral region and reaches a maximum of about 35 percent at 0.865 μm . Little change is seen in the reflective characteristics of water clouds and snow across the same spectral region. Therefore, the M1 band can be used as an “*Imagery Assist Band*” with VIIRS imagery bands in the manual detection of clouds over arid regions such as the Middle East. If for some reason the M1 band is not available, data from the M2, M3, or M4 band can be used in its stead but with a decreasing level of value since the reflectivity of bare soil increases from about 5 – 15 percent over 0.4 – 0.6 μm range. In addition, the VIIRS M1 band is also useful for the manual detection of volcanic aerosols over semi-arid surfaces. Finally, the water leaving radiance product is considered a useful data set for scene interpretation over the ocean surfaces to examine near-coastal effects.

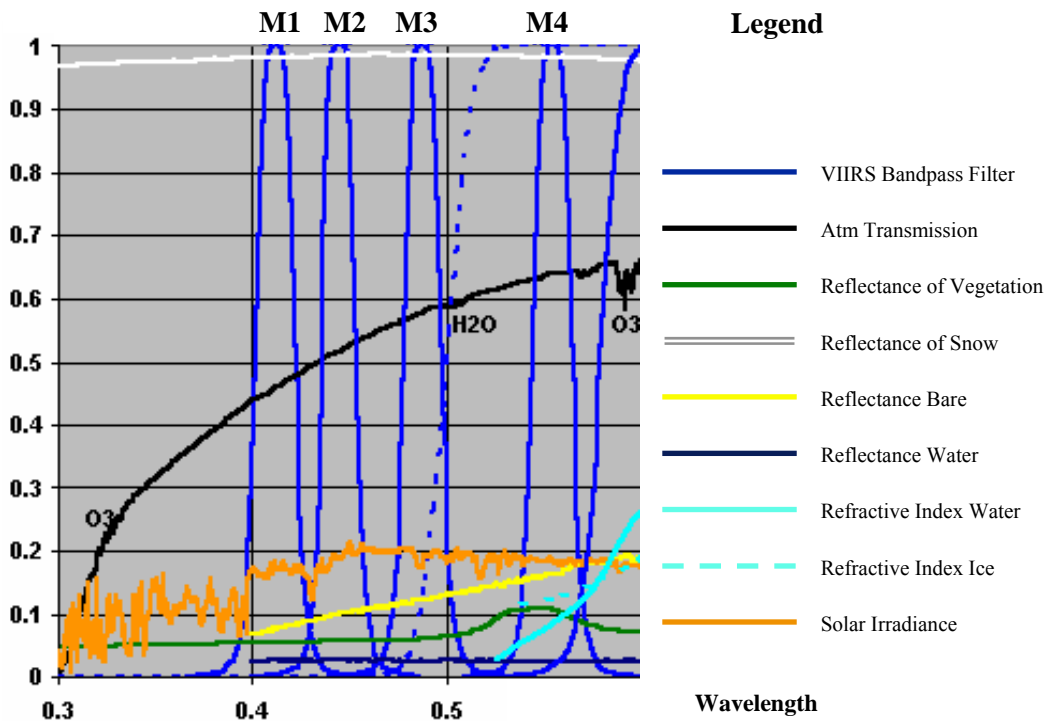


Figure 44. Theoretical calculations of atmospheric and surface properties in the VIIRS M1-M4 bands.

5.3.1.2. Representative Imagery of the VIIRS M1 Band ($0.412 \pm 0.05 \mu\text{m}$)

Figure 45 shows sample M1 and M3 data collected by the SeaWiFS sensor for a scene over the southwestern US at 1954 GMT on July 13, 2001. The scene contains a large layer of stratocumulus in the left-bottom corner, to the left of Baja California. The Altar Desert is located in the middle of the scene, and the Gulf of California at the bottom center of the image. Note that some land features are slightly more evident in the 488 nm, M3 band, in the right panel, than in the 412 nm, M1 band at left. Clouds appear bright and the ocean appears equally dark in both spectral bands.

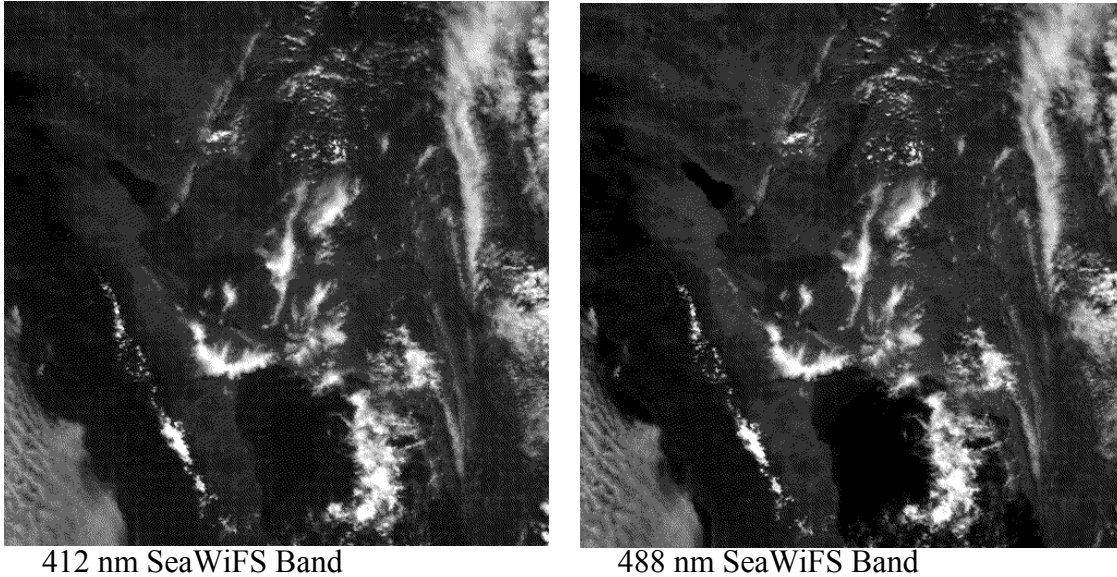


Figure 45. SeaWifs data from the 412 nm and 488 bandpasses are shown for the western US and northern Mexico on July 13, 2001 at 1954 GMT.

For convenience, in Figure 45a, SeaWiFS images of VIIRS M4 and M6 bands are included for the same scene shown in Figure 45. These data contain no additional information that is particularly useful for manual cloud analyses. It is evident, however, that the surface reflectivity of bare soil, which covers much of the scene, increases with wavelength. The contrast between clouds and surface features is least at 765 nm and greatest at 412 nanometers. The 0.845 micron band for this scene was shown earlier in Figure 23. These changes in surface reflectivity properties are exploited in the color composites shown in Chapter 6.

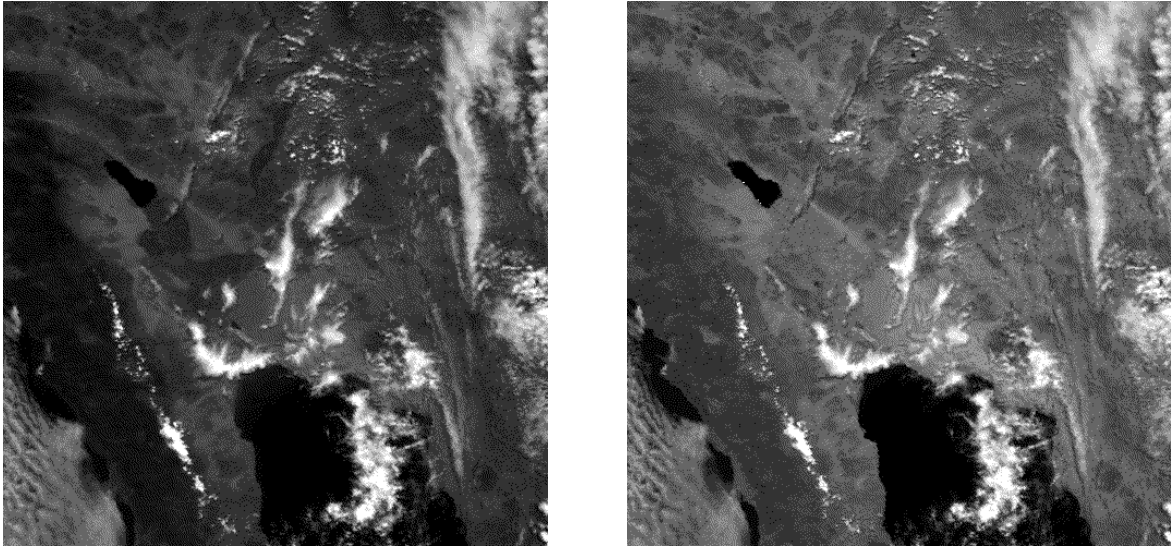


Figure 45a. SeaWiFS data in the 555 nm and 765 nm bands are shown for the scene over the Western US and northern Mexico on July 13, 2001 at 1954 GMT.

5.3.2. VIIRS M9 Band ($1.378 \pm 0.0075 \mu\text{m}$)

5.3.2.1. Theoretical Basis for Band Interpretation

The VIIRS M9 channel has a very narrow bandpass centered on a very strong, but also narrow, water vapor absorption band, as seen in Figure 46. Its primary value for manually-generated cloud analysis is for the detection of thin cirrus clouds, especially over land surfaces, in daytime VIIRS data. Solar irradiance remains large, although it is decreasing with increasing wavelengths. Notice that atmospheric attenuation increases sharply outside the narrow VIIRS M9 band.

Since the concentration of water vapor generally has its maximum in the lower atmosphere and decreases markedly with altitude, incident solar energy in this spectral band is strongly attenuated once prior to reaching the Earth's surface and a second time after being reflected back toward space, under cloud-free atmospheric conditions. Simulations, based upon LOWTRAN (Berk et al., 1989) using a sub-Arctic summer atmospheric profile (Anderson et al., 1986), predict that only 20 percent of the solar energy would arrive at satellite altitude if reflected by a perfect reflector, i.e. 100% albedo or reflectance, located at an altitude of 6 km, as shown in Figure 47. Even less energy will arrive at the VIIRS sensor from reflection off of clouds. This percentage of energy reflected decreases markedly as the perfect reflector is lowered toward the surface. No reflected energy reaches the satellite when the reflector is on a surface at sea level (Gao et al., 1993).

The reflectances of most surfaces are not 100% but generally less than 50% this value as shown in Figure 46. For example, the reflectivities in the VIIRS M9 bandpass of snow, bare soil, and vegetated soil, are all under 50 percent. Thus, these surfaces should not be visible in the M9 band, in effect these surface features are “perfectly black” in this spectral band.

On the other hand, cirrus clouds exist at levels where water vapor concentrations are typically many orders of magnitude less than at the Earth's surface. Therefore, solar energy is scattered from cirrus clouds before it reaches the more humid levels of the atmosphere. Similarly, middle-level water clouds may be seen in M9 data since these clouds reside at altitudes where the water vapor is much less than the surface but they are highly reflective. Lower-level water clouds may or may not be seen in the VIIRS M9 band, depending upon the concentration of water vapor between the tops of these clouds and the VIIRS sensor. Thus, data collected in the VIIRS M9 band are valuable for the detection of both high-level ice clouds and mid-level and lower-level water clouds. In addition, these data can be used to differentiate between mid-level and lower-level water clouds.

Thus, the M9 spectral band should be extremely useful for scene interpretation since surface features are generally masked in these data. The result is a high probability of detecting very thin cirrus clouds even in the presence of more highly reflective, low-level water clouds. However, in extreme elevations, the possibility exists for energy reflected from snow covered surfaces to arrive at the VIIRS sensor. Therefore, it is important that the 1.378 μm data be used in conjunction with 1.6 μm or 3.7 μm albedo imagery.

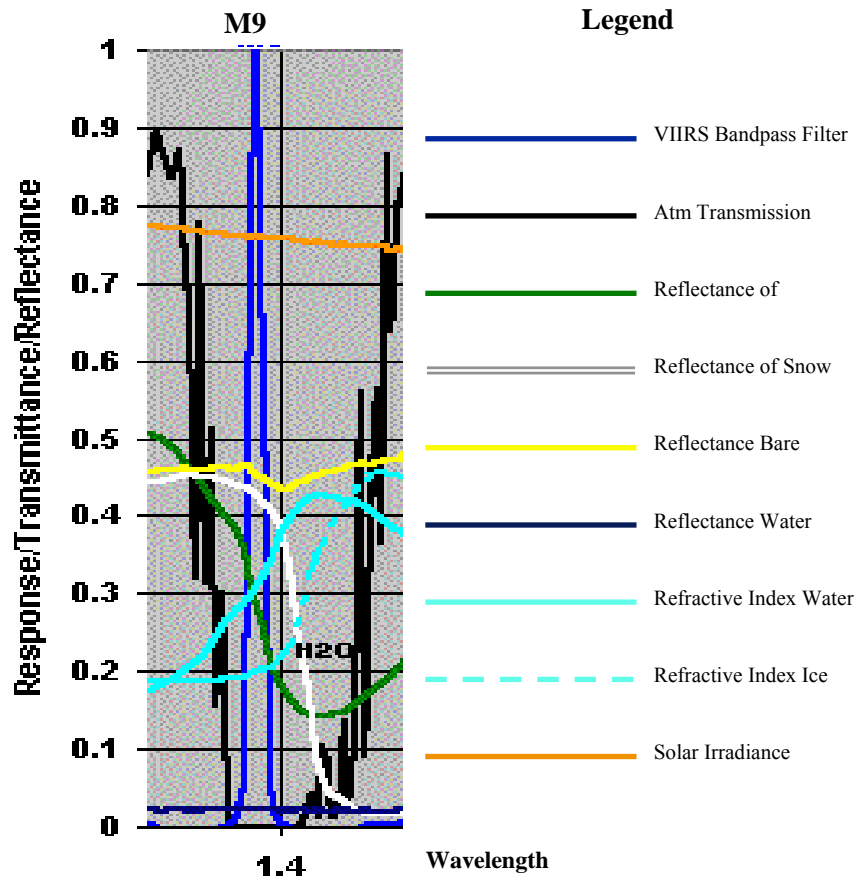


Figure 46. Theoretical calculations of atmospheric and surface properties in the 1.378 μm band that constitutes the VIIRS M9 band.

Finally, it is noted that the bandwidth of VIIRS M9 is 15 nm, half the width of MODIS Channel 26. The narrower VIIRS bandwidth will reduce the risk that side lobes in the spectral response will allow leakage of surface signals to contaminate the cirrus signal.

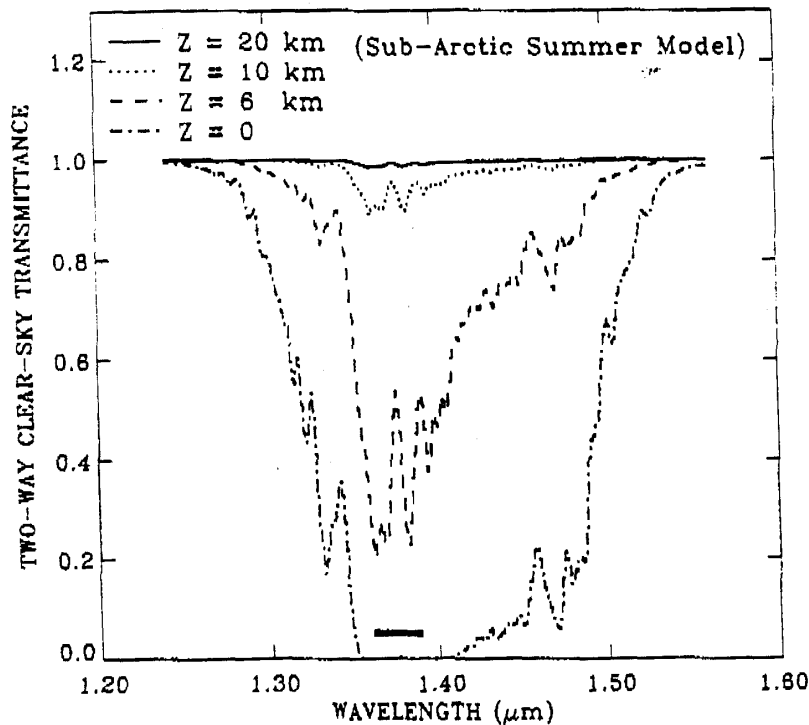


Figure 47. The two-way clear-sky transmittances for energy arriving at satellite altitude in the 1.38 μm region for a perfect reflector located at different altitudes. Calculations based upon sub-Arctic summer atmosphere and LOWTRAN. (Gao et al., 1993).

5.3.2.2. Representative Imagery of the VIIRS M9 Band ($1.378 \pm 0.075 \mu\text{m}$)

The imagery shown in this section was collected by the Airborne Visible/Infrared Imaging Spectrometer (AVIRIS) sensor. Imagery collected by the very similar 1.88 μm band of the MODIS Airborne Simulator (MAS) is shown in Chapter 6. The AVIRIS sensor consists of four spectrometers that cover the 0.4-2.5 μm range providing data in 224 spectral bands. Each band is 10 nanometers wide and the bands are interleaved by line (Goetz et al., 1985; Vane 1987). The resolution of a typical AVIRIS pixel is about 20 meters, for data collected by aircraft flying at a nominal altitude of 20 km. Both the MAS and AVIRIS sensors were flown on NASA's ER-2 aircraft. AVIRIS data are archived at the Jet Propulsion Laboratory.

Two scenes of AVIRIS data are shown in Figures 48-49, each with different surface characteristics. The first scene selected was collected over Coffeyville, Kansas at 1923 GMT on December 5, 1991 and represents a case of moderate surface reflectivity. The second scene was recorded over the Gulf of Mexico area at 1543 GMT earlier on December 5, 1991 and represents the case of low surface reflectivity.

Figure 48 shows the 0.64 and 1.38 μm imagery collected over the Coffeyville, Kansas region as part of the First ISCCP Regional Experiment (FIRE) IFO. Notice that surface features clearly visible in the 0.64 μm band cannot be seen in the 1.38 μm image. Also, no cloud cover is evident in the shorter wavelength data; however, cirrus is obviously present in the upper left and right corners in the 1.38 μm image. In this case, it is more difficult to determine whether the signatures in the remaining 1.38 μm pixels were due to thin cirrus or sensor noise. Similar difficulties were not present with the next generation of AVIRIS sensors.



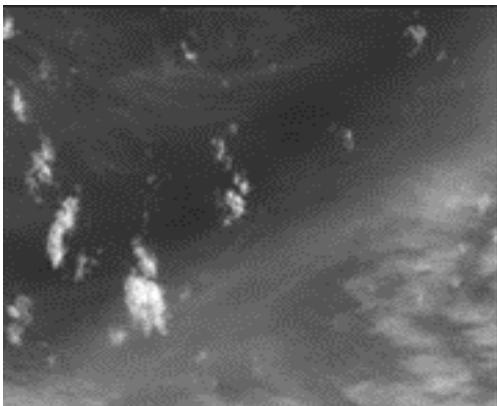
0.645 μm AVIRIS Channel



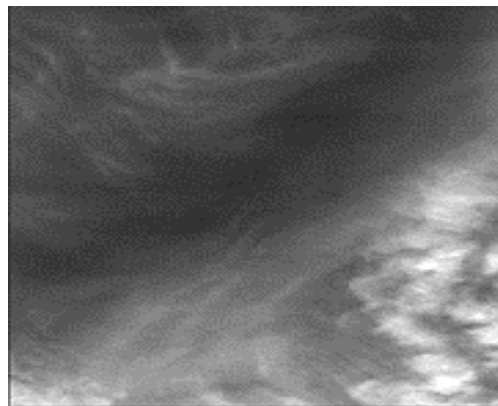
1.378 μm AVIRIS Channel

Figure 48. AVIRIS imagery for VIIRS I2 and M9 channels over Coffeyville, KS shows value of masking surface features for manual interpretation of thin cirrus.

The second scene shown in Figure 49 was recorded over the Gulf of Mexico area. Lower-level water clouds and some cirrus are evident in the 0.64 μm AVIRIS imagery. However, only the cirrus are seen in the 1.38 μm spectral band. The signature of the low-level water clouds is suppressed in the 1.38 μm band because there is sufficient water vapor present above the water cloud top to absorb energy reflected from it. Therefore, the 1.38 μm band provides the analyst with the unique capability to identify multiple cloud layers in single pixels of imagery.



0.645 μm AVIRIS Channel



1.378 μm AVIRIS Channel

Figure 49. AVIRIS imagery for VIIRS I1 and M9 channels over Texas Gulf Coast reveals that low-level water clouds are masked in 1.38 μm imagery.

Chapter 6

MULTICOLOR COMPOSITES OF MULTISPECTRAL IMAGERY

6.1. INTRODUCTION

Image enhancement techniques can facilitate the simultaneous interpretation of many cloud and background signatures in multiple bands of meteorological satellite imagery. In Chapter 5, background information was provided on the energy sources observed by the VIIRS sensor and on the interpretation of these observations in each VIIRS band. Individual signatures found in a given band can be viewed with those of additional bands using color imagery composites. These composites speed the process of manual image interpretation and decrease ambiguities in the signatures found in any single image by viewing the signatures in multiple bands simultaneously. In this chapter, sample color composites are provided to extract specific types of information in multiple scenarios. Before looking at examples of false color composites, background information is provided on the concept of creating and using color composites for image interpretation.

Color composites are highly valuable for visualizing differences in spectral signatures of numerous features simultaneously in multispectral satellite imagery. A color composite is created when one imagery channel is viewed in either the red, blue, and green gun of a color CRT and one or more different channels is placed in the remaining guns. Assume that one of three different spectral bands is placed in the red gun, another is in the blue gun and yet another is in the green gun of the CRT. A feature in the scene will appear reddish, greenish, bluish, or some combination of these colors when its signature is more distinct in one or two of the channels than it is in the third. If little or no difference exists in the spectral signature of a feature in all channels, the feature will appear black, white, or another shade of gray. The variations in gray-shade depend upon whether the brightness temperature of the feature is cold or hot in infrared channels or whether they reflect solar energy strongly or weakly in the visible and near-IR bands.

The concept of constructing color composites is demonstrated with the scene over California previously shown in Figures 3, 20, and 22. In Figure 50, the 0.865 μm channel is assigned to the green gun of the CRT while the 0.64 μm channel is assigned to the red and blue guns.

This very popular color composite is useful to map vegetation since densely vegetated regions appear green while poorly vegetated surfaces appear a shade of gray. The greenish hue in the color composite occurs because the reflectivity of vegetated surfaces is very low in the 0.6-0.7 μm region then increases markedly with wavelengths between 0.7 – 0.75 μm where it becomes nearly constant through 1.0 μm , as was shown in Figure 10. On the other hand, the reflectivity of bare soil increases slowly over the same spectral region. In the 0.64 μm band, the reflectivity of bare soil is slightly larger than vegetated surfaces but the situation is reversed at 0.865 μm . Thus, the mountains and highly agricultural regions of California are brilliant green while the deserts regions, in the lower right corner of the scene, have a grayish hue because the signature of bare soil is nearly the same in both channels. Clouds and the snow covered surfaces in the Sierra

Mountains are a (bright) shade of gray in the color composite because the reflectivity of these features are very similar and high in each band. The cloud-free areas of the ocean have a dark, purple hue since the albedo in both bands are low but Rayleigh scattering produces a slightly higher albedo in the shorter wavelength band.

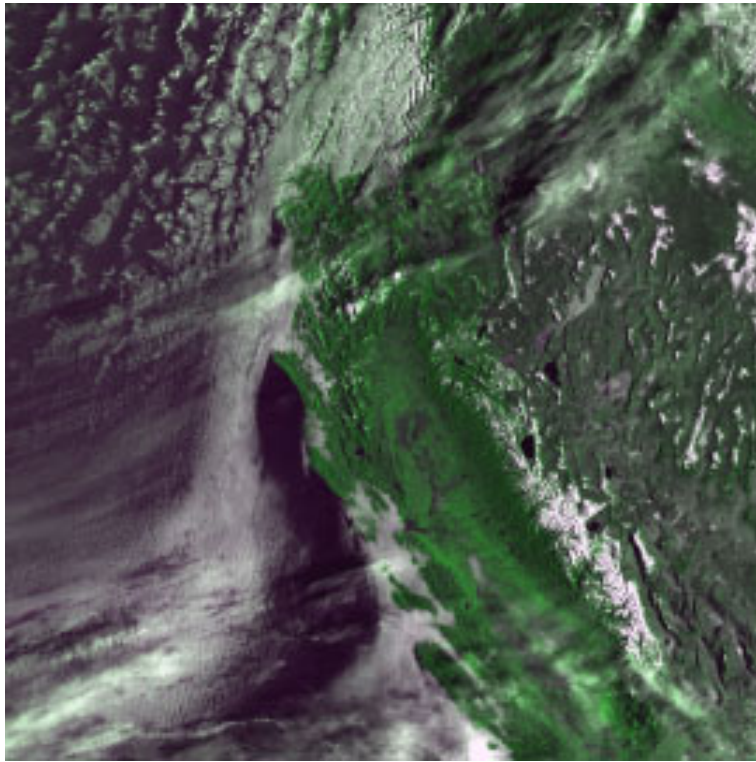


Figure 50. Color composite to emphasize vegetated land surfaces created by assigning 0.64 μm band assigned to red and green guns of CRT and 0.865 μm albedo channel assigned to blue gun.

Several color composites may be needed to accurately interpret all features in any given scene. For example, using Figure 50 it remains difficult to distinguish between snow and water clouds; therefore, additional spectral data must be used to resolve these ambiguities. Additionally, color composites can be created to emphasize variations in brightness temperatures as well as reflectivities. At least one IR channel, consisting of brightness temperatures, is needed to obtain information on relative cloud top heights. The 12.0 μm band is most valuable for this purpose.

It is the focus of this chapter to provide the reader with a variety of color composites that can be used to interpret the contents of features contained in multispectral imagery collected by the NPOESS VIIRS sensor. Background information obtained from the creation of these color composites should be useful in providing the reader with the knowledge necessary to create additional composites for unique mission applications.

6.2. COLOR COMPOSITES OF (0.64 μm , 0.865 μm , AND 12.0 μm) SURFACE VEGETATION AND CLOUD CLASSIFICATION FROM VIIRS IMAGERY BANDS

Color composites that contain at least one VIIRS IR channel provide valuable information on feature temperatures that are useful for cloud classification. Figure 51 contains the same scene shown in Figures 3, 20, 22, and 50. This color composite contains the 0.64 μm (visible) channel assigned to the red gun, the 0.865 μm (near-IR) channel to the green gun, and the 12.0 μm IR band assigned to the blue gun. The IR channel is displayed in the inverted mode, i.e. warm is dark and cold is bright. The major difference between the color composites shown in Figure 50 and Figure 51 is that the latter provides information on cloud top temperatures and relative heights in addition to the same information on vegetation and land/water boundaries found in the earlier figure.

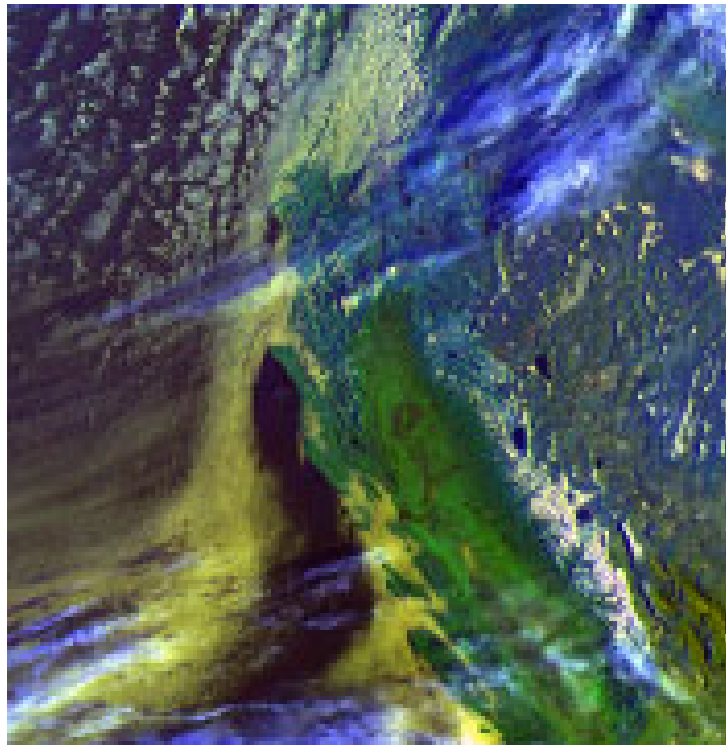


Figure 51. Placing the 12.0 μm channel in the blue gun of Figure 50 provides valuable data on cloud top temperatures needed for cloud typing. Warm, low level water clouds appear yellow while colder ice clouds are blue.

In Figure 51, distinction is readily made between low-level water clouds, seen as yellow, and the much colder ice clouds, which appear blue. The yellowish hue of the water clouds results from nearly equal contributions from the red and green guns of the CRT since water clouds are highly reflective and bright in both bands. On the other hand, the blue gun contains 50% less energy, since these water clouds are relatively warm and thus provide much less energy to the blue gun.

Thin cirrus appears blue in Figure 51 because this gun has more than twice the energy

contribution than either the red or green guns. Cirrus contributes much more energy to the blue gun of the CRT, when displayed in the inverted mode, since these clouds are very cold in the far-IR channel but have low albedos in both the visible and near-IR bands. Regions of dense or optically thick cirrus appear less blue, e.g. bright shade of gray, because thick cirrus cloud elements can be very cold and highly reflective so the energy contributions in all guns of the CRT are similar.

The color composite shows the cumuliform clouds in the upper left-corner have temperatures that are warmer than the (blue) cirrus but colder than the (yellow) stratus. Thus, these clouds probably occur in the middle-levels of the atmosphere but may also be lower-level clouds in a much colder air mass than found in the bottom left corner of the scene. Thus, it is important to compare cloud top temperatures in the far-IR band with adjacent cloud-free temperatures to determine approximate cloud top height.

Finally, land regions in the right part of the scene have a bluish hue because the land is relatively cold and sparsely vegetated, especially near snow fields. Analyses show these regions have most energy in the blue gun and slightly more energy in the green gun than in the red gun. Thus, the land must be sparsely vegetated.

It is emphasized that the inclusion of the 12.0 μm band into a color composite provides valuable information on cloud top temperatures which is most valuable for manual cloud classifications. In Figure 51, the following clouds have been identified:

- (d) Stratus – yellow
- (e) Stratocumulus - yellow
- (f) Thin cirrus – blue
- (g) Thick cirrus – white
- (h) Altostratus – greenish
- (i) Altocumulus - greenish

Snow along the Sierra Nevada mountains remains white because it is highly reflective in the solar bands and very cold in the thermal bands. White means there is no unique spectral signature for snow in this color composite. While the presence of snow is inferred by the dendritic pattern in the mountain regions, additional spectral data might be needed to positively confirm the presence of snow in another scene, based solely upon its signature in a color composite. For example, additional spectral data are essential to identify snow in non-mountainous regions where scene interpretation might be complicated by the presence of other relatively cold features, including supercooled clouds.

6.3 COLOR COMPOSITES OF (3.7 μm ALBEDO, 0.865 μm , 12.0 μm) POSITIVE SNOW DETECTION WITH VIIRS IMAGERY BANDS

Snow appears white in the color composites shown in Figures 50 and 51 because it is highly reflective in both the 0.64 μm and 0.865 μm bands and cold in the 12.0 μm band. Thus equal contributions are received from snow by each gun in the CRT. While snow covered regions were readily identified by the dendritic patterns in the mountainous regions of these earlier scenes, it becomes more difficult to identify in less rugged terrain without the use of specific imagery where snow has a unique spectral signature. In this section, another VIIRS band is examined, where the spectral signature of snow is very different than those shown previously. Thus use of this band allows snow to be positively identified in any sunlit terrain. The color composite is shown in Figure 52 below.

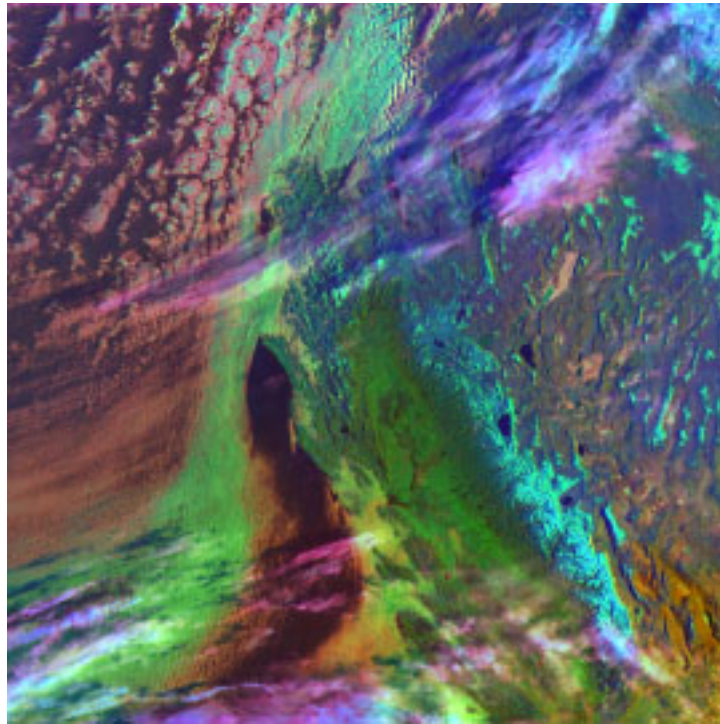


Figure 52. Replacing the band in the red gun of Figure 51 with the 3.7 albedo channel allows snow to be differentiated from lower-level water clouds, thin cirrus, and thicker cirrus while maintaining information on cloud top temperatures and vegetated land surfaces (red = 3.7 μm albedo, green = 0.865 μm , blue = 12.0 μm).

Snow appears turquoise in Figure 52 because it is highly reflective in the 0.865 μm band and very poorly reflective in the derived 3.7 μm (albedo) channel while relatively cold temperature exist in the 12.0 μm band. Turquoise results from the absence of red in the CRT display. Thus, an extensive area of snow is readily seen along the entire Sierra Nevada Mountain Range. Smaller regions of snow are seen east and north of these mountains, over Nevada, Utah, and Idaho. In addition, snow is confirmed in this color image in the mountains just north of the San Joaquin Valley. Specially, Mt Shasta can vaguely be seen through the thin cirrus clouds. In this composite, snow and thin cirrus are readily differentiated because the signatures of cirrus clouds have a purplish hue,

demonstrating strong signatures in the red and blue guns. It should be noted that use of the 1.6 μm VIIRS channel in place of the 3.7 μm albedo band will produce the same signature for snow; however, the signature of thin cirrus is less dramatic in the 1.6 μm band since the 3.7 μm channel enhances the signature of thin cirrus while the 1.6 μm channel suppresses it. The phenomenology for the enhanced signature of thin cirrus in the 3.7 μm band was discussed in Section 5.2.4.2.3.

The intensity of the turquoise color is related to the combined effects from the green gun and blue guns in the CRT. The contribution in the green gun is generally large, assuming daytime imagery. There is a minimum expected contribution from the blue gun since surface (skin) temperatures of snow-covered areas must be at least freezing. In some regions, surface temperatures may be significantly colder. For example, brightness temperatures in the Sierra Mountains are considerably colder than those seen in the large snow regions on the very right edge of the scene. However, the turquoise appears similar for both regions.

Finally, note the “streets” of snow east of the Sierra Nevada Mountains are surrounded by a blue tint. The bluish hue demonstrates a region of very cold air, which is associated with both altitude of these “smaller” mountains and the airmass over them. In the lower-right corner, the color becomes orange due to the surface being very warm over the Death Valley Desert of California. The snow-covered region just north of Death Valley and east of the Sierra Mountains is readily identified as the White Mountains. The topography of these mountains frequently results in severe, mountain-wave turbulence under proper meteorological conditions with rotor clouds occasionally reported in weather observations issued from Bishop, California.

6.4. COLOR COMPOSITES OF (0.64 μm , 0.64 μm , 3.7 μm ALBEDO) SNOW MAPPING THROUGH THIN CIRRUS CLOUDS WITH VIIRS IMAGERY BANDS

For some applications, it might be useful to determine the presence of snow in cloud-covered conditions, especially when the clouds are optically thin or semi-transparent in the visible part of the solar spectrum. In this section, a methodology is shown to identify snow even if cirrus completely envelops the region. The color composite shown in Figure 53 uses the scene first described in Figures 30 and 31.

The color composite shown in Figure 53 was created by assigning the 0.64 μm band to both the red and green guns of the CRT and the 3.7 μm albedo channel to the blue gun. Snow appears yellow in this composite and can be seen even through the cirrus clouds. Inspection of the 12.0 μm band in Figure 30 reveals overcast cirrus across much of the upper right portion of this region.

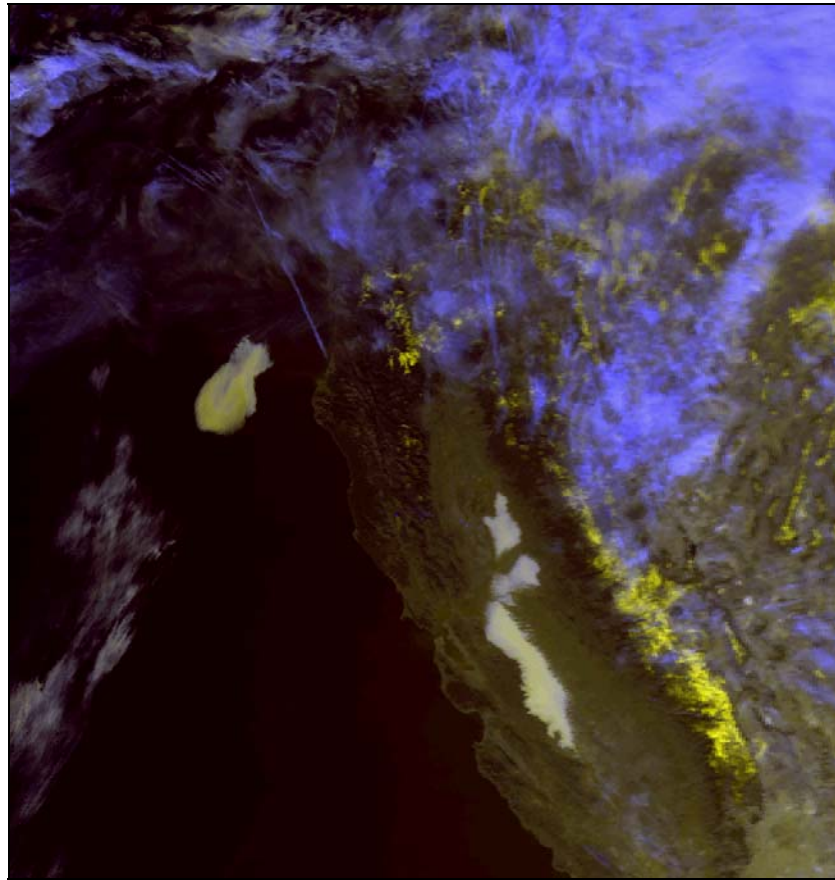


Figure 53. Color composite red = 0.64 μm band, green = 0.64 μm band, blue = 3.7 μm albedo band) for the manual detection and mapping of snow through cirrus cloudy conditions (Hutchison and Locke, 1997).

The yellowish hue of snow in this color composite results from nearly equal energy contributions coming from the red and green guns and the absence of energy in the blue gun. Thin cirrus has a bluish hue since the signature of optically-thin cirrus is enhanced in the 3.7 μm albedo image but much less evident in the 0.64 μm band. Thus, snow can be seen through overcast cirrus clouds since the reflectance of snow is much stronger in the band in which the thin cirrus is not readily seen, i.e. the 0.64 μm channel. Therefore, it is possible to map snow through thin cirrus clouds.

It is noteworthy to mention that the 3.7 μm albedo band cannot be interchanged with the 1.6 μm band for this application. While both the 3.7 μm albedo band and the 1.6 μm band can be used interchangeably to distinguish between water clouds and snow, the 3.7 μm albedo band is more useful for mapping snow through thin cirrus clouds. As noted in Section 5.2.4.2.3, the signature of thin cirrus is simultaneously enhanced while the snow is suppressed in the 3.7 μm albedo band. The signature of thin cirrus is enhanced in the 3.7 μm albedo band because the methodology used to create it makes the image very similar to a 3.7 – 12.0 μm brightness temperature difference field. Thus, it is the thermal signature of the thin cirrus that is enhanced in the 3.7 μm albedo band. There is no thermal (terrestrial) energy in the 1.6 μm band.

Finally, the signature of snow and water clouds can be very similar in this color composite as seen by the yellowish hue of the stratus clouds located in the San Joaquin Valley and off the California coast. An additional color composite that uses the 1.6 μm channel is essential to avoid any confusion between water clouds and snow-covered surfaces.

6.5. COLOR COMPOSITES OF (0.412 μm , 0.865 μm , AND 0.64 μm) CLOUDS OVER ARID REGIONS USING VIIRS IMAGERY AND IMAGERY ASSIST BANDS

The color composite shown in Figure 54 was generated using SeaWiFS data collected over the Southwestern US on July 13, 2001. The scene contains a large layer of stratocumulus in the left-bottom corner, to the left of Baja California. The Altar Desert is located in the middle of the scene, and the Gulf of California at the bottom center of the image. Gray-scale images and descriptions of these data are at Figure 23 and Figure 45a.

This color composite was created by assigning the 412 nm or 0.412 μm (M1) band to the red gun, the 0.865 μm (I2) band to the green gun and the 0.64 μm (I1) band to the blue gun. Densely vegetated regions appear green in the composite image, while bare soil, sand, and very sparsely vegetated regions appear turquoise, due to the strong contributions of green and blue channels but the absence of red, as discussed in Section 6.3. The 0.412 μm band was identified as an Imagery Assist band in the VIIRS design since albedos over desert have a minimum in this VIIRS bandpass. Therefore, water clouds, when present in desert regions, appear as bright shade of gray (or white) since they strongly reflect energy in each of the bandpasses. Thus, this composite assists in the differentiation between obscurations cause by clouds and perhaps blowing sand in arid environments.

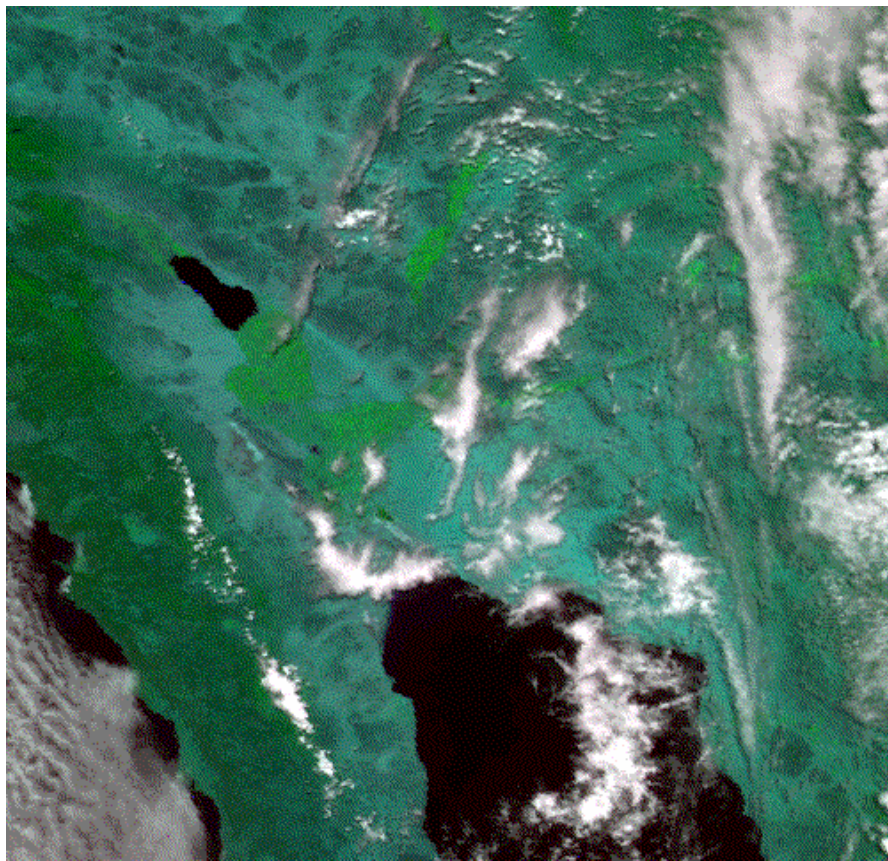


Figure 54. Composite image (red = 0.412 μm , green = 0.865 μm , blue = 0.64 μm) for the detection clouds over highly reflective, arid or semi-arid regions.

The strong separation between bare soil (turquoise) and vegetated (green) regions result from the cross-over in reflectivities for these surfaces between 0.64 and 0.865 μm . As seen in Figure 10, the reflectivity of bare soil is about 20 percent at the shorter wavelength while that for vegetated land is only 5 percent. At 0.865 μm , the reflectivity for vegetated regions is about 55 percent while that for bare soil is now around 35 percent. In addition, both surface types reflect energy very poorly at 0.412 μm . Therefore, bare vegetated regions contribute mostly in the 0.865 μm band (placed in the green gun of the CRT), while bare soil contributes nearly equally to the green and blue guns. Neither bare soil nor vegetated regions contribute to the red gun. Clouds appear white since they are highly reflective in all bands. Ocean is dark since it does not reflect significant energy in any of the three bands.

The fact that VIIRS Imagery resolution bands have a spatial resolution of 371 m while the Imagery Assist band has a spatial resolution of 742 m is of little consequence on this or any color composite. However, it is necessary to perform pixel replication on the 0.412 μm band to make all channels have the same number of pixels in the scene. If pixel replication exceeds 2:1, which is the maximum needed to use Imagery Assist data with VIIRS imagery resolution bands, distortion may become evident in the interpretation of the scene.

6.6. COLOR COMPOSITES SERIES FROM MODIS AIRBORNE SIMULATOR DATA

The remaining Red Green Blue (RGB) Color Composites have been selected due to their spectral content. They are useful to an analyst in Cloud Type determination as well as Cloud vs. Snow/Ice background discrimination. These RGBs have been generated using 3 MODIS Airborne Simulator (MAS) scenes from the SUCCESS and ARMCAS Campaigns. The features identified in each RGB are explained in the sub-captions.

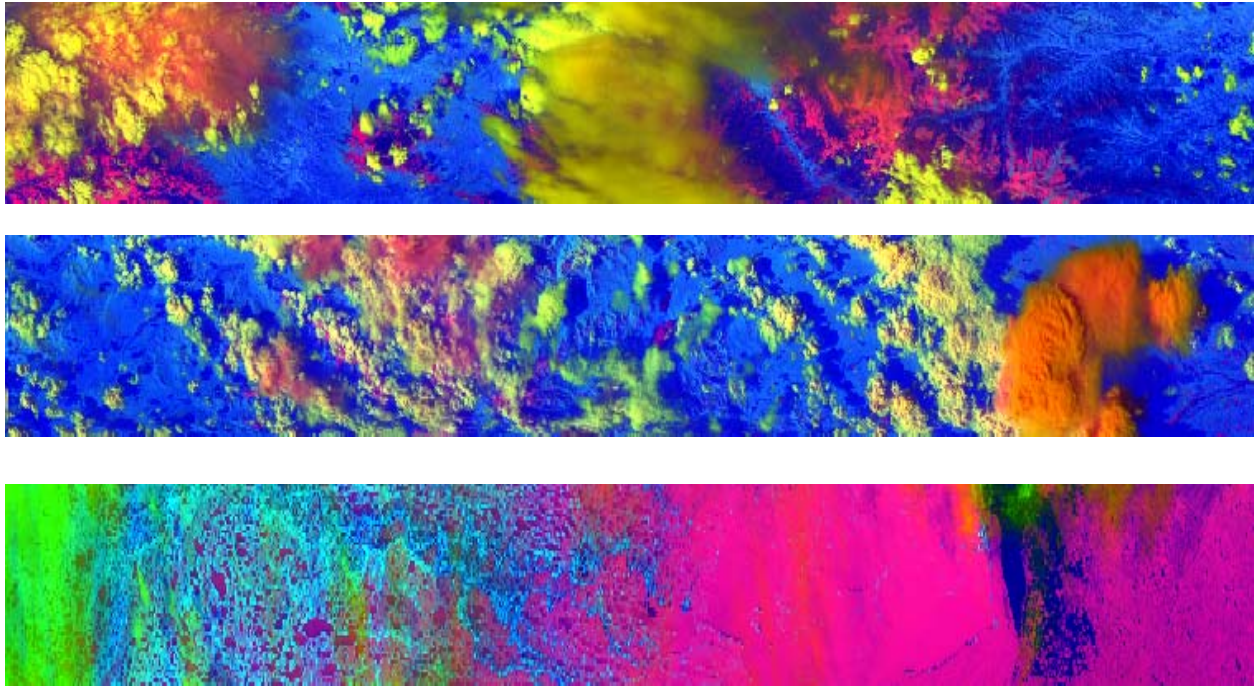


Figure 55. RGB (0.64, 1.61, BT10.8/BT12.0)

Using this RGB composite snow/ice surfaces are rose to purple, low clouds are yellow, high (water) clouds range from yellow to green, thin cirrus over snow/ice is orange, and vegetated land is blue. The thundercloud in the middle scene is believed to be orange due to the high reflectance in the visible and absorption in the near IR of the ice contained at its upper levels.

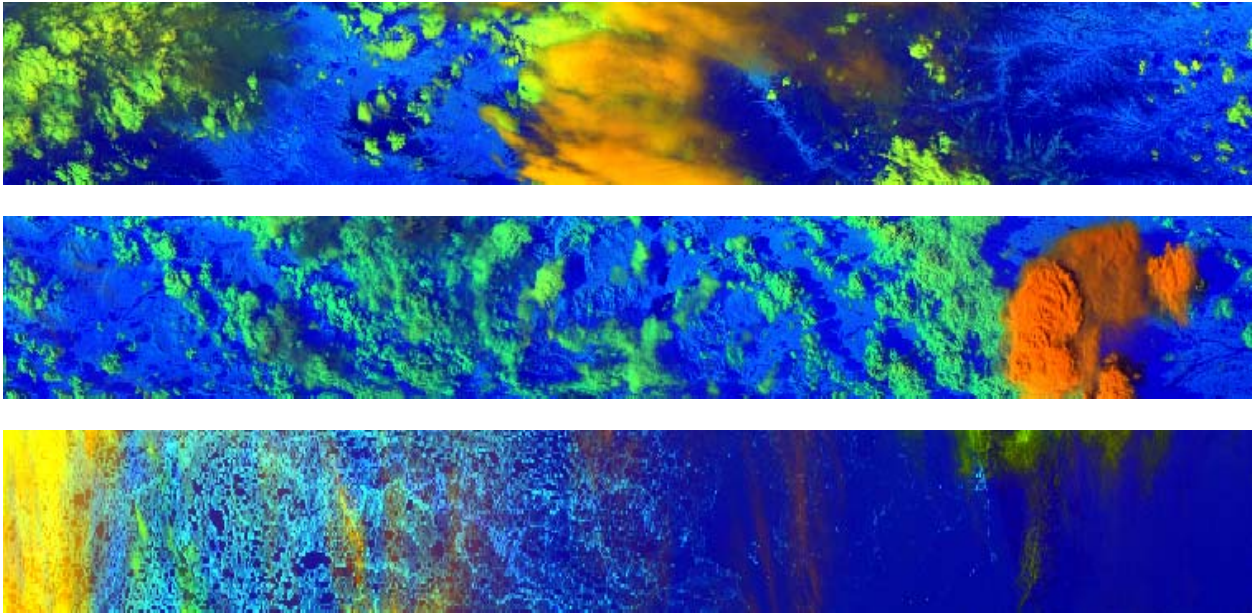


Figure 56. RGB (1.38[1.88], 1.61, 12.0)

Using this RGB composite masks out snow ice fields making them the same coloration as vegetated land. Land with a low amount of vegetation tends to be aqua blue. Optically thin cirrus has a deep bluish hue, lower level water clouds appear greenish, optically thick cirrus are more golden to orange. Overshooting tops such as the thundercloud in the middle figure appear orange.

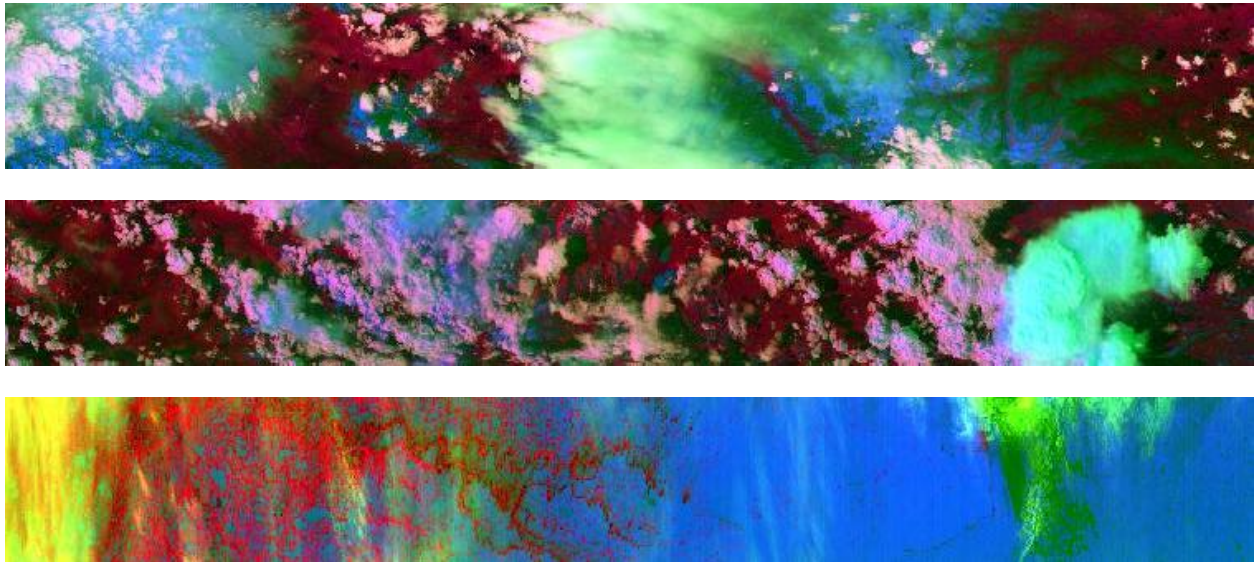


Figure 57. RGB (1.61, Invert BT8.6, 0.64)

Using this RGB composite one can distinguish between lower level cumulus and upper level cirrus and snow/ice fields. Snow/ice fields are blue. Optically-thin cirrus has a yellow-greenish-turquoise hue, lower-level water clouds are rose to white, overlaying mid-level water clouds are darker blue. Vegetated surfaces are red.

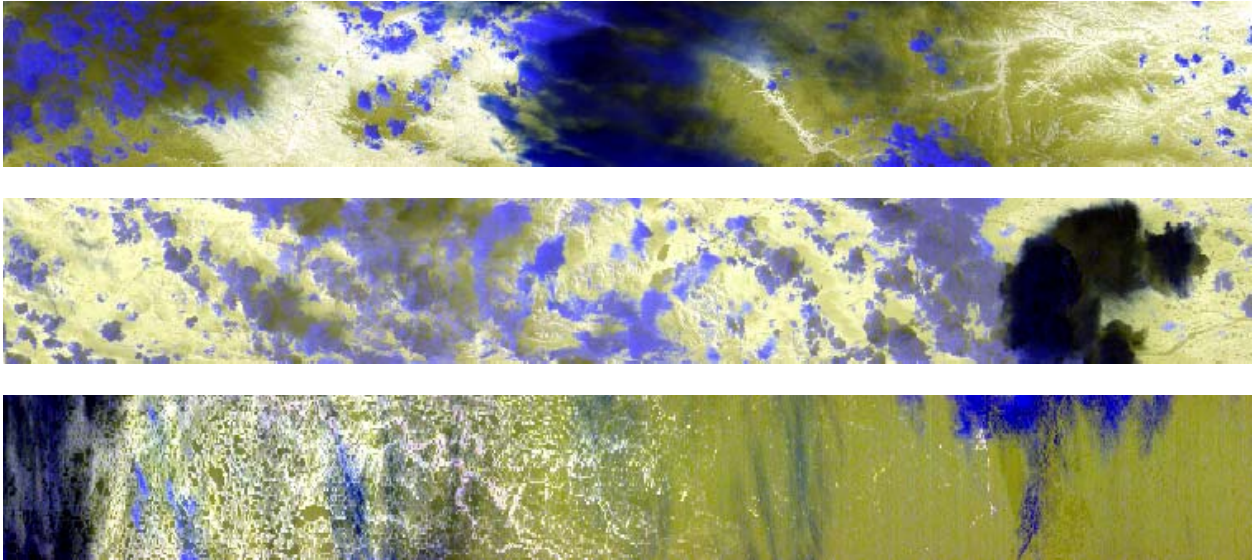


Figure 58. RGB (BT11, BT8.6, BT3.75)

Using this RGB composite one can distinguish between lower level Cumulus and upper level Cirrus and snow/ice fields. Snow/ice fields are olive-green, optically thin cirrus has a deep blue-blackish hue over land and blue over ice, lower level water clouds are dark blue, vegetated regions tend to be white. Overshooting tops such as the thunderstorm in the middle figure appear black with clearly defined boundaries, and cellular structure clearly visible.

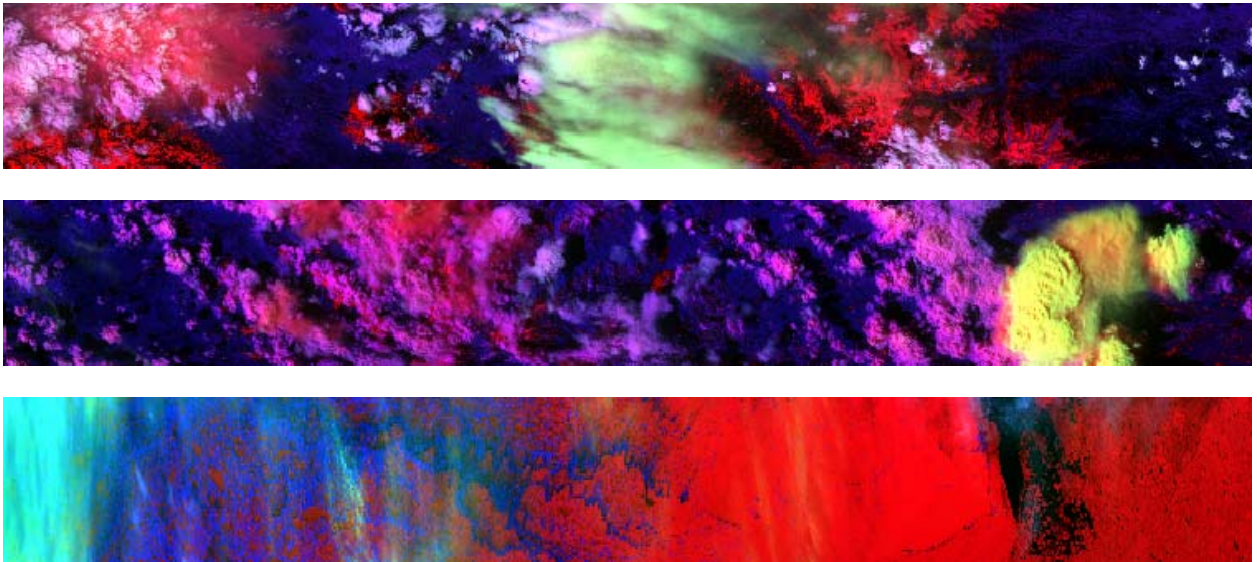


Figure 59. RGB (0.64, 1.38[1.88], 1.61)

Using this RGB composite allows distinction between lower level cumulus and upper level cirrus and snow/ice fields. Snow/ice fields are red, optically-thick cirrus is green and thin cirrus is aqua blue, lowest level water clouds appear dark purple, while middle level appear pin. Overshooting tops from thunderstorms, such as the middle figure, appear yellow with lower cellular structure being orange.

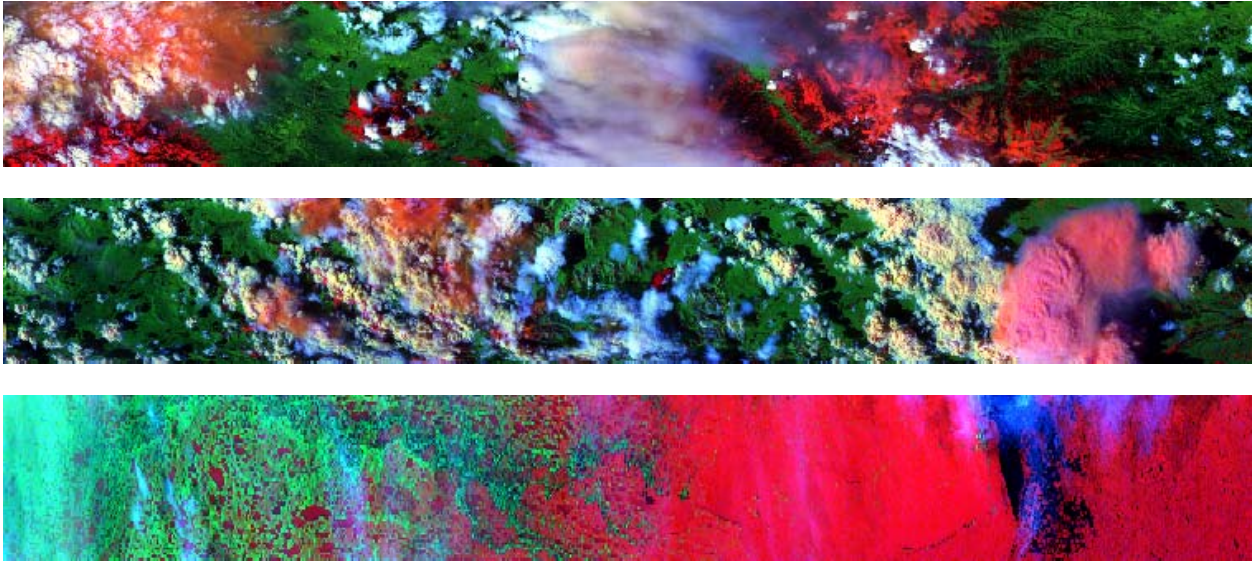


Figure 60. RGB (0.64, 1.61, 3.75A)

Using this RGB composite vegetated land is green, low level water clouds are white, high level cirrus are Grey blue, snow/ice is bright red, and thin cirrus over snow/ice is pink to purple, while over vegetated land it is aqua green. The thundercloud in the middle scene is pink.

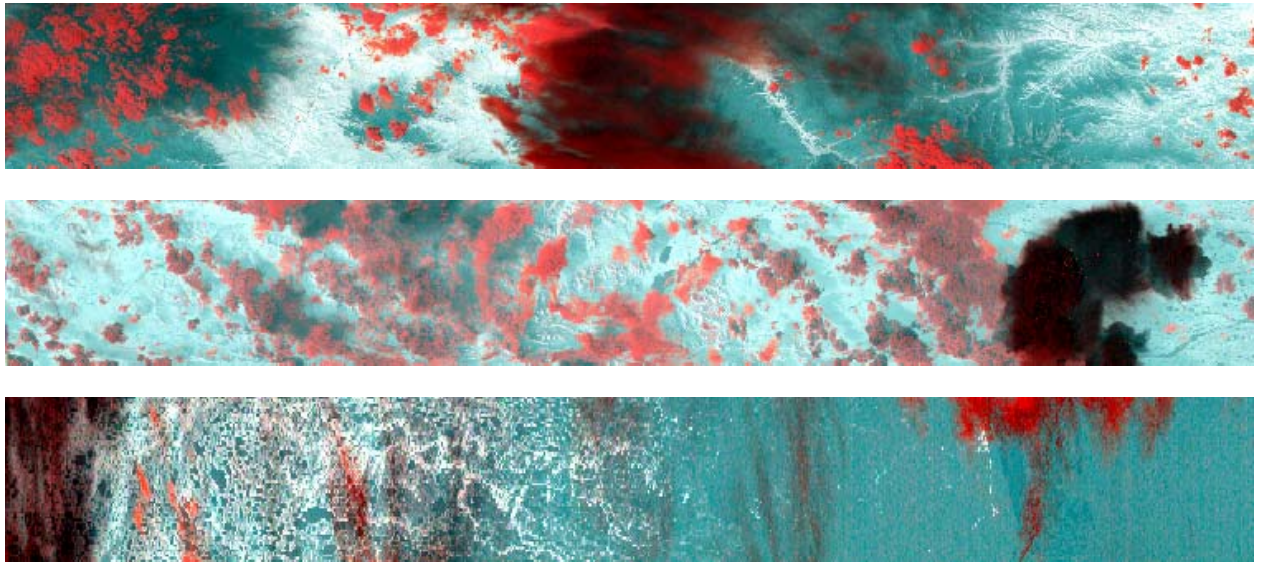


Figure 61. RGB (BT3.75, BT10.8, BT12)

Using this RGB composite snow/ice surfaces are blue-gray, water clouds are bright red over vegetated land, cirrus covered regions are black to gray, thin cirrus over ice is bright red, and vegetated land is white. The cells of the thundercloud in the middle image are clearly visible.

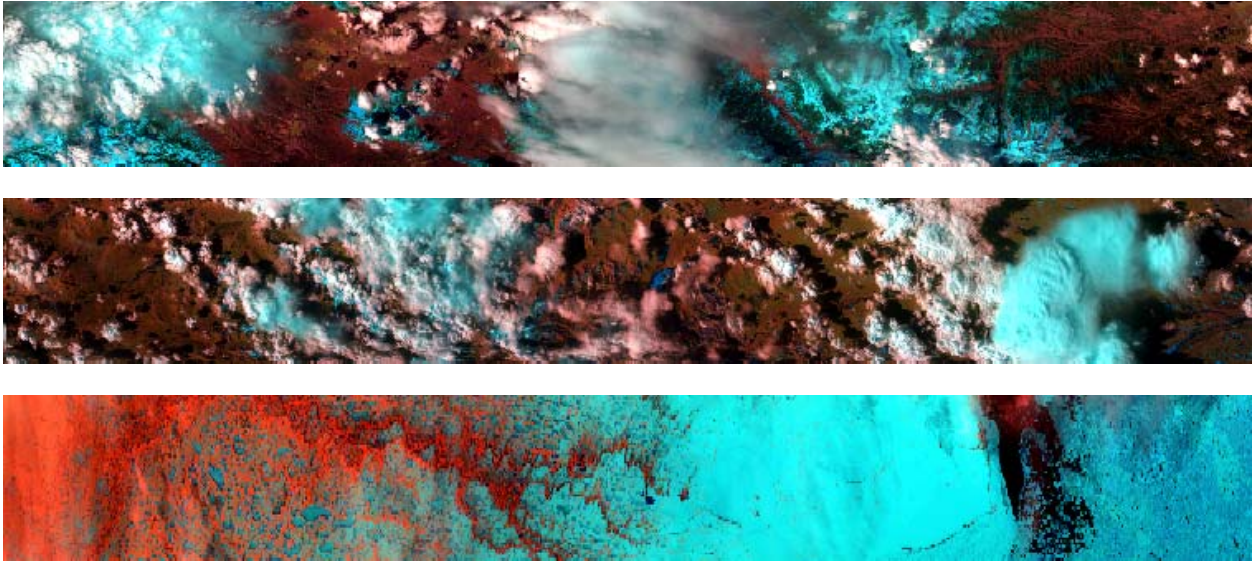


Figure 62. RGB (2.1/1.6, .845, .640)

Using this RGB composite snow/ice surfaces are aqua blue, clouds are white, vegetated land is red, and highly vegetated land such as irrigated regions are green. Above note the middle thundercloud scene optically thin clouds over snow/ice surfaces and clouds that contain a large quantity of ice crystals may be blue.

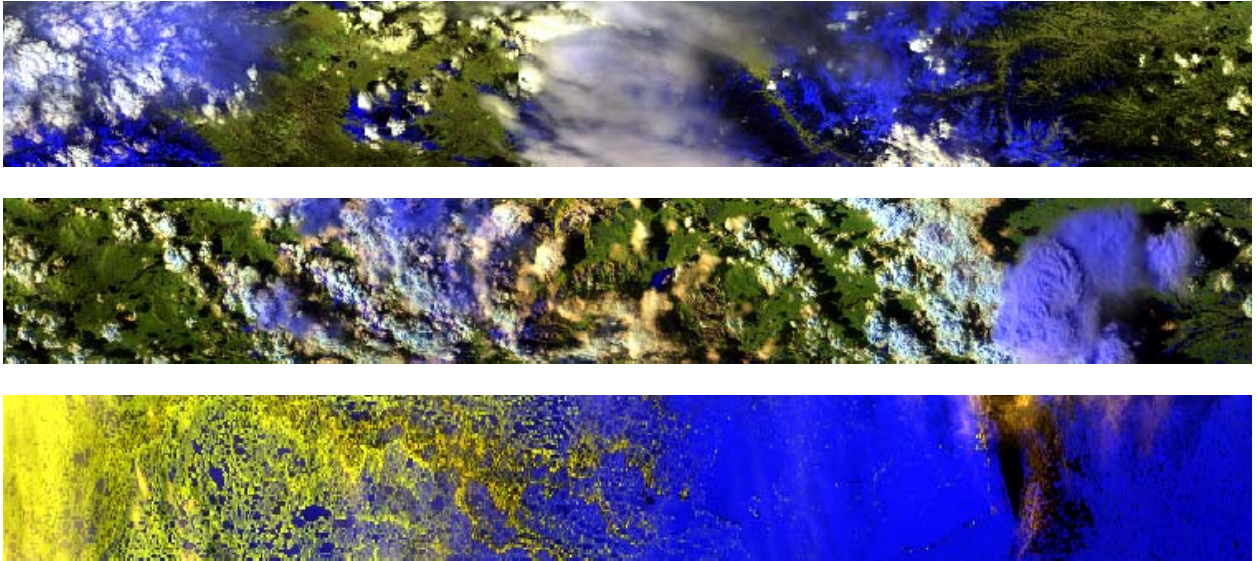


Figure 63. RGB (2.1, 1.6, .640)

Using this RGB composite snow/ice surfaces are dark blue, water clouds are white, vegetated land is green, and highly vegetated land such as irrigated regions are dark green. Above note the middle thundercloud scene optically thin clouds over snow/ice surfaces and clouds that contain a large quantity of ice crystals may be blue. The vegetated regions with this RGB combination also tend to exhibit greater contrast, due to the range of reflectances that vegetated surfaces may have in the near IR bands.

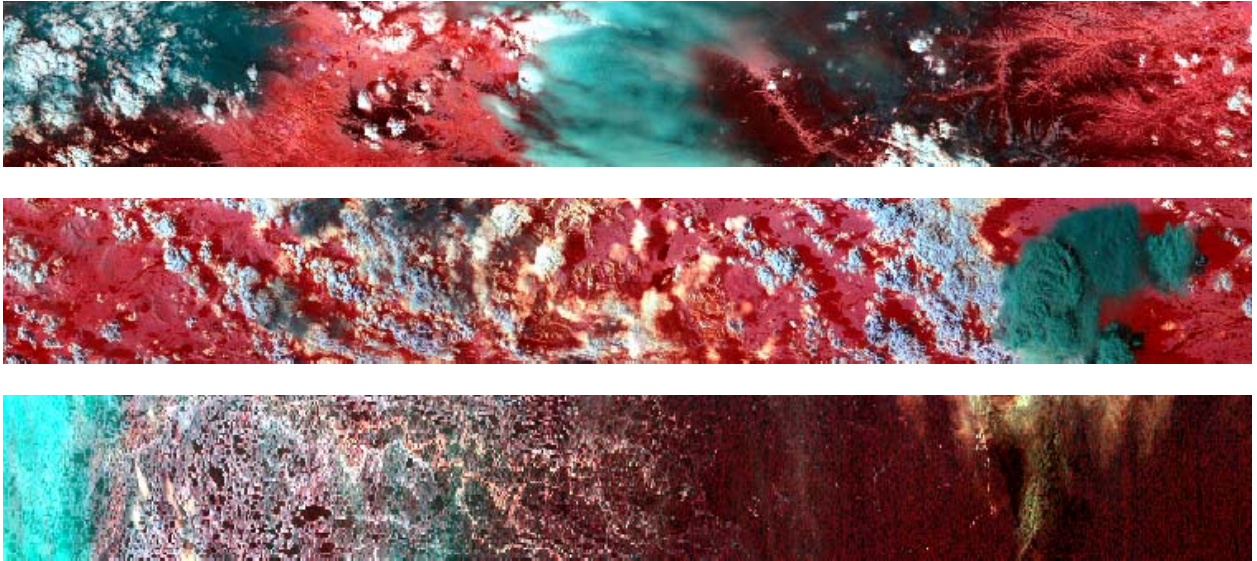


Figure 64. RGB (BT3.75, 2.1, 1.6)

Using this RGB composite vegetated land is bright red and snow/ice surfaces are dark black. Low level water clouds are white, while higher level cirrus clouds are blue when optically thin and grayish blue when optically thick. This variation in color for higher and lower level clouds allows visual discrimination between them.

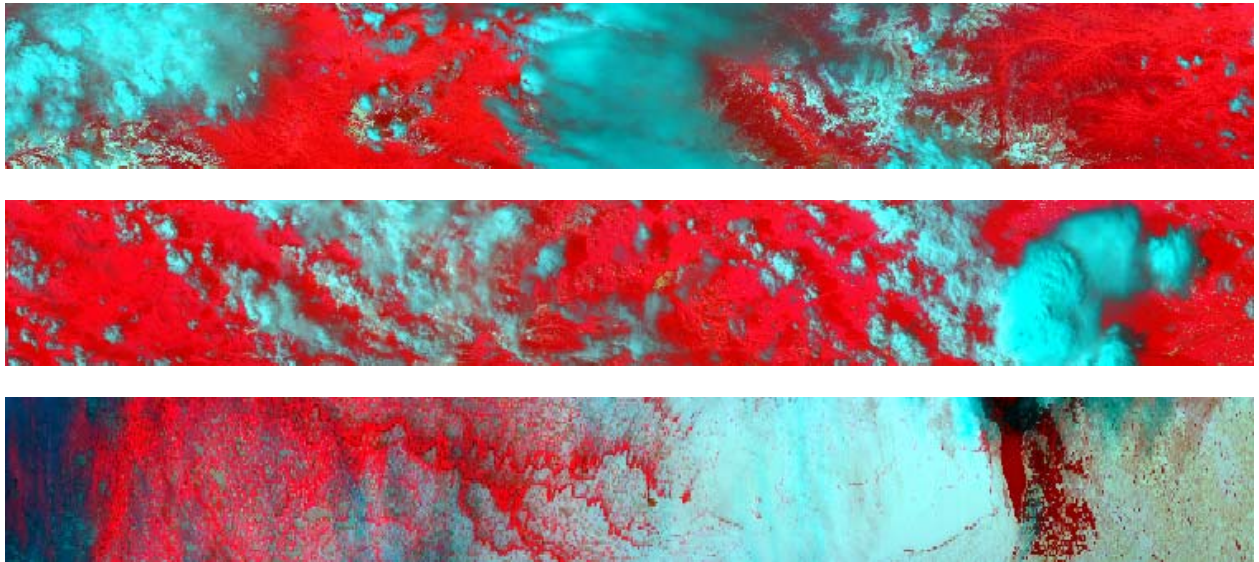


Figure 65. RGB (BT8.6, .640, .845)

Using this RGB composite snow/ice surfaces are aqua blue as are clouds, vegetated land is very bright red. Optically thin cirrus over vegetated land and water are purple. Optically thick cirrus tends to be grayish blue. Caution: it is possible to confuse clouds with snow/ice with this combination.

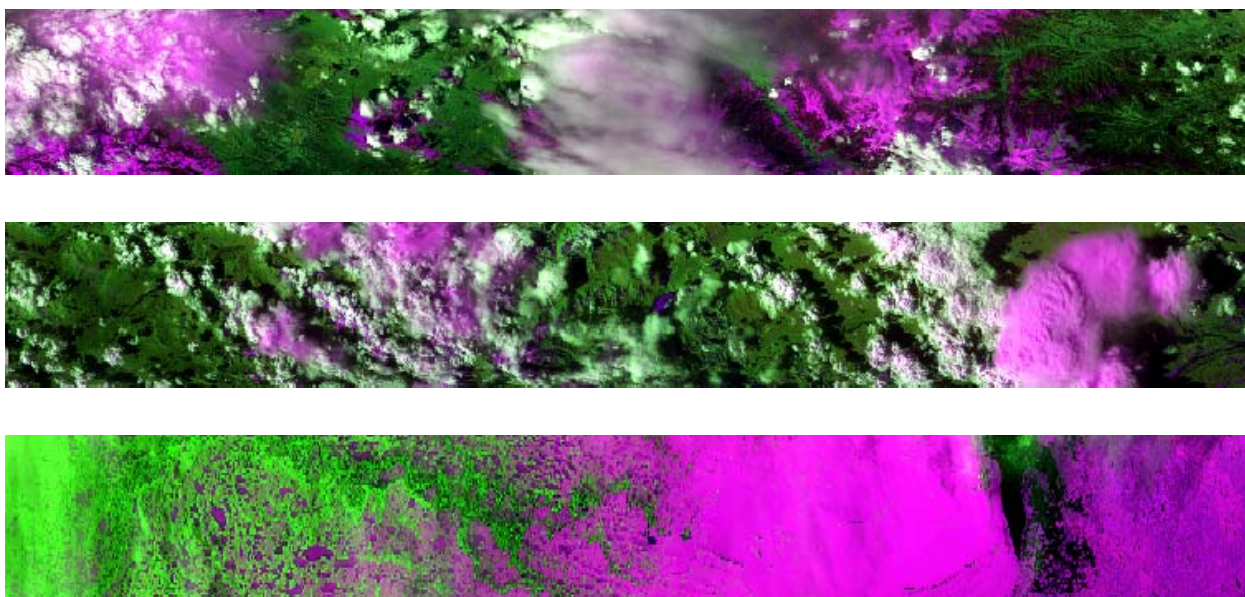


Figure 66. RGB (.86, 1.61, .640)

Using this RGB composite snow/ice surfaces are purple, while water clouds are white, vegetated land is green. Optically thin cirrus over land is green and tends to blur the underlying surface features. Optically thick ice clouds are purple to gray.

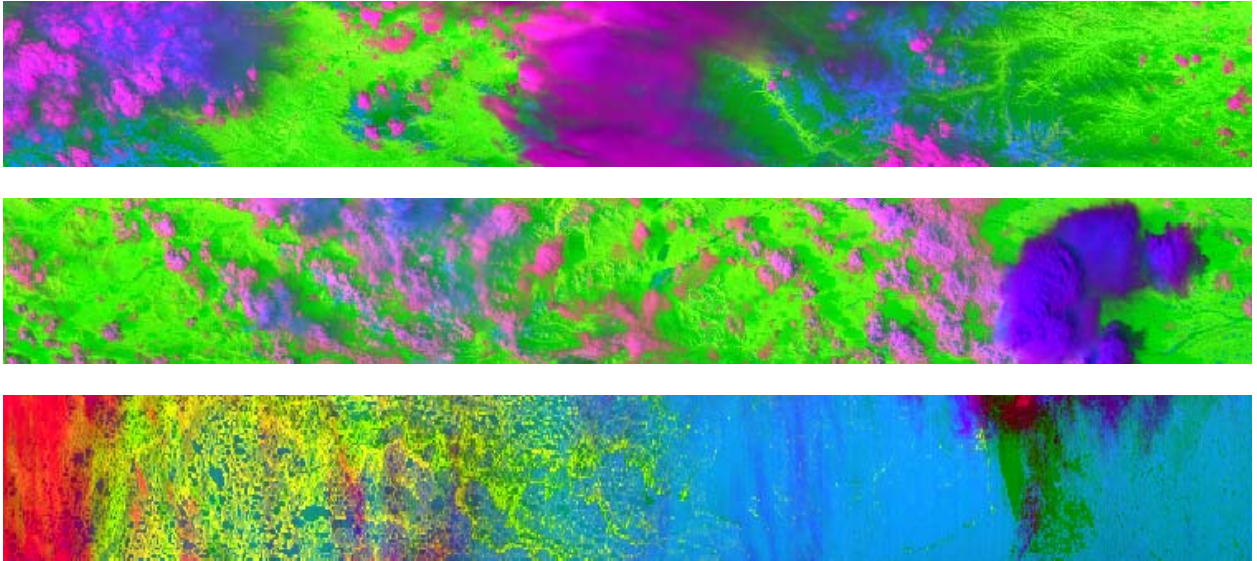


Figure 67. RGB (1.61, BT8.6, .640)

Using this RGB composite brings out dramatic differences within a scene. Clouds are purple to dark blue, the bluer the clouds are the more ice that they contain. Cellular structure in thunderclouds is discernable. Thin cirrus may be red over vegetated land. Snow ice surfaces are light blue, while vegetated land is bright green and sparsely vegetated land is dark green. Snow visible through clouds takes on a darker blue color than the clear snowy regions.

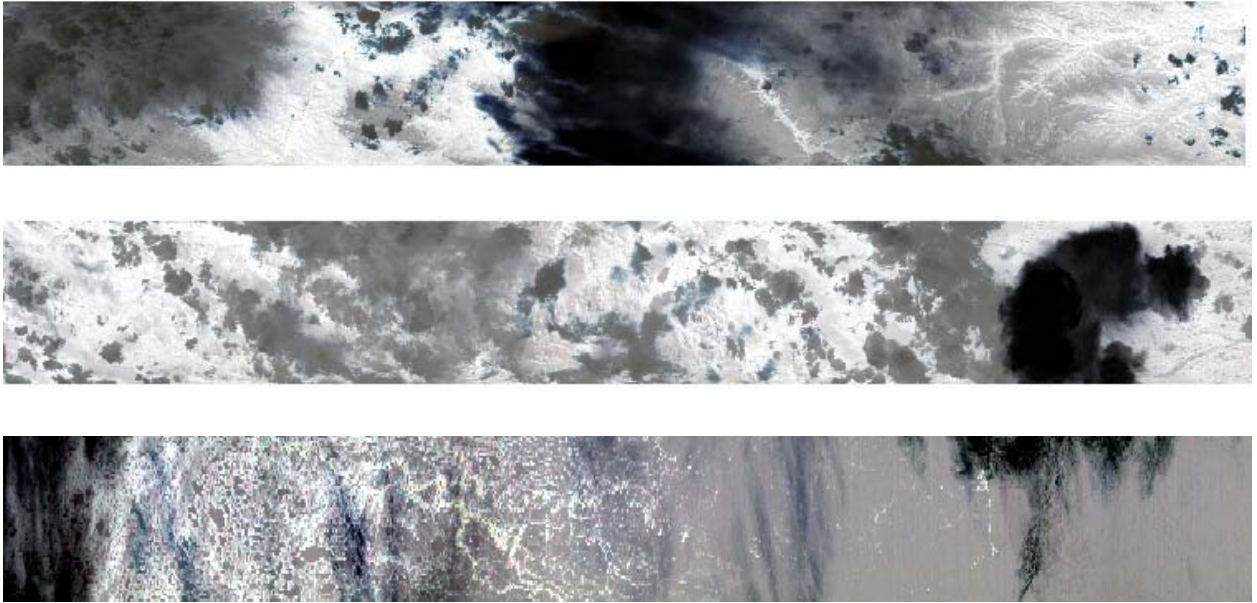


Figure 68. RGB (BT12, BT11, BT8.6)

Using this RGB composite generates an image that is almost gray scale at first glance. However, due to the thermal contrast of clouds over underlying surfaces an analyst can notice them. Vegetated land is white, lower level water clouds are gray, higher level cirrus are black, snow/ice surfaces are gray, and optically thin cirrus can have a blue hue. The thermal contrast in the middle scene allows one to visually separate out the cellular structure of the thundercloud.

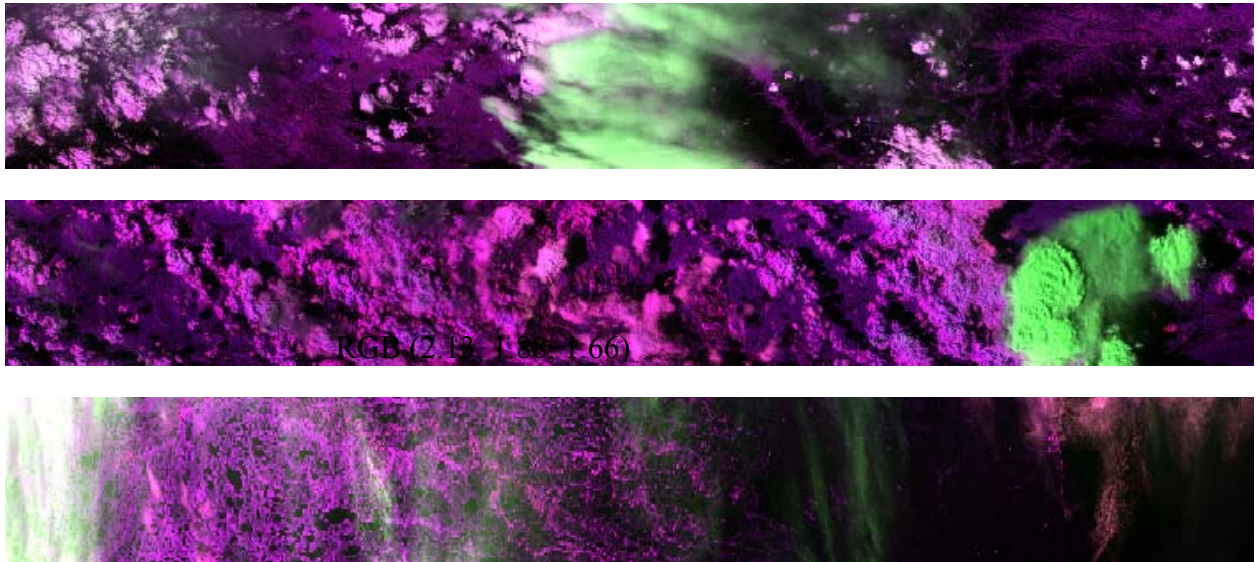


Figure 69. RGB (2.13, 1.38[1.88], 1.66)

Using this near-IR RGB composite snow ice surfaces are black, while vegetated land is black to purple. Lower level water clouds are purple and higher clouds such as cirrus and thunderclouds tend to be from green to white. The whiter the cirrus is the more optically thin it is. This composite is good to use over an ice-covered region to discern clouds from snow/ice and to look for higher cloud presence.

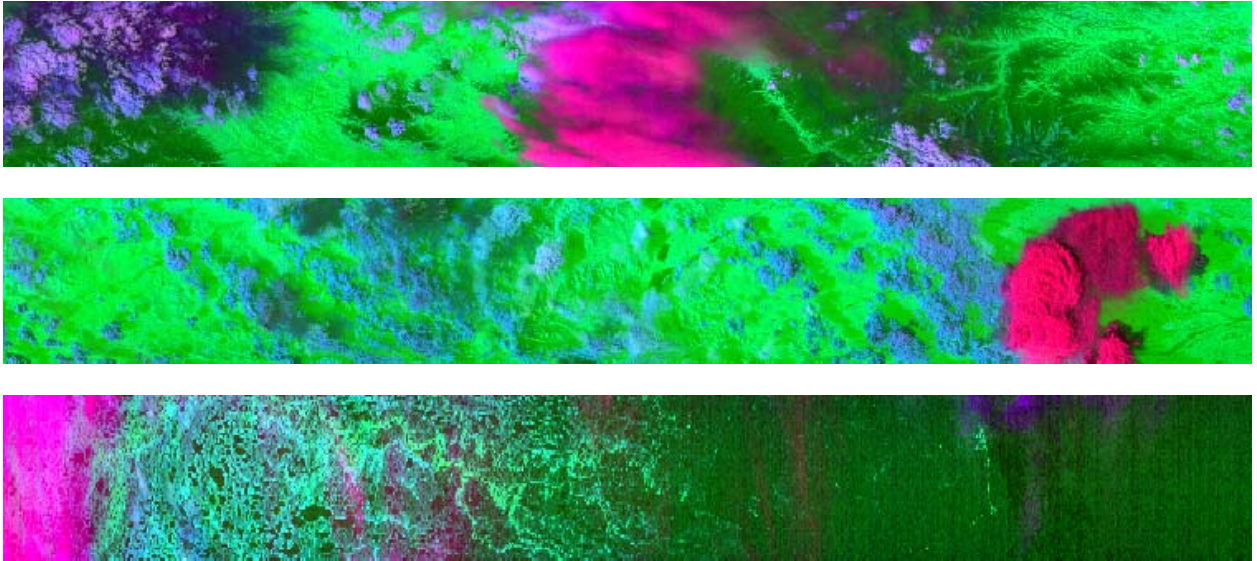


Figure 70. RGB (1.38[1.88], BT4, 1.61)

Using this RGB composite snow/ice surfaces are dark green, lower level water clouds are light blue to dark blue, vegetated land is bright green, with less vegetated being dark green, cirrus over snow and ice is black, high level cirrus clouds are purple. Above note the middle thundercloud scene the cellular structure and edges of this cloud is apparent and the color is reddish-purple.

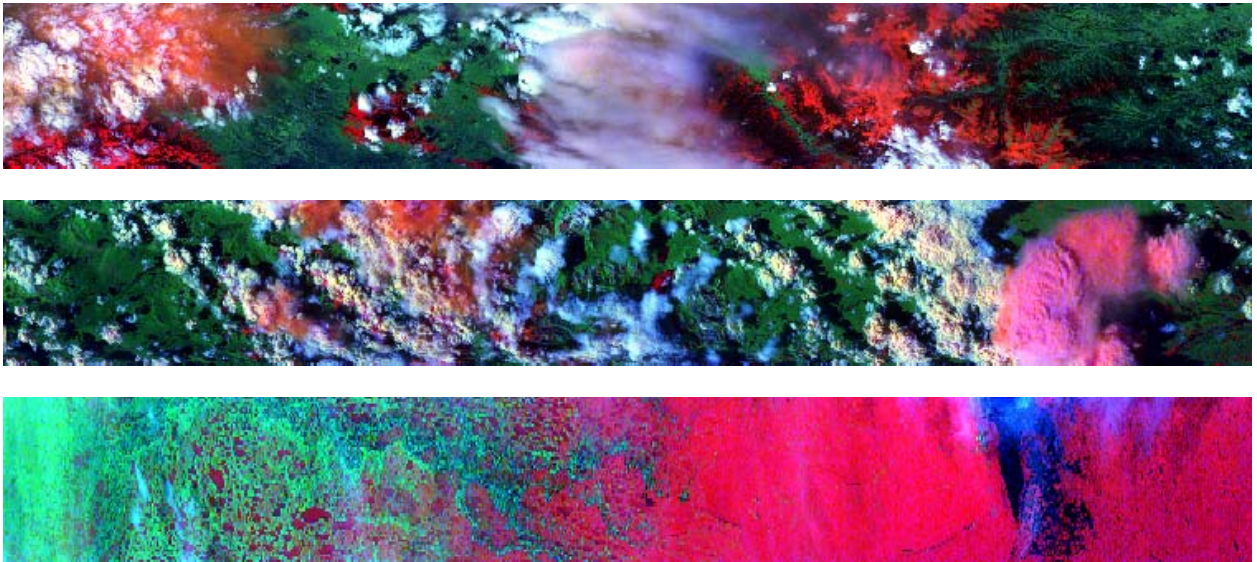


Figure 71. RGB (.640, 1.61, BT3.75-BT4.0)

Using this RGB composite snow/ice surfaces are red, low level water clouds are white, vegetated land is green, thin cirrus are red to gray, however over some regions they tend to be the same color as the underlying surface but blur the surface features. Thin cirrus over water is blue-purple while over snow/ice it is pinkish colored. Thunderclouds tend to be pink in color.

Chapter 7

REFERENCES

- Allen, R. C., Durkee, P. A., and C. H. Wash, 1990: Snow/cloud discrimination with multispectral satellite measurements, *J. Appl. Met.*, 29, 994-1004.
- Anderson, G. P., Clough, S. A., Kneizys, F. X., Chetwynd, J. H., and E. P. Shettle, 1986: AFGL Atmospheric Constituent profiles (0-120 km), A. F. Geophysics Laboratory Technical Report, GL-TR-86-0110, pp. 43.
- Anding, D. and R. Kauth, 1970: Estimation of sea surface temperature from space, *Rem. Sens. Environ.*, 1, 217-220.
- Anding D. and R. Kauth, 1972: Reply to the comment by G. A. Maul and M. Sidran, *Rem. Sens. Environ.*, 2, 171-173.
- Berk, A., Bernstein, L. S., and D. C. Robertson, 1989: MODTRAN: A Moderate Resolution Model for LOWTRAN 7, A. F. Geophysics Laboratory Technical Report, GL-TR-89-0122, pp 38.
- Gao, B. C. and Goetz, A. F. H., and W. J. Wiscombe, 1993: Cirrus cloud detection from Airborne Imaging Spectrometer Data using the 1.38 micron water vapor band, *Journal of Geophysical Letters*, 20, 301-304.
- Goetz, A. F. H., Van, G., Solomon, J., and B. Rock, 1985: Imaging spectrometry for Earth remote sensing, *Science*, 228, 1147-1153.
- Hutchison, K. D. and J. K. Locke, 1997: Snow Identification through Cirrus Cloudy Atmospheres using AVHRR Daytime Imagery, *Geophysical Research Letters*, 24, 1791-1794.
- Hutchison, K. D., B. J. Etherton, and P. C. Topping, 1997: Validation of Automated Cloud Top Phase Algorithms: Distinguishing Between Cirrus Clouds and Snow in A-priori Analyses of AVHRR Imagery, *Optical Engineering*, 36, 1727-1737.
- Hutchison, K. D., Etherton, B. J., Topping, P. C., and A. H. L. Huang, 1997: Cloud Top Phase Determination from the Fusion of Signatures in Daytime AVHRR Imagery and HIRS Data, *International Journal of Remote Sensing*, 18, 3245-3262.
- Hutchison, K. D., Hardy, K., and Gao, B. C., 1995: Improved Detection of Optically-Thin Cirrus Clouds in Nighttime Multispectral Meteorological Satellite Imagery using Total Integrated Water Vapor Information, *Journal of Applied Meteorology*, 34, 1161-1168.
- Hutchison, K. D., Marusa, S., Henderson, J. R., Kenley, R. C., Topping, P. C., Uplinger, W., and J. Twomey, 1999: System Design Considerations for the Retrieval of Sea

Surface Temperatures during the NPOESS Era, *Journal of Atmospheric and Oceanic Technology*, 1, 107-116.

Hutchison, K., and P. Janota, 1989: Cloud Models Enhancement Project Phase 1 Report, The Analytic Sciences Corporation (TASC) Technical Report, TR-5773-1, August 1989.

Inoue, T., 1985: On the temperature and effective emissivity determination of semitransparent cirrus clouds by bi-spectral measurements in the 10 micron window region, *Journal of Meteorological Society of Japan*, 63, 88-99.

Keiss, R. B., and W. M. Cox, 1985, The AFGWC Automated Real-time Cloud Analysis Model, US Air Force Technical Note, *AFGWC-TN-88/001*, pp. 80.

Liou, K-N., 1980: Introduction to Atmospheric Radiation, International Geophysics Series, 26, London, New York: Academic Press.

Liou, K-N., 1992: Radiation and Cloud Processes in the Atmosphere, Oxford press,

McMillin, L. M. and D. S. Crosby, 1984: Theory and validation of the multiple window sea surface temperature technique, *J. Geophys. Res.*, 89(C3), 3655-3661.

National Polar-Orbiting Operational Environmental Satellite System (NPOESS) Technical Requirements Document (TRD), Appendix D, NPOESS System EDR Requirements, Version 6a, June, 2001, pp 86.

National Polar-Orbiting Operational Environmental Satellite System (NPOESS) Visible/Infrared Imager/Radiometer Suite (VIIRS) Sensor Requirements Document (SRD), Version 3, June, 2000, pp 91.

Planet, W.G. (ed.), (1988). Data extraction and calibration of TIROS-N/NOAA radiometers. NOAA Technical Memorandum NESS 107 – Rev. 1, Oct. 1988. 130 pp.

Saunders, R. W. and K. T. Kriebel, 1988: An improved method for detecting clear sky and cloudy radiances from AVHRR data, *International Journal of Remote Sensing*, 9, 123-150.

Scorer, R. S., 1990: *Satellite as Microscope*, Ellis Horwood Limited, pp 267.

Stewart, R. H., 1985: Methods of Satellite Oceanography, University of California Press, Berkeley, CA., pp 360.

Stowe, L. L., McClain, E.P., Casey, R., Pellegrino, P., Gutman, G. G., Davis, P., Long, C., and S. Hart, 1991, Global distribution of cloud cover derived from NOAA/AVHRR operational satellite data, Colloquium on Advances in Space Research, 28th Scientific Assembly of the COPSAR, The Hague, Netherlands, 11, (3)51-(3)54.

Valovcin, F. R., 1978: Spectral radiance of snow and clouds in the near infrared spectral region, Tech. Rep. *AFGL-TR-78-0289*, 46 pp., USAF Geophysics Lab., Bedford, MA..

Vane, G., 1987: Airborne visible/infrared imaging spectrometer (AVIRIS), *Jet Propulsion Laboratory Publication 87-38*, Jet Propulsion Laboratory, Pasadena, CA.

Za'vody, A.M., Mutlow, C.T., and D.T. Llewellyn-Jones, 1995: A radiative transfer model for sea surface temperature retrieval for the along-track scanning radiometer, *J. Geophy Res.*, 100(C1), 937-952.